



HAL
open science

Efficient computation of modal Green's kernels for vectorial equations in helioseismology under spherical symmetry

Hélène Barucq, Florian Faucher, Damien Fournier, Laurent Gizon, Ha Pham

► **To cite this version:**

Hélène Barucq, Florian Faucher, Damien Fournier, Laurent Gizon, Ha Pham. Efficient computation of modal Green's kernels for vectorial equations in helioseismology under spherical symmetry. [Research Report] RR-9433, Inria Bordeaux - Sud Ouest. 2021, pp.86. hal-03406855

HAL Id: hal-03406855

<https://hal.science/hal-03406855>

Submitted on 28 Oct 2021

HAL is a multi-disciplinary open access archive for the deposit and dissemination of scientific research documents, whether they are published or not. The documents may come from teaching and research institutions in France or abroad, or from public or private research centers.

L'archive ouverte pluridisciplinaire **HAL**, est destinée au dépôt et à la diffusion de documents scientifiques de niveau recherche, publiés ou non, émanant des établissements d'enseignement et de recherche français ou étrangers, des laboratoires publics ou privés.



Efficient computation of modal Green's kernels for vectorial equations in helioseismology under spherical symmetry

Hélène Barucq, Florian Faucher, Damien Fournier,
Laurent Gizon, Ha Pham

**RESEARCH
REPORT**

N° 9433

October 2021

Project-Team Makutu



Efficient computation of modal Green's kernels for vectorial equations in helioseismology under spherical symmetry

Hélène Barucq^{*}, Florian Faucher^{†*}, Damien Fournier[‡],

Laurent Gizon^{‡§ ¶}, Ha Pham^{*}

Project-Team Makutu

Research Report n° 9433 — October 2021 — 83 pages

^{*} Inria Project-Team Magique 3D, E2S-UPPA, CNRS, Pau, France.

[†] Faculty of Mathematics, University of Vienna, Oskar-Morgenstern-Platz 1, A-1090 Vienna, Austria.

[‡] Max-Planck-Institut für Sonnensystemforschung, Justus-von-Liebig-Weg 3, 37077 Göttingen, Germany.

[§] Institut für Astrophysik, Georg-August-Universität Göttingen, Friedrich-Hund-Platz 1, 37077 Göttingen, Germany.

[¶] Center for Space Science, NYUAD Institute, New York University Abu Dhabi, PO Box 129188, Abu Dhabi, UAE.

**RESEARCH CENTRE
BORDEAUX – SUD-OUEST**

200 avenue de la Vieille Tour
33405 Talence Cedex

Abstract: We investigate the numerical computation of physical modal Green's kernels for the time-harmonic Galbrun's equation in helioseismology under spherical symmetry. These kernels are the coefficients of the 3D Green's kernels in the vector spherical harmonic expansion. In a previous work, we have characterized the physical kernels for the isothermal radial solar background model S-AtmoI and provide their well-posedness results. Here, we provide an algorithm to compute efficiently these kernels for all receiver and source positions in a region of interest and develop the technical ingredients for its implementation.

The kernels are built from the solution of a scalar wave equation for the radial displacement. The solution and its derivative which are both necessary to assemble the Green's kernel are obtained by solving a first-order system using the HDG method. This approach extends previous works considering a scalar wave equation and allows to model not only the pressure modes but also the surface and internal gravity waves. While being physically more interesting, this problem raises additional numerical difficulties. In particular, the solution of the Schrödinger equation for the radial displacement is singular without attenuation and it is thus preferable to solve the original equation. Moreover, for low frequencies and high-modes, the potential switches sign in the atmosphere which requires the position of the artificial boundary to be further away from the solar surface in order to capture the correct physical solution.

Key-words: Helioseismology, modal Green's kernels, Galbrun's equation, Radiation boundary conditions, Hybridizable discontinuous Galerkin method, wave equation, vector spherical harmonics.

Calcul des noyaux de Green modaux pour l'équation vectorielle en héliosismologie avec symétrie sphérique

Résumé : Dans ce travail, nous étudions et calculons les noyaux de Green modaux pour l'équation de Galbrun pour les ondes harmoniques dans un problème d'héliosismologie avec symétrie sphérique. Ces noyaux sont les coefficients des noyaux de Green 3D décomposés en harmoniques sphériques vectorielles. Dans nos travaux précédents, nous avons caractérisé les noyaux physiques pour le milieu solaire isothermal S-AtmoI, en donnant les résultats sur le caractère bien-posé du problème. Dans ce travail, nous définissons un algorithme pour calculer de manière efficace et précise ces noyaux, pour tous les récepteurs et les sources, et développons tous les ingrédients techniques à sa mise en place. Les noyaux sont construits à partir de la solution de l'équation d'onde pour le déplacement radial. Plus précisément, la solution et sa dérivée sont toutes les deux nécessaires pour assembler les noyaux de Green et sont obtenues à partir du système du premier-ordre en utilisant la méthode de discrétisation de Galerkin discontinue hybride. Cette approche étend nos travaux précédents sur l'équation d'onde scalaire, et nous permet de modéliser non seulement les modes acoustiques du soleil, mais également les ondes de gravité de surface et internes. Ce problème vectoriel révèle aussi des difficultés numériques additionnelles. En particulier, la solution de l'équation de Schrödinger pour le déplacement radial est singulière dans le cas sans atténuation, et il est ainsi préférable de résoudre l'équation originale à la place. De plus, à fréquences basses et modes de hauts degrés, le potentiel change de signe dans l'atmosphère, ce qui implique que la condition de radiation pour la troncature du domaine numérique doit être placée bien plus loin que la surface solaire afin d'obtenir la solution correcte.

Mots-clés : Héliosismologie, Noyaux de Green modaux, Équation de Galbrun, Conditions aux limites de radiation, méthode de Galerkin discontinue hybride, équation des ondes, harmoniques sphériques vectorielles.

Contents

1	Introduction	5
2	Notations	7
3	Theoretical results - Part 1	10
3.1	Coefficients of the modal ODEs	15
3.2	Properties of the modal ODEs	18
3.2.1	Singularities	18
3.2.2	Growth and decay when r tends to infinity	20
3.3	Existence and uniqueness of the outgoing modal Green's kernel	22
4	Theoretical results - Part 2: Coefficients of the formal expansion of the 3D Green's kernel in VSH basis	25
5	Numerical computation working with original equation \mathfrak{L}_ℓ	32
5.1	Boundary conditions	33
5.2	Approaches to compute G_ℓ^+	34
5.3	First-order formulation	36
5.4	Discretization with HDG method	38
6	Radiation boundary condition coefficients	43
6.1	Approximation of V_ℓ in the atmosphere	43
6.2	List of Radiation boundary conditions	46
7	Numerical experiments using solar background models	48
7.1	Maps of the solar potentials	49
7.2	Original and conjugated regular solutions, effect of attenuation	53
7.2.1	Original and conjugated problems	53
7.2.2	Numerical comparisons	54
7.3	Efficiency of the radiation boundary conditions	57
7.3.1	Construction of a reference solution	57
7.3.2	Oscillatory pattern of solutions and Whittaker's function	57
7.3.3	Position of the radiation boundary conditions	60
7.3.4	Analysis of performance	63
7.4	Modal Green's kernels	65
7.4.1	Comparison of the approaches	65
7.4.2	Comparison of the vector modal Green's kernels	67
7.5	Multi-frequency, multi-modal representations	70
7.5.1	Experiments at fixed mode and different levels of attenuation	70
7.5.2	Experiments with all modes	73
7.6	Concluding remarks	74
8	Conclusion	75
A	Numerical computation working with conjugated equation \mathcal{L}_ℓ	76
A.1	Coefficients of the Green's kernels using the conjugated equation	76
A.2	Implementation of the HDG method for \mathcal{L}_ℓ	77
A.2.1	Boundary conditions	77
A.2.2	Direct and assembling methods	77
A.2.3	First-order formulation	78
A.2.4	Discretization with HDG	79

1 Introduction

In this work, with applications geared towards local helioseismology, we investigate the numerical computation of the modal Green's kernels for the time-harmonic simplified Galbrun's equation under spherical symmetry,

$$\begin{aligned} \mathfrak{L}_{\text{SG}} \boldsymbol{\xi} &= F \quad \text{in } \mathbb{R}^3, \\ \text{with } \mathfrak{L}_{\text{SG}} \boldsymbol{\xi} &= -\rho_0(\omega^2 + 2i\omega\Gamma) \boldsymbol{\xi} - \nabla[\gamma p_0 \nabla \cdot \boldsymbol{\xi}] + (\nabla p_0)(\nabla \cdot \boldsymbol{\xi}) \\ &\quad - \nabla(\boldsymbol{\xi} \cdot \nabla p_0) + (\boldsymbol{\xi} \cdot \nabla) \nabla p_0 + \rho_0(\boldsymbol{\xi} \cdot \nabla) \nabla \phi_0. \end{aligned} \quad (1.1)$$

The above equation models small adiabatic displacement, represented by $\boldsymbol{\xi}$, on top of a stationary self-gravitating background without flow with the latter characterized by pressure p_0 , density ρ_0 , and adiabatic index γ ; additionally, attenuation is prescribed by the parameter Γ . Equation (1.1) is obtained from the full equation given by Lynden-Bell and Ostriker in [30], by ignoring background flow, rotation, and perturbation to the gravitational potential. The original equation lends its name from the work of Galbrun [25] in aeroacoustics and we refer to [31] for a discussion of the history of the Galbrun's equation in this context. Galbrun's equation also plays an important role in helioseismology, cf., e.g., the lecture notes of Christensen-Dalsgaard [18] and Gough [27]. In particular, its eigenvalues represent data for inversion in global helioseismology, cf. [18], while its Green's kernels are used to compute helioseismic sensitivity kernels in local helioseismology, cf. [26, 12, 9].

The Green's kernel \mathbb{G} is a distributional solution to (1.1) with right-hand side $F = \delta(\mathbf{x} - \mathbf{s})$. As a standard approach to solve vector equations in spherical symmetry, one works with modal Green's kernels which are the coefficients of \mathbb{G} in (formal) vector spherical harmonics (VSH) expansion. This is also applied for computing eigenfunctions; specifically, eigenpairs of (1.1) come from those of its modal operators and the eigenfunctions are computed in terms of their coefficients in VSH basis, cf. [17, 18, 27, 11]. Other perspectives to study the Galbrun's equation without spherical symmetry is the theoretical investigation for bounded domains in [29], and for unbounded settings in [28]. For numerical treatments of the Galbrun's equation in \mathbb{R}^2 , see, e.g., [13, 31]. We also refer to the introduction of [29, 28] for references on mathematical analysis of Galbrun's equation or simplified versions in the context of aeroacoustics.

There are two main approaches in computing the Green's kernel of \mathfrak{L}_{SG} exploiting the assumption of spherical symmetry. Most works in helioseismology consider \mathfrak{L}_{SG} in the form of a boundary-value problem (BVP) defined on the bounded domain Ω_{\odot} (occupied by the Sun) with vanishing Lagrangian pressure perturbation $\delta_p^L := -\rho_0 c_0^2 \nabla \cdot \boldsymbol{\xi}$ condition placed at the boundary (i.e. at the height of the photosphere),

$$\mathfrak{L}_{\text{SG}} \boldsymbol{\xi} = F \text{ on } \Omega_{\odot}, \quad \text{with } \delta_p^L = 0 \text{ on } \partial\Omega_{\odot}. \quad (1.2)$$

This formulation does not allow for the presence of an atmosphere and fails to model waves that can propagate beyond the photosphere. In [12], Böning et al. considered the BVP (1.2) and wrote its associated Green's kernel \mathbb{G} as a sum of eigenfunctions summed over the discrete spectrum, cf. [12, Appendix B]. The eigenvalues and the coefficients of the eigenfunctions in VSH basis are then computed using¹ ADIPLS [17]. In a second approach, one computes the coefficients of \mathbb{G} in VSH basis, i.e. the modal Green's kernels, directly as solutions to modal equations with Dirac right-hand side (rhs). This is the approach taken by [10, 32, 9] to compute the modal Green's kernels also associated to the BVP (1.2).

The main objective of this work is to put into practice the theoretical results of [6] in order to extend the work in [3] to equation (1.1) and obtain an efficient algorithm for computing modal Green's kernels which are mathematically defined on \mathbb{R}^3 . This report documents the development of the necessary ingredients needed for the final results. We list below the main groups of results/novelities realized in this work.

- In comparison with the aforementioned references [18, 10, 12], we study (1.1) defined on the whole \mathbb{R}^3 . To include an atmospheric model, as was done in [6, 5], we extend the physical parameters $(\rho_0, \gamma, p_0, \phi_0)$, which are given by the model \mathcal{S} in the interior of the Sun, to \mathbb{R}^3 according to the isothermal atmospheric model *Atmo-I* constructed in [22]. This approach to model the atmosphere

¹We note that the eigenvalues in [27, 18] are used for inversion in global helioseismology, while the eigenpairs computed by the same software in [12] serve to carry out local helioseismology inversion, in particular to compute sensitivity kernel.

was also employed in [24, 2] for the helioseismic scalar wave operator L_{scalar} (recalled in Remark 6), see also [8, 3]. The unboundedness of the domain also necessitates constructing criteria to choose the correct family of solutions; these are called the *physical* or *outgoing* solutions and are intuitively those that tend to zero at infinity in the presence of attenuation. This task, realized in [6, 5], characterized explicitly the physical modal Green's kernels for (1.1) and established the existence and uniqueness of such solutions. The current work is the numerical analog to the theoretical results obtained in [6, 5].

- Our approach to compute the modal Green's kernel is comparable to [10, 32], in the sense that it is computed directly and not via a spectral expansion. However, we carry out our theoretical (in [6, 5]) and numerical investigation using a second-order ODE (derived from (1.1) which only involves the displacement ξ , instead of a first-order ODE system (cf. (3.26)) in terms of the radial component of displacement and the Eulerian perturbation in pressure; we refer to Remark 5 for further discussion. In this direction, while we also show results obtained by computing the modal kernel directly (i.e. as a solution with Dirac rhs), which is referred to as the *Direct approach* in this work (Subsection 5.2), we also extend the approach employed in [3] for the scalar wave equation, which is based on the fact that Green's kernels of scalar second-order ODEs are given by an analytic 'gluing' formula involving the Heaviside function and regular modal solutions (solutions to modal equation with zero rhs). This idea was exploited in [3] for the scalar equation, and sees its full utility for the vector equations. In particular, the advantage of using first-order formulation to solve the ODE in the patching algorithm allows to compute analytically the nonradial components of \mathbb{G} . This is in addition to providing the value of the full kernel already exploited in [3]. Recall from [3], by the complete kernel, we mean having its value for all positions of source and receiver in $[\epsilon, r_{\text{max}}] \times [\epsilon, r_{\text{max}}]$, with $0 < \epsilon < r_{\text{max}}$. The theoretical discussion of this result is given in Section 4, in particular Proposition 2, and the numerical implementation is in Section 5, in particular Algorithm 1.
- We also discuss the robustness (or the lack thereof) of two versions of the modal operators: the original one denoted by \mathcal{L}_ℓ and the conjugate operator \mathcal{L}_ℓ . Their explicit expression and meaning are recalled in Section 3. The theoretical results in [6, 5] was obtained with \mathcal{L}_ℓ using long-range scattering theory for Schrödinger equation. However due to the singularity of the solution and the coefficients of \mathcal{L}_ℓ at zero attenuation, it becomes numerically unstable to work with. This is a new feature of the vector equation (1.1) compared to the scalar wave operator for which both the numerical implementation and theoretical work are carried for the conjugated operator L_{scalar} and its modal operator L_ℓ (see definition in Remark 6). In the same process, we also illustrate the regularity and oscillatory behavior of the modal solutions predicted from [6]. Proposition 2 also clarifies the singularity of the Green's kernel \mathbb{G} , which contains a Dirac distribution in its nonradial components.
- Radiation boundary conditions (RBC) are needed to compute outgoing solutions numerically. This work gives an organized exposition on the coefficients initially developed in [5], and carry out a numerical comparison on their robustness. We have seen from [3, 8] the importance of using the correct wavenumber in the RBC. The analysis in [6, 5] has provided us with the correct wavenumber k_a for the vector equation (1.1), cf. (3.63) and (3.68). A novelty in comparison with the scalar equation is the presence of the gravity term. The numerical study in this work also serves to analyze the importance of this term despite its low order in r (order $O(r^{-3})$ compared to the highest order being $O(1)$).
- Using the solar background models, we observe that the potential associated with the vector-wave problem has the profile of a well in the atmosphere for frequencies that are below both the cut-off and atmospheric Lamb frequencies. These wells appear at relatively low frequencies and high modes, and they do not exist with the scalar-wave approximations. These low frequencies and high modes configurations are particularly challenging as the potential changes sign in the atmosphere and we observe a drop of accuracy regarding the radiation boundary conditions, which have to be put further away in the atmosphere to ensure the accuracy.

The organization of the report is as follows. After introducing the necessary notations in Section 2, we recall the main results of [6] in Section 3 and organize them in a way that is more geared towards numerical implementation. New remarks and figures are also added here. In Section 4, the patching formula is obtained for nonradial components of Green's kernels with the main results summarized in Proposition 2. This proposition also shows the reciprocity of the coefficients. In Section 5, we develop the algorithm which implements Proposition 2, where we use the Hybridizable Discontinuous Galerkin

discretization (HDG) which leads to a first-order formulation. In Section 6, we list the choice of RBC coefficients, initially developed in [5]. After developing the necessary tools, we provide numerical results in Section 7, using the background solar models *S-AtmoI* of [22]. We first show that, contrary to the scalar-wave problem, the potential of the vector-wave problem has the profile of a well in the atmosphere region, in the case of low frequency and high modes. We then compare the numerical accuracy when solving the original or conjugated problems, highlighting that the latter leads to inaccuracy in the case of no (or low) attenuation. The efficiency of the RBC is investigated before we compute the solar Green's kernels.

2 Notations

Scaled system We denote by R_\odot the Sun's radius with $R_\odot = 6.96 \times 10^8$ m. We have denoted by $X \in \mathbb{R}^3$ the coordinate system in \mathbb{R}^3 with the origin placed at the center of the Sun and the set $\{\|X\| = R_\odot\}$ representing its surface. The scaled coordinates \mathbf{x} and radius $r = \|\mathbf{x}\|$, are defined by

$$\mathbf{x} = \frac{X}{R_\odot}, \quad r = \frac{R}{R_\odot}, \quad R = \|X\|. \quad (2.1)$$

We note three special values of the scaled radius. The surface of the Sun in scaled coordinates is given by $\{r = 1\}$, while the value $r = r_s$ corresponds to the height at which the reference solar model *S* ends ([15]), and $r = r_a$ the beginning of the model *AtmoI*. The specific values of these heights employed in our experiments are,

$$r_s = 1.0007126, \quad r_a = 1.00073. \quad (2.2)$$

Given a function in terms of R , $R \mapsto \check{f}(R)$, we can define one in terms of r that taking the same value, $r \mapsto f(r)$, such that,

$$f(r) = \check{f}(R_\odot r). \quad (2.3)$$

Physical background parameters In Table 1, we introduce the notations for the physical background parameters in scaled coordinates, defined from the original ones using relation (2.3). We also assume adiabaticity for the whole region

$$c_0^2 \rho_0 = \gamma p_0 \quad (\text{equivalently} \quad c_0^2 \rho_0 = \gamma p_0). \quad (2.4)$$

Table 1: Background parameters notations. Function in R and r are related by relation (2.3).

	As a function of R	As a function of r	Unit (SI)
Density	ρ_0	ρ_0	kg m^{-3}
Pressure	p_0	p_0	Pa
Adiabatic exponent	γ	γ	-
Attenuation	Γ	Γ	s^{-1}
Sound speed	c_0	c_0	m s^{-1}
Gravity potential	ϕ_0	ϕ_0	$\text{m}^2 \text{s}^{-2}$

Auxilliary background quantities Background quantities defined from ρ_0 , γ , and p_0

1. When ρ_0 is radial, with $'$ denoting the derivative with respect to the radial coordinate r , the *gravitational potential* ϕ_0 is the solution to, cf. [5, Appendix G.3],

$$\frac{1}{r^2} (r^2 \phi_0')' = 4\pi G R_\odot^2 \rho_0, \quad \text{with} \quad \phi_0'(r) = \frac{4\pi G R_\odot^2}{r^2} \int_0^r \rho_0(s) s^2 ds, \quad (2.5)$$

with G the gravitational constant

$$G = 6.67430 \times 10^{-8} \text{cm}^3 \text{g}^{-1} \text{s}^{-2}. \quad (2.6)$$

2. We introduce the *inverse scale height* function α_\bullet associated with a \mathcal{C}^1 function $\mathfrak{g}(r)$:

$$\alpha_{\mathfrak{g}}(r) := -\frac{\mathfrak{g}'(r)}{\mathfrak{g}(r)}. \quad (2.7)$$

3. We introduce the quantity E_{he} (unitless) which measures the deviation from hydrostatic equilibrium,

$$E_{\text{he}}(r) := \frac{\phi_0'(r)}{c_0^2(r)} - \frac{\alpha_{p_0}(r)}{\gamma(r)}. \quad (2.8)$$

This also means that hydrostatic equilibrium assumption is equivalent to $E_{\text{he}} = 0$, see [6, footnote 1] for the origin of this condition.

Remark 1 (Other notations of gravitational potentials). *We can further give additional notations.*

1. In [6], we worked with the scaled background gravitational potential $r \mapsto \Phi_0(r)$ (in s^{-2}) defined by

$$\frac{1}{r^2} (r^2 \Phi_0')' = 4\pi G \rho_0, \quad \text{with} \quad \Phi_0'(r) = \frac{4\pi G}{r^2} \int_0^r \rho_0(s) s^2 ds. \quad (2.9)$$

This is related to $\phi_0(r)$ defined in (2.5) by

$$\Phi_0(r) = \frac{\phi_0(r)}{R_\odot^2}. \quad (2.10)$$

In terms of Φ_0 , the hydrostatic equilibrium quantity (2.8) is

$$E_{\text{he}}(r) = R_\odot^2 \frac{\Phi_0'(r)}{c_0^2(r)} - \frac{\alpha_{p_0}(r)}{\gamma(r)}. \quad (2.11)$$

2. A more standard version is the gravitational potential in unscaled coordinates, $R \mapsto \phi_0(R)$, which solves the PDE,

$$\frac{1}{R^2} \frac{d}{dR} \left(R^2 \frac{d}{dR} \phi_0 \right) = 4\pi G \rho_0(R), \quad (2.12)$$

and is related to $\phi_0(r)$ by the relation (2.3). From the identity $\frac{d\phi_0}{dr}(r) = R_\odot \frac{d\phi_0}{dR}(R_\odot r)$

$$\frac{d\phi_0}{dR}(R) = \frac{4\pi G}{R^2} \int_0^R \rho_0(S) S^2 dS = R_\odot \frac{4\pi G}{r^2} \int_0^r \rho_0(s) s^2 ds, \quad (2.13)$$

we also obtain the expression (2.5) for ϕ_0' . \diamond

Square root branches We work with two branches of square root, for $z \in \mathbb{C} \setminus \{0\}$,

$$\sqrt{z} := |z| e^{i\tilde{\text{Arg}}(z)/2}, \quad \text{with argument } \tilde{\text{Arg}} : \mathbb{C} \setminus \{0\} \rightarrow [0, 2\pi); \quad (2.14a)$$

$$(z)^{1/2} := |z| e^{i\text{Arg}(z)/2}, \quad \text{with argument } \text{Arg} : \mathbb{C} \setminus \{0\} \rightarrow (-\pi, \pi]. \quad (2.14b)$$

The branch $(\cdot)^{1/2}$ is also called the principal branch. The first choice is common in scattering theory with $\text{Im}\sqrt{z} > 0$. We have

$$\text{Im } z > 0 \implies (z)^{1/2} = \sqrt{z}. \quad (2.15)$$

The wavenumbers The *complex-frequency* σ (in s^{-1}) and wavenumber k_0 (unitless) are defined in terms of the angular frequency ω and attenuation $\Gamma(\omega, r)$,

$$\sigma(r, \omega) = \sqrt{\omega^2 + 2i\omega\Gamma(\omega, r)}, \quad k_0(r) = R_\odot \frac{\sigma(r)}{c_0(r)}. \quad (2.16)$$

We introduce the wavenumber function $k(r)$ and the parameter $\eta(r)$ such that

$$-k^2 := \frac{\alpha_{\gamma p_0}^2}{4} - \frac{\alpha'_{\gamma p_0}}{2} - k_0^2, \quad (2.17a)$$

$$\eta := 2\frac{\alpha_{p_0}}{\gamma} - \alpha_{\gamma p_0}. \quad (2.17b)$$

Important auxiliary functions The following function appears in the change of variable between the original modal ODE and its Schrödinger form,

$$\mathfrak{J}_\ell(r) = \frac{1}{r c_0 \sqrt{\rho_0}} \frac{\sqrt{F_\ell}}{\sqrt{F_0}} = \frac{1}{r c_0 \sqrt{\rho_0}} \frac{\sqrt{\sigma^2 - S_\ell^2 - \frac{E_{\text{he}}}{r} \frac{c_0^2}{R_\odot^2}}}{\sqrt{\sigma^2 - \frac{E_{\text{he}}}{r} \frac{c_0^2}{R_\odot^2}}}, \quad (2.18)$$

with functions

$$F_\ell := k_0^2 r^2 - r E_{\text{he}} - \ell(\ell + 1); \quad F_0 := k_0^2 r^2 - r E_{\text{he}}. \quad (2.19)$$

In the second expression of (2.18), S_ℓ is the Lamb frequency, cf. [16, Equation 30]:

$$S_\ell^2 := \ell(\ell + 1) \frac{c_0^2}{r^2 R_\odot^2}. \quad (2.20)$$

The relation between S_ℓ and F_ℓ is given in Remark 7. We also recall the definition of the Brunt-Väisälä or buoyancy frequency N ,

$$N^2 := \frac{\phi'_0}{R_\odot^2} \left(\alpha_{\rho_0} - \frac{\alpha_{p_0}}{\gamma} \right). \quad (2.21)$$

Vector spherical harmonics The tangential gradient acting on a scalar function f and tangential divergence acting on the vector $\mathbf{v} = v_r \mathbf{e}_r + v_\theta \mathbf{e}_\theta + v_\phi \mathbf{e}_\phi$ are given by

$$\nabla_{\mathbb{S}^2} f := \partial_\theta f \mathbf{e}_\theta + \frac{\partial_\phi f}{\sin \theta} \mathbf{e}_\phi, \quad \nabla_{\mathbb{S}^2} \cdot \mathbf{v} := \frac{\partial_\theta(\sin \theta v_\theta)}{\sin \theta} + \frac{\partial_\phi v_\phi}{\sin \theta}. \quad (2.22)$$

Constructed from the scalar spherical harmonics Y_ℓ^m together with $\nabla_{\mathbb{S}^2}$, an orthonormal basis for $L^2(\mathbb{R}^3)^3$ vector is given by, cf. [34, Eq. (9.56), Section 9.3.3] or [33, Definition 3.336, p. 107],

$$\begin{aligned} \mathbf{P}_\ell^m(\hat{\mathbf{x}}) &= Y_\ell^m(\hat{\mathbf{x}}) \mathbf{e}_r, \quad \ell = 0, 1, \dots; \\ \mathbf{B}_\ell^m(\hat{\mathbf{x}}) &= \frac{\nabla_{\mathbb{S}^2} Y_\ell^m}{\sqrt{\ell(\ell + 1)}}, \quad \mathbf{C}_\ell^m(\hat{\mathbf{x}}) = -\frac{\mathbf{e}_r \times \nabla_{\mathbb{S}^2} Y_\ell^m}{\sqrt{\ell(\ell + 1)}}, \quad \ell = 1, 2, \dots, \end{aligned} \quad (2.23)$$

The above choices in basis function and notation agree with [20, Equation B.158-B.160], see further discussion in Remark 2.

Remark 2. In this work as in previous ones [6, 5], we follow the convention of the scalar and vector spherical harmonics of [34, 19], which was employed to solve the Maxwell equation in spherical symmetry. We recall the important expressions here. The scalar spherical harmonics Y_ℓ^m are defined, for $m = -\ell, \dots, \ell$, $\ell = 0, 1, 2, \dots$, as

$$Y_\ell^m(\theta, \phi) = \sqrt{\frac{(2\ell + 1)}{4\pi} \frac{(\ell - |m|)!}{(\ell + |m|)!}} P_\ell^{|m|}(\cos \theta) e^{i m \phi}, \quad (2.24)$$

where the Legendre polynomial P_ℓ is given by the Rodrigues' formula, cf. [34, Equation 9.35],

$$P_\ell(t) = \frac{(-1)^\ell}{2^\ell \ell!} \frac{d^\ell}{dt^\ell} (1 - t^2)^\ell = \frac{1}{2^\ell \ell!} \frac{d^\ell}{dt^\ell} (t^2 - 1)^\ell, \quad \ell = 0, 1, 2, \dots, \quad (2.25)$$

and the associated Legendre polynomial P_ℓ^m is defined as

$$P_\ell^m(t) := (1 - t^2)^{m/2} \frac{d^m}{dt^m} P_\ell(t), \quad m = 0, 1, \dots, \ell. \quad (2.26)$$

The above definitions of the Legendre and associated Legendre polynomials are the same as [20, B.67 and B.48]. However the definition of the scalar spherical harmonics (2.24) is slightly different from [20, B.58] by a factor of $(-1)^m$.

In [10, 32, 9], following [14, 38], the VSH basis in (2.23) are also written as (also called the Hansen basis or Chandrasekhar & Kendal basis), cf. [10, Equation 4]

$$\mathbf{Y}_{\ell m}^{(-1)} = \mathbf{P}_{\ell}^m, \quad \mathbf{Y}_{\ell m}^{(1)} = \mathbf{B}_{\ell}^m, \quad \mathbf{Y}_{\ell m}^{(0)} = -\mathbf{C}_{\ell}^m. \quad (2.27)$$

Another choice is the Phinney-Burridge basis, cf. [10, Equation 3]

$$\mathbf{Y}_{\ell m}^{-1} = \frac{\mathbf{B}_{\ell}^m - \mathbf{C}_{\ell}^m}{\sqrt{2}}, \quad \mathbf{Y}_{\ell m}^1 = \frac{\mathbf{B}_{\ell}^m + \mathbf{C}_{\ell}^m}{\sqrt{2}}, \quad \mathbf{Y}_{\ell m}^0 = \mathbf{P}_{\ell}^m. \quad \diamond$$

3 Theoretical results - Part 1

In this section, we recall theoretical results, most of which were obtained in our previous work [6]. The principal goal is to solve (1.1) by expanding the unknowns and the right-hand side in terms of VSH basis. One first obtains a system of equations for the coefficients of the displacement $\boldsymbol{\xi}$, cf. (3.12). Secondly, the system is reduced to an ODE in terms of the coefficients in the radial direction, written in two equivalent forms: one called the original modal equation (3.12a) with operator \mathfrak{L}_{ℓ} and the second in the Schrödinger form (3.14) with operator \mathcal{L}_{ℓ} . The explicit forms of the ODE are given in (3.28) and (3.29) for the original modal operator \mathfrak{L}_{ℓ} , and in (3.34b) and (3.37) for the Schrödinger form \mathcal{L}_{ℓ} . Thirdly, under suitable assumptions on the background parameters (see (3.5)–(3.8)), which are satisfied by the atmospheric solar model Atmo-I, we show how to characterize the physical solution of these ODEs for which one has existence and uniqueness of solution. The theoretical analysis in [6] was carried with \mathcal{L}_{ℓ} , however we show in later sections that \mathfrak{L}_{ℓ} is numerically more stable for small attenuation, and thus is the operator of choice for the computational purposes. For this reason, we also reinterpret the theoretical results (obtained for \mathcal{L}_{ℓ}) in terms of \mathfrak{L}_{ℓ} .

The characterization of the regular physical Green's kernel comprises of choosing the regular solution at the regular singular point $r = 0$ and of determining its oscillatory behavior. The first task is done via indicial analysis which gives the indicial exponents of the solution, cf. (3.55) and (3.56) for \mathcal{L}_{ℓ} , (3.59) and (3.60) for \mathfrak{L}_{ℓ} . The details are given in Subsection 3.2.1. These exponents also include the singular position $r_{\omega, \ell}^*$ (3.48) which only exists at zero attenuation $\Gamma = 0$ and mode $\ell > 0$.

The oscillatory behavior of the solution of \mathcal{L}_{ℓ} is prescribed by a phase function ψ characterized as a solution of eikonal equation (3.76). The analysis also makes appear the wavenumber k_a , cf. (3.63) and (3.68), which controls the oscillation at infinity in r ,

$$w \sim e^{i\psi}(a_+ + \text{l.o.t}) + e^{-i\psi}(a_- + \text{l.o.t}), \quad \text{with} \quad \psi \sim ik_a, \quad r \rightarrow \infty,$$

with l.o.t abbreviation for ‘lower order terms’. Thus wavenumber also plays a key role in the low-order radiation boundary condition in Section 6.

In Subsection 3.3, for each operator, one obtains the explicit ODE and boundary conditions to uniquely characterize the Green's kernel and the basis functions for the homogeneous (without source) solutions,

$$\begin{array}{ll} G_{\ell}^+, \phi_{\ell}^+, \phi_{\ell} & \text{associated with } \mathfrak{L}_{\ell}, & \mathcal{G}_{\ell}^+, \varphi_{\ell}^+, \varphi_{\ell} & \text{associated with } \mathcal{L}_{\ell}. \\ (3.86) & (3.87) & (3.88) & (3.80) & (3.77) & (3.75) \end{array}$$

The relations between the two modal Green's kernels are given in (3.18) and (3.84), while the one between homogeneous solutions are presented in (3.13). The latter relation (3.13) consists of a multiplication by the factor \mathcal{J}_{ℓ} (2.18) which is singular at $r_{\omega, \ell}^*$ (cf. Subsection 3.2.1). The ‘gluing’ formulation which expresses the Green's kernel in terms of the homogeneous solution, (3.79) for \mathcal{G}_{ℓ}^+ , and (3.90) for G_{ℓ}^+ is also the foundation of the computation in Section 4. These so-called ‘gluing’ formulas play a key role in the indirect approach to compute not only the modal Green's kernel but also the coefficients in VSH basis of the 3D kernel. For purpose of comparison, the scalar equation in previous work is recalled in Remark 6.

Equation in scaled coordinate By using $\nabla_X = R_{\odot}^{-1} \nabla_{\mathbf{x}}$, equation (1.1) in variable \mathbf{x} is

$$\mathcal{L}_{\text{SG}} \boldsymbol{\xi} = \mathbf{f}, \quad \text{in } \mathbb{R}^3, \quad (3.1)$$

where the differential operator \mathcal{L}_{SG} is defined in variable \mathbf{x} by

$$\mathcal{L}_{\text{SG}} := -\rho_0 \sigma^2 + \frac{1}{R_\odot^2} \mathcal{P} + \frac{1}{R_\odot^2} \mathcal{G}, \quad (3.2)$$

with

$$\mathcal{G}\xi = \rho_0 (\xi \cdot \nabla_{\mathbf{x}}) \nabla_{\mathbf{x}} \phi_0, \quad (3.3a)$$

$$\mathcal{P}\xi = -\nabla_{\mathbf{x}} [\gamma p_0 \nabla_{\mathbf{x}} \cdot \xi] + (\nabla_{\mathbf{x}} p_0)(\nabla_{\mathbf{x}} \cdot \xi) - \nabla_{\mathbf{x}} [(\xi \cdot \nabla_{\mathbf{x}}) p_0] + (\xi \cdot \nabla_{\mathbf{x}}) \nabla_{\mathbf{x}} p_0. \quad (3.3b)$$

Its unknown $\xi(\mathbf{x})$ and right-hand side $\mathbf{f}(\mathbf{x})$ relates to $\xi(X)$ and $F(X)$ of the original equation (1.1) by

$$\xi(\mathbf{x}) = \xi(R_\odot \mathbf{x}), \quad \mathbf{f}(\mathbf{x}) = F(R_\odot \mathbf{x}). \quad (3.4)$$

Assumption 1. *In addition to the adiabatic condition (2.4), given $r_s < r_a$, we assume that the parameters satisfy the following assumptions.*

1. The functions γ , \mathbf{p}_0 , ρ_0 and $\Gamma(\omega, \cdot)$ are radial and satisfy

$$\Gamma(\omega, r) \geq 0, \quad 1 < \gamma(r) < 2, \quad \rho_0(r) > 0, \quad \mathbf{p}_0(r) > 0; \quad (3.5a)$$

$$\rho_0, \gamma \in \mathcal{C}^2[0, \infty), \quad \mathbf{p}_0 \in \mathcal{C}^3[0, \infty), \quad r \mapsto \Gamma(\omega, r) \in \mathcal{C}^2([0, \infty)); \quad (3.5b)$$

$$r \mathbf{c}_0^{-1} \text{ strictly increasing on } [0, \infty); \quad (3.5c)$$

$$E_{he} \leq 0, \quad E_{he} \text{ decreasing on } [0, \infty). \quad (3.5d)$$

2. The hydrostatic equilibrium is verified for $r \in [0, r_s]$,

$$\mathbf{p}'_0 = -\rho_0 \Phi'_0. \quad (3.6)$$

3. For $r \geq r_a$, the coefficients follow the model *AtmoI*, which assumes the attenuation Γ , the adiabatic coefficient γ , and the sound speed \mathbf{c}_0 to be constant, and the density ρ_0 exponentially decreasing. In other words, we consider positive constants

$$\gamma_a, \alpha_a, \mathbf{c}_a > 0, \quad \text{and } \Gamma_a(\omega) \geq 0, \quad (3.7)$$

such that on $r \geq r_a$,

$$\Gamma(\omega, r) = \Gamma_a(\omega), \quad \gamma(r) = \gamma_a, \quad \mathbf{c}_0(r) = \mathbf{c}_a, \quad \rho_0(r) = \rho_0(r_a) e^{-\alpha_a(r-r_a)}. \quad (3.8)$$

For solar background parameters, we follow the model *S-AtmoI* which is explicitly constructed in [22] and is displayed in Figure 1. They are defined using $r_a = 1.00073$ and we have,

$$\gamma_a = 1.6401, \quad \alpha_a = 6.6325 \times 10^3, \quad \mathbf{c}_a = 9.8608 \times 10^{-6} \text{s}^{-1}. \quad (3.9)$$

In the computational experiment of Section 7, the (scaled) interval for the computation corresponds to $(0, 1.0008)$, that is, we slightly extend after r_a before applying the boundary condition. The efficiency of the boundary condition depending on the size of the computational domain is also studied in this section.

Remark 3. *In order to evaluate how far we are from the hydrostatic equilibrium in the atmosphere, we compare the values of Φ'_0/\mathbf{c}_0^2 and α_{p_0}/γ that enters in the computation of E_{he} (2.8). At the photosphere ($r \approx 1.003$) both quantities are approximately equal to 4000 while $E_{he} \approx -30$ so the deviation from the hydrostatic equilibrium corresponds to a small correction. \diamond*

We next give an overview discussion of the results obtained in [6, Section 7]. Suppose $\xi \in H^1(\mathbb{R}^3)^3$ is a solution with right-hand side $\mathbf{f} \in \mathcal{C}_c^\infty(\mathbb{R}^3)^3$,

$$-R_\odot^2 \rho_0 \sigma^2 \xi + \mathcal{P}\xi + \mathcal{G}\xi = R_\odot^2 \mathbf{f}, \quad \text{in } \mathbb{R}^3.$$

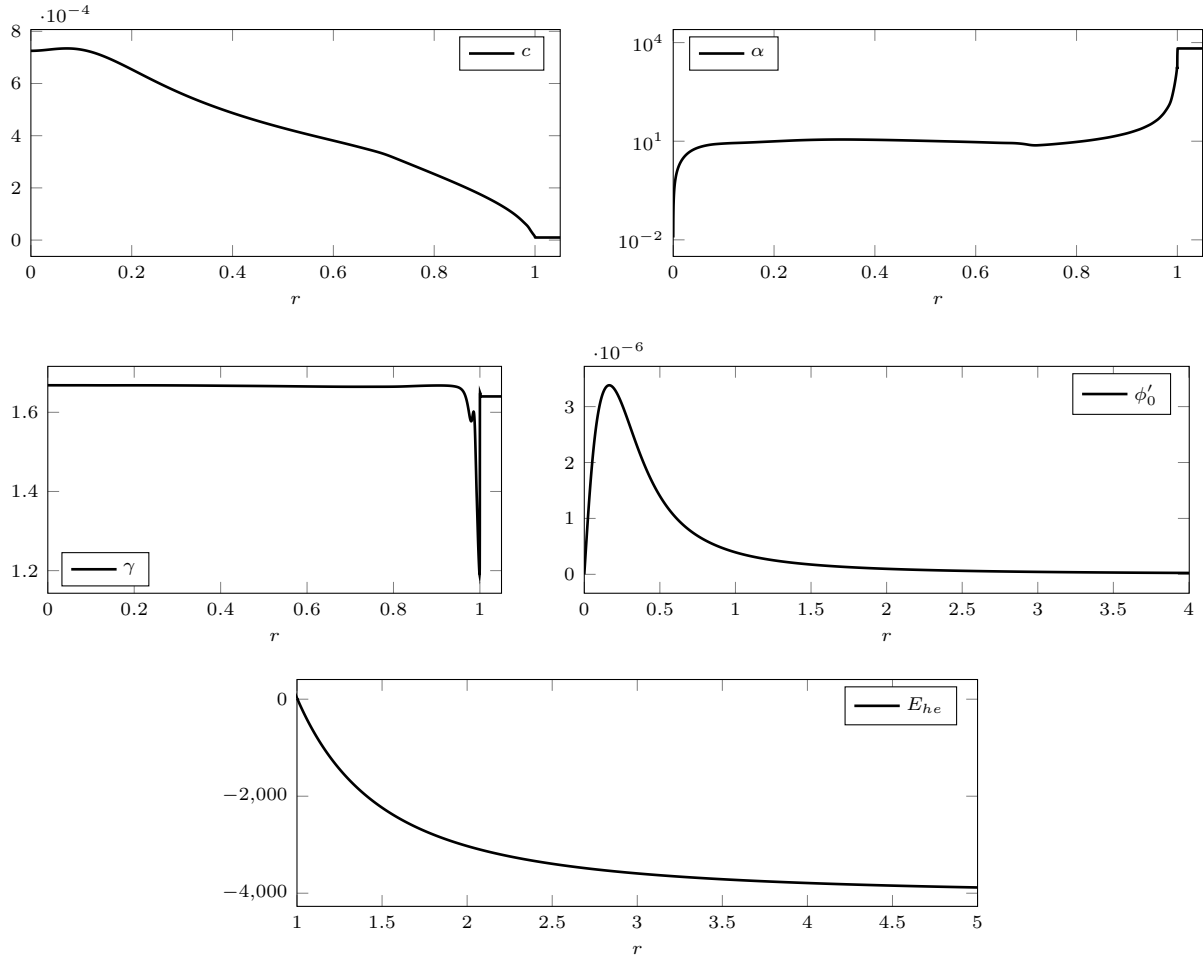


Figure 1: Solar background parameters from model S-AtmoI of [22] using $r_a = 1.00073$. Note that by definition, $E_{he} = 0$ in the interior while c , α and γ are constant for $r > r_a$.

Denote their coefficients in VSH basis (2.23) by

$$\begin{aligned}
 \mathbf{f} &= \sum_{\ell=0}^{\infty} \sum_{m=-\ell}^{\ell} f_{\ell}^m(r) \mathbf{P}_{\ell}^m(\hat{\mathbf{x}}) + \sum_{\ell=1}^{\infty} \sum_{m=-\ell}^{\ell} g_{\ell}^m(r) \mathbf{B}_{\ell}^m(\hat{\mathbf{x}}) + \sum_{\ell=1}^{\infty} \sum_{m=-\ell}^{\ell} h_{\ell}^m(r) \mathbf{C}_{\ell}^m(\hat{\mathbf{x}}) ; \\
 \boldsymbol{\xi} &= \sum_{\ell=0}^{\infty} \sum_{m=-\ell}^{\ell} a_{\ell}^m(r) \mathbf{P}_{\ell}^m(\hat{\mathbf{x}}) + \sum_{\ell=1}^{\infty} \sum_{m=-\ell}^{\ell} b_{\ell}^m(r) \mathbf{B}_{\ell}^m(\hat{\mathbf{x}}) + \sum_{\ell=1}^{\infty} \sum_{m=-\ell}^{\ell} c_{\ell}^m(r) \mathbf{C}_{\ell}^m(\hat{\mathbf{x}}).
 \end{aligned} \tag{3.10}$$

With F_0, F_{ℓ} defined in (2.19), define \mathfrak{f}_{ℓ}^m in terms of (f_{ℓ}^m, g_{ℓ}^m) by

$$\begin{aligned}
 \mathfrak{f}_{\ell}^m &:= R_{\odot}^2 \ell(\ell+1) \frac{r^{\frac{\alpha p_0}{\gamma}} - r \alpha \gamma p_0 - 1}{F_{\ell}} \frac{g_{\ell}^m}{\gamma p_0 \sqrt{\ell(\ell+1)}} \\
 &\quad + R_{\odot}^2 \frac{\ell(\ell+1)}{r} \partial_r \left(\frac{r^2}{F_{\ell}} \frac{1}{\gamma p_0} \frac{g_{\ell}^m}{\sqrt{\ell(\ell+1)}} \right) + R_{\odot}^2 \frac{f_{\ell}^m}{\gamma p_0}.
 \end{aligned} \tag{3.11}$$

Main results (Group 1) The coefficients in VSH basis of solution ξ and right-hand-side \mathbf{f} satisfy at each level (ℓ, m)

$$\left\{ \begin{array}{l} (\hat{q}_\ell \partial_r^2 + q_\ell \partial_r + \tilde{q}_\ell) a_\ell^m = \mathfrak{f}_\ell^m, \quad \text{with } \mathfrak{f}_\ell^m \text{ defined in (3.11),} \\ \hspace{15em} \text{and } \hat{q}_\ell, q_\ell, \tilde{q}_\ell \text{ in (3.29),} \\ \frac{\mathbf{b}_\ell^m}{\sqrt{\ell(\ell+1)}} = -\frac{r}{F_\ell} \partial_r a_\ell^m - \left(\frac{2}{r} - \frac{\alpha_{p_0}}{\gamma} \right) \frac{r}{F_\ell} a_\ell^m - \frac{r^2 R_\odot^2}{F_\ell \gamma p_0} \frac{g_\ell^m}{\sqrt{\ell(\ell+1)}}, \\ \mathbf{c}_\ell^m = -R_\odot^2 \frac{r^2}{\rho_0 c_0^2 F_0} h_\ell^m. \end{array} \right. \quad (3.12a)$$

$$\frac{\mathbf{b}_\ell^m}{\sqrt{\ell(\ell+1)}} = -\frac{r}{F_\ell} \partial_r a_\ell^m - \left(\frac{2}{r} - \frac{\alpha_{p_0}}{\gamma} \right) \frac{r}{F_\ell} a_\ell^m - \frac{r^2 R_\odot^2}{F_\ell \gamma p_0} \frac{g_\ell^m}{\sqrt{\ell(\ell+1)}}, \quad (3.12b)$$

$$\mathbf{c}_\ell^m = -R_\odot^2 \frac{r^2}{\rho_0 c_0^2 F_0} h_\ell^m. \quad (3.12c)$$

The coefficients b_ℓ^m are completely determined by a_ℓ^m and the coefficients of (f_ℓ^m, g_ℓ^m) of \mathbf{f} , while the equation for c_ℓ^m decouples from that for (a_ℓ^m, b_ℓ^m) . As a result of this, the only equation to focus on and solve is (3.12a) for a_ℓ^m .

Using the change of variable

$$\tilde{a}_\ell^m = \frac{a_\ell^m}{\mathfrak{I}_\ell}, \quad \text{with } \mathfrak{I}_\ell \text{ defined in (2.18),} \quad (3.13)$$

the modal ODE (3.12a), also called the *original* modal equation, is equivalent to the *conjugated* equation,

$$(-\partial_r^2 + V_\ell(r)) \tilde{a}_\ell^m = \frac{1}{\mathfrak{I}_\ell \hat{q}_\ell} \mathfrak{f}_\ell^m, \quad \text{with } V_\ell \text{ given in (3.34b).} \quad (3.14)$$

For convenience of discussion, we write the original modal operators in (3.12a) and conjugate modal operator in (3.14) as

$$\mathcal{L}_\ell := -\partial_r^2 + V_\ell(r), \quad \mathfrak{L}_\ell := \hat{q}_\ell \partial_r^2 + q_\ell \partial_r + \tilde{q}_\ell. \quad (3.15)$$

Remark 4. The change of unknown (3.13) also appears in [18, Equations (7.5) and (7.6)]. This is also used in order to reduce to a Schrödinger form the original ODE in variable ξ_r which contains a first order derivative, i.e. from equation (7.3) in (7.7) of [18]. In fact, in the interior, $E_{he} = 0$, their expression is equivalent to the one derived here except that they did not give the explicit expression of the term \tilde{q}_ℓ . The term \mathfrak{I}_ℓ is the square of the expression given in [18, Equation 7.5]. \diamond

Main results (Group 2) The second group of results of [6] is the characterization of outgoing kernels for \mathcal{L}_ℓ and \mathfrak{L}_ℓ , and their existence and uniqueness. Under assumption that ω is not an eigenvalue of \mathcal{L}_ℓ , there exists a unique regular-at-0 and outgoing at infinity distributional solution to

$$\mathfrak{L}_\ell G_\ell^+ = \delta(r-s). \quad (3.16)$$

This solution is denoted by $G_\ell^+(r, s)$ and is called the physical/outgoing Green's kernel for the conjugate operator \mathcal{L}_ℓ . The coefficients a_ℓ^m of solution $\xi \in L^2(\mathbb{R}^3)^3$ are then uniquely determined by (f_ℓ^m, g_ℓ^m) via operator G_ℓ^+ ,

$$\mathbf{a}_\ell^m(r) = \int_0^\infty G_\ell^+(r, s) \mathfrak{f}_\ell^m(s) ds, \quad \mathfrak{f}_\ell^m \text{ defined in (3.11).} \quad (3.17)$$

In [6, Section 7, Eq. (7.6)], this Green's kernel is constructed from the physical kernel \mathcal{G}_ℓ^+ ,

$$G_\ell^+(r, s) := -\frac{\mathfrak{I}_\ell(r)}{\mathfrak{I}_\ell(s) \hat{q}_\ell(s)} \mathcal{G}_\ell^+(r, s) = \frac{\mathfrak{I}_\ell(r)}{\mathfrak{I}_\ell(s)} \frac{F_\ell(s)}{F_0(s)} \mathcal{G}_\ell^+(r, s), \quad (3.18)$$

with the latter being the unique regular-at-0 and outgoing-at-infinity distributional solution to

$$\mathcal{L}_\ell \mathcal{G}_\ell^+ = \delta(r-s). \quad (3.19)$$

The boundary value problems solved by G_ℓ^+ and \mathcal{G}_ℓ^+ are listed in (3.80) and (3.86) and the existence and construction of solution are discussed in Subsection 3.3.

Remark 5 (First order system with $\xi_r - \delta_p$). *Instead of working entirely in variable ξ , most references in helioseismology (e.g., [17, 18, 10, 12]) work with a first-order ODE system (cf. (3.26)) derived in terms of the radial component of displacement and the Eulerian perturbation in pressure. In addition, note that these references consider the problem in the interior of the Sun on which the hydrostatic equilibrium (3.6), $E_{he} = 0$, is imposed. Under this condition, with δ_ρ , δ_p denoting the Eulerian perturbations in density and pressure respectively, equation (3.1) can be written as a system with unknowns $(\xi, \delta_\rho, \delta_p)$, cf. [6, Remark 2] and [5, Prop. 2 and Section 5.1],*

$$\begin{cases} -\rho_0 R_\odot^2 \sigma^2 \xi + \nabla \delta_p + \delta_p \nabla \phi_0 = R_\odot^2 \mathbf{f}, & (3.20a) \\ \delta_\rho = -(\nabla \rho_0) \cdot \xi - \rho_0 \nabla \cdot \xi, & (3.20b) \\ \delta_p = -\xi \cdot \nabla p_0 - \rho_0 c_0^2 \nabla \cdot \xi. & (3.20c) \end{cases}$$

Assume additionally that σ^2 is constant (equivalent to a constant attenuation Γ), system (3.20) implies the following system in terms of $(\xi_r, \delta_\rho, \delta_p)$, cf. [5, Section 5.1],

$$\begin{cases} -\sigma^2 \xi_r + \frac{\partial_r \delta_p}{\rho_0 R_\odot^2} + \frac{\phi'_0}{\rho_0 R_\odot^2} \delta_p = \frac{f_r}{\rho_0}, & (3.21a) \\ \sigma^2 \left(\frac{\delta_\rho}{\rho_0} + \frac{\rho'_0}{\rho_0} \xi_r + \partial_r \xi_r + \frac{2}{r} \xi_r \right) + \frac{\Delta_{S^2} \delta_p}{r^2 \rho_0 R_\odot^2} = \frac{\nabla_{S^2} \cdot \mathbf{f}_h}{r \rho_0}, & (3.21b) \\ c_0^2 \delta_\rho - \delta_p = \xi_r (p'_0 - c_0^2 \rho'_0). & (3.21c) \end{cases}$$

The above equations use the radial and tangential parts of \mathbf{f} , and the radial part of ξ ,

$$\mathbf{f} = f_r \mathbf{e}_r + \mathbf{f}_h, \quad \text{with } f_r = \mathbf{f} \cdot \mathbf{e}_r, \quad \xi_r = \xi \cdot \mathbf{e}_r. \quad (3.22)$$

Using (3.21c) to eliminate δ_ρ from (3.21a) and (3.21b), we obtain a system in terms of (ξ_r, δ_p)

$$\begin{cases} \left(-\sigma^2 + \frac{\phi'_0}{\rho_0 R_\odot^2} \left(\frac{p'_0}{c_0^2} - \rho'_0 \right) \right) \xi_r + \frac{\partial_r \delta_p}{\rho_0 R_\odot^2} + \frac{\phi'_0}{c_0^2 \rho_0 R_\odot^2} \delta_p = \frac{f_r}{\rho_0} & (3.23a) \\ \frac{\sigma^2}{c_0^2 \rho_0} \delta_p + \xi_r \sigma^2 \left(\frac{p'_0}{\gamma \rho_0} + \frac{2}{r} \right) + \sigma^2 \partial_r \xi_r + \frac{1}{r^2 \rho_0} \Delta_{S^2} \frac{\delta_p}{R_\odot^2} = \frac{\nabla_{S^2} \cdot \mathbf{f}_h}{r \rho_0}. & (3.23b) \end{cases}$$

Next, denote by a_ℓ^m and e_ℓ^m the coefficients of ξ_r and $\frac{\delta_p}{R_\odot^2}$ in scalar harmonic basis, i.e.,

$$\xi_r = \sum_{\ell=0}^{\infty} \sum_{m=-\ell}^{\ell} a_\ell^m Y_\ell^m, \quad \frac{\delta_p}{R_\odot^2} = \sum_{\ell=0}^{\infty} \sum_{m=-\ell}^{\ell} e_\ell^m Y_\ell^m. \quad (3.24)$$

With (f_ℓ^m, g_ℓ^m) the coefficients of \mathbf{f} in VSH basis as written in (3.10), we have

$$f_r = \sum_{\ell=0}^{\infty} \sum_{m=-\ell}^{\ell} f_\ell^m Y_\ell^m, \quad \nabla_{S^2} \cdot \mathbf{f}_h = - \sum_{\ell=1}^{\infty} \sum_{m=-\ell}^{\ell} \sqrt{\ell(\ell+1)} g_\ell^m Y_\ell^m. \quad (3.25)$$

System (3.23) with unknowns (ξ_r, δ_p) and rhs $(f_r, \nabla_{S^2} \cdot \mathbf{f}_h)$ decomposes on each mode ℓ to give a system in terms of unknown (e_ℓ^m, a_ℓ^m) with rhs (f_ℓ^m, g_ℓ^m) such that,

$$\begin{pmatrix} \frac{1}{\rho_0} & 0 \\ 0 & \sigma^2 \end{pmatrix} \partial_r \begin{pmatrix} e_\ell^m \\ a_\ell^m \end{pmatrix} + \mathbb{B} \begin{pmatrix} e_\ell^m \\ a_\ell^m \end{pmatrix} = \frac{1}{\rho_0} \begin{pmatrix} f_\ell^m \\ -\frac{\sqrt{\ell(\ell+1)}}{r} g_\ell^m \end{pmatrix}, \quad (3.26)$$

where the zero-th order operator \mathbb{B} is given by,

$$\mathbb{B} = \begin{pmatrix} \frac{\phi'_0}{\rho_0 c_0^2} & -\sigma^2 + \frac{\phi'_0}{\rho_0 R_\odot^2} \left(\frac{p'_0}{c_0^2} - \rho'_0 \right) \\ \frac{\sigma^2 R_\odot^2}{\rho_0 c_0^2} - \frac{\ell(\ell+1)}{r^2 \rho_0} & \sigma^2 \left(\frac{p'_0}{\gamma \rho_0} + \frac{2}{r} \right) \end{pmatrix} = \begin{pmatrix} \frac{\phi'_0}{\rho_0 c_0^2} & N^2 - \sigma^2 \\ \frac{\sigma^2 - S_\ell^2}{\rho_0 \frac{c_0^2}{R_\odot^2}} & \sigma^2 \left(\frac{p'_0}{\gamma \rho_0} + \frac{2}{r} \right) \end{pmatrix}. \quad (3.27)$$

The second form of \mathbb{B} is in terms of the buoyancy frequency N and the lamb frequency S_ℓ defined in (2.20) and (2.21). As noted in [6, Remark 2] and [5, Remark 12], the system (3.26) is equivalent to [18, Eqs. (5.12) and (5.13)] and [37, Eqs. (14.2) and (14.3)]. This is also the system employed to compute the Green's kernel in [10, 9], cf. [10, Eq. (A.10) or (A.14)]. \diamond

3.1 Coefficients of the modal ODEs

We list here the explicit expressions for the coefficients of the conjugated modal operator \mathcal{L}_ℓ and of the original modal operator \mathfrak{L}_ℓ introduced in (3.12a) and (3.14). These results were obtained in [6, Section 4]. They are recited here in the notation given in Section 2. The main quantities of these expressions are F_ℓ , F_0 in (2.19), k_0 in (2.16), E_{he} in (2.8), the gravitational potential ϕ_0 in (2.5), and the inverse scale height α_\bullet in (2.7).

Coefficients of the original reduced ODE \mathfrak{L}_ℓ The coefficients of this operator are, cf. [6, Proposition 5], for $\ell = 0$,

$$\hat{q}_0 = -1, \quad q_0 = \alpha_{\gamma p_0} - \frac{2}{r}, \quad \tilde{q}_0 = -k_0^2 + \frac{\phi_0''}{c_0^2} + \frac{2}{r^2} + \frac{2(\alpha_{\gamma p_0} - \frac{\alpha_{p_0}}{\gamma})}{r}, \quad (3.28)$$

and for $\ell > 0$

$$\hat{q}_\ell = -\frac{F_0}{F_\ell}; \quad q_\ell = \left(\alpha_{\gamma p_0} - \frac{2}{r} \right) \frac{F_0}{F_\ell} + \ell(\ell+1) \frac{F_0'}{(F_\ell)^2}; \quad (3.29a)$$

$$\begin{aligned} \tilde{q}_\ell = & \left(-k_0^2 + \frac{\phi_0''}{c_0^2} + \frac{2}{r^2} + \frac{2(\alpha_{\gamma p_0} - \frac{\alpha_{p_0}}{\gamma})}{r} \right) \frac{F_0}{F_\ell} + \ell(\ell+1) \left(\frac{2}{r} - \frac{\alpha_{p_0}}{\gamma} \right) \frac{F_0'}{(F_\ell)^2} \\ & + \frac{\ell(\ell+1)}{F_\ell} \left(k_0^2 - \frac{\phi_0''}{c_0^2} + \left(\frac{\alpha_{p_0}}{\gamma} \right)' + \frac{\alpha_{p_0}}{\gamma} \left(-\alpha_{\gamma p_0} + \frac{\alpha_{p_0}}{\gamma} \right) \right). \end{aligned} \quad (3.29b)$$

We can define a quantity called buoyancy squared wavenumber $k_{\mathcal{N}}^2$ ²

$$-k_{\mathcal{N}}^2(r) = -E'_{\text{he}} + E_{\text{he}} \left(2\alpha_{c_0} + R_\odot^2 \frac{N^2}{\phi_0'} \right) - R_\odot^2 \frac{N^2}{c_0^2} \quad (3.31a)$$

$$= -\frac{\phi_0''}{c_0^2} + \left(\frac{\alpha_{p_0}}{\gamma} \right)' + \frac{\alpha_{p_0}}{\gamma} \left(-\alpha_{\gamma p_0} + \frac{\alpha_{p_0}}{\gamma} \right). \quad (3.31b)$$

²The equivalence of the expressions (3.31a) and (3.31b) as seen as follows. From the definition of E_{he} in (2.8), we obtain the following expression for its derivative,

$$E'_{\text{he}} = \frac{\phi_0''}{c_0^2} - \left(\frac{\alpha_{p_0}}{\gamma} \right)' + \frac{\phi_0'}{c_0^2} \alpha_{c_0} = \frac{\phi_0''}{c_0^2} - \left(\frac{\alpha_{p_0}}{\gamma} \right)' + \left(E_{\text{he}} + \frac{\alpha_{p_0}}{\gamma} \right) \alpha_{c_0}. \quad (3.30)$$

We then use (3.30) to replace the first two terms in expression (3.31b) in terms of E'_{he} ,

$$\begin{aligned} \text{rhs of (3.31b)} &= -E'_{\text{he}} + \left(E_{\text{he}} + \frac{\alpha_{p_0}}{\gamma} \right) \alpha_{c_0}^2 + \left(\frac{\alpha_{p_0}}{\gamma} \right)^2 - \frac{\alpha_{p_0}}{\gamma} \alpha_{c_0}^2 - \frac{\alpha_{p_0}}{\gamma} \alpha_{\rho_0} \\ &= -E'_{\text{he}} + 2E_{\text{he}} \alpha_{c_0} + \frac{\alpha_{p_0}}{\gamma} \left(\frac{\alpha_{p_0}}{\gamma} - \alpha_{\rho_0} \right) \\ &= -E'_{\text{he}} + 2E_{\text{he}} \alpha_{c_0} - \left(-E_{\text{he}} + \frac{\phi_0'}{c_0^2} \right) \frac{R_\odot^2 N^2}{\phi_0'} = \text{rhs of (3.31a)}. \end{aligned}$$

We have used the following substitution from the definition of N^2 (2.21), which gives $N^2 \frac{R_\odot^2}{\phi_0'} = \alpha_{\rho_0} - \frac{\alpha_{p_0}}{\gamma}$, and E_{he} (2.8) which gives $\frac{\alpha_{p_0}}{\gamma} = -E_{\text{he}} + \frac{\phi_0'}{c_0^2}$.

Note that $k_{\mathcal{N}}^2$ reduces to $R_{\odot}^2 \frac{N^2}{c_0^2}$ in the interior ($r \leq r_s$) where $E_{\text{he}} = 0$. For $\ell > 0$, we can write \tilde{q}_{ℓ} to make appear $k_{\mathcal{N}}^2$ as³

$$\tilde{q}_{\ell} = -k_0^2 + k_{\mathcal{N}}^2 + \mathbf{g}^D \frac{F_0}{F_{\ell}} + \ell(\ell+1) \left(\frac{2}{r} - \frac{\alpha_{p_0}}{\gamma} \right) \frac{F_0'}{(F_{\ell})^2}, \quad (3.32)$$

with

$$\mathbf{g}^D(r) = \frac{2}{r^2} + 2 \frac{\frac{\alpha_{p_0}}{\gamma} - \alpha_{\gamma p_0}}{r} + \left(\frac{\alpha_{p_0}}{\gamma} \right)' + \frac{\alpha_{p_0}}{\gamma} \left(-\alpha_{\gamma p_0} + \frac{\alpha_{p_0}}{\gamma} \right). \quad (3.33)$$

Coefficients of conjugated modal operator \mathcal{L}_{ℓ} An important feature of \mathcal{L}_{ℓ} is the appearance of the new wave function k^2 , and the coefficient function η , introduced in (2.17),

$$-k^2 := \frac{\alpha_{\gamma p_0}^2}{4} - \frac{\alpha'_{\gamma p_0}}{2} - k_0^2, \quad \eta := 2 \frac{\alpha_{p_0}}{\gamma} - \alpha_{\gamma p_0}.$$

We will list the most important variants of potential V_{ℓ} . In the first variant,

$$V_0(r) = -k^2(r) + \frac{\phi_0''(r)}{c_0^2(r)} - \frac{\eta(r)}{r} + \frac{2}{r^2}, \quad (3.34a)$$

$$V_{\ell}(r) = -k^2(r) + \frac{\phi_0''(r)}{c_0^2(r)} - \eta(r) \mathbf{v}_{\ell}(r) + \frac{\ell(\ell+1)}{r^2} \mathbf{w}_{\ell}(r) + \frac{[\ell(\ell+1)]^2}{4} \mathbf{t}_{\ell}^2(r), \quad \ell > 0, \quad (3.34b)$$

where in addition to k and η , we have auxiliary functions for $\ell > 0$,

$$\mathbf{v}_{\ell} := \frac{F_0/r}{F_{\ell}}; \quad \mathbf{t}_{\ell} := \frac{1}{F_{\ell}} \frac{F_0'}{F_0}; \quad (3.35a)$$

$$\mathbf{w}_{\ell}(r) := 1 + \underbrace{\frac{rE_{\text{he}} - r^2 k_{\mathcal{N}}^2}{F_0}}_{\frac{r^2(k_0^2 - k_{\mathcal{N}}^2)}{F_0}} + \frac{2r}{\ell(\ell+1)} \mathbf{v}_{\ell} + \left(1 - \frac{\eta}{2} r \right) \left(r \mathbf{t}_{\ell} - \frac{2}{F_{\ell}} \right) - \frac{r^2}{2} \mathbf{t}_{\ell}'. \quad (3.35b)$$

In chosen form (3.34b), these global functions are bounded and continuous, in particular,

$$k^2, \eta, \mathbf{v}_{\ell} - \frac{1}{r}, \mathbf{w}_{\ell}, \mathbf{t}_{\ell} \in C^2([0, \infty]) \cap L^{\infty}([0, \infty)), \text{ for } \Gamma > 0. \quad (3.36)$$

The limit of the wave function k^2 at infinity gives the ‘energy level’ of the system, while that of η is the coefficient of the Coulomb-type potential, which is the slowest decay potential part of V_{ℓ} . This is discussed further in the scattering-theory format (3.67) of V_{ℓ} .

Following the discussion of [6, Section 5.1], the second variant of V_{ℓ} is,

$$V_{\ell}(r) = -\frac{\sigma^2(r) - \omega_c^2(r)}{\left(\frac{c_0(r)}{R_{\odot}} \right)^2} + k_{\text{h}}^2(r). \quad (3.37)$$

This is in terms of the local cut-off frequency defined as,

$$\frac{\omega_c^2(r)}{c_0^2(r)} := \frac{1}{R_{\odot}^2} \left(\frac{\alpha_{\gamma p_0}^2(r)}{4} - \frac{\alpha'_{\gamma p_0}(r)}{2} + \frac{\phi_0''(r)}{c_0^2(r)} - \frac{\eta(r)}{r} + \frac{2}{r^2} \right), \quad (3.38)$$

and the (local) horizontal wavenumber function k_{h}^2 defined as,

$$k_{\text{h}}^2 = 0, \quad \text{for } \ell = 0, \\ k_{\text{h}}^2 = \frac{\ell(\ell+1)}{r^2} \left(1 + \frac{rE_{\text{he}} - r^2 k_{\mathcal{N}}^2}{F_0} - \frac{r^2 \eta \mathbf{t}_{\ell}}{2} + r \mathbf{t}_{\ell} - \frac{r^2 \mathbf{t}_{\ell}'}{2} + \frac{\ell(\ell+1)}{4} (r \mathbf{t}_{\ell})^2 \right), \quad \ell > 0. \quad (3.39)$$

³The expression (3.29b) of \tilde{q}_{ℓ} can be rewritten as

$$\tilde{q}_{\ell} = \left(-k_0^2 + \frac{\phi_0''}{c_0^2} + \frac{2}{r^2} - 2 \frac{\frac{\alpha_{p_0}}{\gamma} - \alpha_{\gamma p_0}}{r} \right) \frac{F_0}{F_{\ell}} + \frac{\ell(\ell+1)}{F_{\ell}} \left(k_0^2 - k_{\mathcal{N}}^2 + \left(\frac{2}{r} - \frac{\alpha_{p_0}}{\gamma} \right) \frac{F_0'}{F_{\ell}} \right) = \text{rhs of (3.32)}.$$

The current notation suppresses the dependence of k_h^2 on ℓ . See also [Figure 3](#) for an illustration for ω_c . This figure also gives a comparison with the local cut-off frequency of the scalar equation recalled in [Remark 6](#).

In addition to the above variants provided in [\[6\]](#), we introduce here a third variant of V_ℓ which is inspired from the Whittaker's equation format of modal scalar equation studied in previous work (recalled below in [Remark 6](#)),

$$V_\ell = -k^2 + \frac{\phi_0''}{c_0^2} - \frac{\eta}{r} + \frac{\nu_\ell^2 - \frac{1}{4}}{r^2}, \quad (3.40)$$

where we have introduced the index $\nu_\ell(r)$

$$\begin{aligned} \nu_0^2(r) - \frac{1}{4} &= 2, \\ \ell > 0, \quad \nu_\ell^2(r) - \frac{1}{4} &= \ell(\ell+1) \mathfrak{w}_\ell(r) - \eta(r) (r^2 \mathfrak{v}_\ell(r) - r) + \left(\frac{\ell(\ell+1) r \mathfrak{t}_\ell(r)}{2} \right)^2. \end{aligned} \quad (3.41)$$

This will be useful in constructing radiation boundary conditions in [Section 6](#).

Remark 6 (Comparison with the scalar-wave equation in helioseismology). *Throughout the work, we carry out comparison with the scalar equation*

$$\mathfrak{L}_{\text{scalar}} = -\nabla \cdot \frac{1}{\rho_0} \nabla - \frac{k_0^2}{\rho_0}. \quad (3.42)$$

As mentioned in the introduction, this equation offers a simplified alternative to study acoustic waves in helioseismology and was employed in [\[26, 24, 2\]](#). In [\[8, 3\]](#), we studied the equivalent of $\mathfrak{L}_{\text{scalar}}$ in Schrödinger form,

$$\mathcal{L}_{\text{scalar}} := -\Delta - k_0^2 + \rho_0^{-1/2} \Delta \rho_0^{1/2} = -\Delta - k_0^2 + \frac{\alpha_{\rho_0}^2}{r} + \frac{\alpha'}{2} + \frac{\alpha}{r}. \quad (3.43)$$

The physical solution u to $\mathcal{L}_{\text{scalar}} u = \rho_0^{1/2} \nabla \cdot \mathbf{f}$ serves as an approximate solution to $\rho_0^{1/2} c_0^2 \nabla \cdot \boldsymbol{\xi}$ with $(\boldsymbol{\xi}, \mathbf{f})$ the solution and rhs pair of \mathcal{L}_{SG} [\(3.1\)](#). We refer to [\[7, Remark 1\]](#) for the derivation of $\mathcal{L}_{\text{scalar}}$ and $\mathfrak{L}_{\text{scalar}}$ from \mathcal{L}_{SG} .

The modal operators (conjugate by r^{-1}) of $\mathcal{L}_{\text{scalar}}$ is denoted by \mathbb{L}_ℓ with

$$\mathbb{L}_\ell^{\text{scalar}} := -\partial_r^2 - k_0^2 + \frac{\alpha_{\rho_0}^2}{4} + \frac{\alpha'_{\rho_0}}{2} + \frac{\alpha_{\rho_0}}{r} + \frac{\ell(\ell+1)}{r^2} = -\partial_r^2 + V_\ell^{\text{scalar}}, \quad (3.44)$$

where the associated potential is

$$\begin{aligned} V_\ell^{\text{scalar}} &:= -k_0^2 + \frac{\alpha_{\rho_0}^2}{4} + \frac{\alpha'_{\rho_0}}{2} + \frac{\alpha_{\rho_0}}{r} + \frac{\ell(\ell+1)}{r^2} \\ &= -k_{\text{scalar}}^2 + \frac{\alpha_{\rho_0}}{r} + \frac{\ell(\ell+1)}{r^2}. \end{aligned} \quad (3.45)$$

The associated wavenumbers are

$$\begin{aligned} [k_h^{\text{scalar}}]^2 &= \frac{\ell(\ell+1)}{r^2} \geq 0, & [\omega_c^{\text{scalar}}]^2 &= \frac{1}{R_\odot^2} \left(\frac{\alpha_{\rho_0}^2}{4} + \frac{\alpha'_{\rho_0}}{2} + \frac{\alpha_{\rho_0}}{r} \right), \\ k_{\text{scalar}}^2 &= k_0^2 - \frac{\alpha_{\rho_0}^2}{4} - \frac{\alpha'_{\rho_0}}{2}. \end{aligned} \quad (3.46)$$

Note that the imaginary part of the square horizontal wavenumber k_h [\(3.39\)](#) is nonzero (since k_h^2 can be negative), while k_h^{scalar} is always real. A comparison for the local cut-off frequencies is given in [Figure 3](#). We note that, despite their difference in their local value, they have the same limiting value in the high atmosphere given by $\omega_t/(2\pi) = 5.20$ mHz. \diamond

3.2 Properties of the modal ODEs

3.2.1 Singularities

Nonzero singularity points Recall that

$$F_\ell := k_0^2 r^2 - r E_{\text{he}} - \ell(\ell + 1), \quad k_0^2 = \frac{\omega^2 R_\odot^2}{c_0^2} \text{ when } \Gamma = 0.$$

Under the assumption stated in (3.5), the algebraic equation

$$F_\ell(r, \omega) = 0 \quad \text{at } \Gamma = 0, \quad (3.47)$$

in terms of r, ω , and ℓ , can be used to define implicitly one quantity in terms of the other two. In particular, for each fixed ℓ and ω , the relation (3.47) is used in [6] to define $r_{\omega, \ell}^* = r_*(\omega, \ell)$ as the unique zero of F_ℓ , i.e.

$$F_\ell(r_{\omega, \ell}^*; \omega) = 0. \quad (3.48)$$

The value $r_{\omega, \ell}^*$ contributes to the non-zero singularity of the coefficients of \mathfrak{L}_ℓ and \mathcal{L}_ℓ for $\ell > 0$, see below discussion in (3.54) and (3.99) and (3.100), as well as the function \mathfrak{I}_ℓ (2.18) which gives the equivalence (3.13) between solution with \mathfrak{L} and \mathcal{L} and whose definition we recall here,

$$\mathfrak{I}_\ell(r) = \frac{1}{r c_0 \sqrt{\rho_0}} \frac{\sqrt{F_\ell}}{\sqrt{F_0}} = \frac{1}{r c_0 \sqrt{\rho_0}} \frac{\sqrt{\sigma^2 - S_\ell^2 - \frac{E_{\text{he}} c_0^2}{r R_\odot^2}}}{\sqrt{\sigma^2 - \frac{E_{\text{he}} c_0^2}{r R_\odot^2}}}.$$

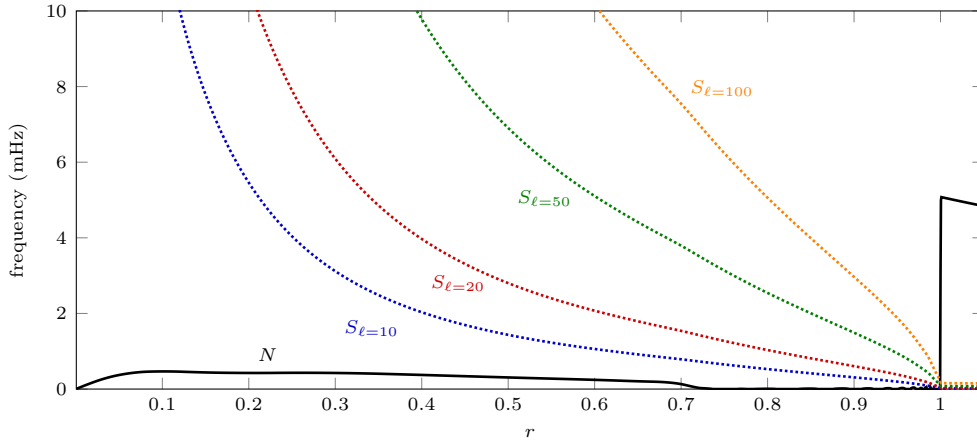


Figure 2: Lamb and Brunt-Väisälä frequencies, respectively S_ℓ and N in (2.20) and (2.21), associated to the solar model S-AtmoI.

We next comment on the position of $r_{\omega, \ell}^*$ in particular with respect to r_s (the surface of the Sun). For a frequency ω , define the harmonic mode,

$$\ell_\omega^* := -\frac{1}{2} + \sqrt{\frac{\omega^2}{\left(\frac{c_0(r_s)}{R_\odot}\right)^2} r_s^2 + \frac{1}{4}}. \quad (3.49)$$

We have

$$\ell < \ell_\omega^* \Rightarrow r_{\omega, \ell}^* \in [0, r_s] \quad \text{and} \quad \ell > \ell_\omega^* \Rightarrow r_{\omega, \ell}^* > r_s. \quad (3.50)$$

If $\ell_\omega^* \in \mathbb{N}$, for $\ell = \ell_\omega^*$, then $r_{\omega, \ell}^* = r_s$. For the low ω and high ℓ , $r_{\omega, \ell}^*$ is close to r_s , which is close to r_{max} (the end of the simulation domain). In these cases, r_{max} being close to $r_{\omega, \ell}^*$ can create numerical instability at low attenuation. See further discussion in Remark 16.

Remark 7 (Lamb frequency). Using (3.47), for fixed ℓ and r , we define a generalized Lamb frequency $S_\ell(r)$,

$$S_\ell(r) := (rE_{he} + \ell(\ell + 1)) \frac{c_0^2}{r^2 R_\odot^2}. \quad (3.51)$$

Since expression F_ℓ can be written as

$$F_\ell = \frac{r^2 R_\odot^2}{c_0^2} (\sigma^2 - S_\ell(r)), \quad (3.52)$$

definition (3.51) is equivalent to defining S_ℓ as the unique zero of (3.47), i.e.

$$F_\ell(r; S_\ell(r)) = 0. \quad (3.53)$$

In the interior of the Sun, under hydrostatic equilibrium, $E_{he} = 0$, the quantity S_ℓ reduces to the usual definition of the Lamb frequency (2.20), since the two quantities are related by

$$S_\ell^2 = S_\ell^2 + \frac{E_{he}}{r} \frac{c_0^2}{R_\odot^2}, \quad \text{thus} \quad S_\ell = S_\ell \quad \text{when} \quad r \leq r_s \quad (\text{where } E_{he} = 0).$$

In this perspective, instead of fixing (ω, ℓ) and defining singular position in terms of r , one can instead fix (r, ℓ) and define a singular frequency. As pointed out in Remark 4, in the interior $E_{he} = 0$ and the expression \mathfrak{I}_ℓ is the squared of the expression given in [18, Equation 7.5]. The singularity of this expression occurs at $r = r_{\omega, \ell}^*$ given (ω, ℓ) or at $\omega = S_\ell$ given (r, ℓ) . The singularity of \mathfrak{I}_ℓ at the Lamb frequency for $r \leq r_s$ is noted in [18, Section 7.1 p.129]. Furthermore, the Lamb frequency is a good approximation of the lower turning point of the p -modes. \diamond

Indicial analysis for the conjugate equation \mathcal{L}_ℓ This result is cited from [6, Section 5.1]. The useful information from this analysis are the position of singularities and their indicial exponents, denoted below by λ^\pm and κ^\pm , which are used to infer the structure of the homogeneous solutions, written in (3.99)–(3.101). From [6, Proposition 8], we have, when $(\ell = 0, \Gamma \geq 0)$, or $(\Gamma > 0, \ell > 0)$, that $r = 0$ is the only regular singular point of V_ℓ . When $(\Gamma = 0, \ell > 0)$, in addition to $r = 0$, \mathcal{L}_ℓ has an additional unique singular point $r_{\omega, \ell}^*$. Specifically,

$$\lim_{r \rightarrow 0} r^2 V_0 = 2; \quad (3.54a)$$

$$\text{while for } \ell > 0, \quad \lim_{r \rightarrow 0} r^2 V_\ell = \ell(\ell + 1); \quad (3.54b)$$

$$\text{and } \ell > 0, \Gamma = 0, \quad \lim_{r \rightarrow r_{\omega, \ell}^*} (r - r_{\omega, \ell}^*)^2 V_\ell = \frac{3}{4}. \quad (3.54c)$$

The indicial exponents of $r = 0$ for \mathcal{L}_ℓ are

$$\kappa_0^+ = 2, \kappa_0^- = -1; \quad \kappa_\ell^+ = \ell + 1, \kappa_\ell^- = -\ell, \quad \text{for } \ell > 0, \quad (3.55)$$

while that of $r_{\omega, \ell}^*$ are independent of ℓ with value,

$$\kappa_\star^+ = \frac{3}{2}, \quad \kappa_\star^- = -\frac{1}{2}. \quad (3.56)$$

Indicial analysis for the original equation \mathfrak{L}_ℓ We have a similar statement for \mathfrak{L}_ℓ , i.e. when $(\ell = 0, \Gamma \geq 0)$, or $(\Gamma > 0, \ell > 0)$, $r = 0$ is the only regular singular point, and when $(\Gamma = 0, \ell > 0)$, in addition to $r = 0$, \mathfrak{L}_ℓ has an additional unique singular point $r_{\omega, \ell}^*$. Explicitly,

$$\lim_{r \rightarrow 0} r \frac{q_0}{\hat{q}_0} = 2, \quad \lim_{r \rightarrow 0} r^2 \frac{\tilde{q}_0}{\hat{q}_0} = -2, \quad (3.57)$$

while for $\ell > 0$, cf. [6, Proposition 7],

$$\ell > 0, \quad \lim_{r \rightarrow 0} r \frac{q_\ell}{\hat{q}_\ell} = 4 \quad ; \quad \lim_{r \rightarrow 0} r^2 \frac{\tilde{q}_\ell}{\hat{q}_\ell} = 2 - \ell(\ell + 1); \quad (3.58a)$$

$$\ell > 0, \Gamma = 0, \quad \lim_{r \rightarrow r_{\omega, \ell}^*} (r - r_{\omega, \ell}^*) \frac{q_\ell}{\hat{q}_\ell} = -1 \quad ; \quad \lim_{r \rightarrow r_{\omega, \ell}^*} (r - r_{\omega, \ell}^*)^2 \frac{\tilde{q}_\ell}{\hat{q}_\ell} = 0. \quad (3.58b)$$

The indicial exponent of singular point $r = 0$ associated to \mathfrak{L}_ℓ is

$$\lambda_0^+ = 1, \lambda_0^- = 2; \quad \lambda_\ell^+ = \ell - 1, \quad \lambda_\ell^- = -\ell - 2, \quad \text{for } \ell > 0, \quad (3.59)$$

and that of singular point $r_{\omega, \ell}^*$ is, cf. [6, Proposition 8]

$$\lambda_\star^+ = 2, \quad \lambda_\star^- = 0. \quad (3.60)$$

3.2.2 Growth and decay when r tends to infinity

Constancy in high atmosphere Equations (3.7) and (3.8) of Assumption 1 lead to the constancy on $r \geq r_a$ of the following quantities,

$$\begin{aligned} k_0(r) &= k_a, & \alpha_{\rho_0}(r) &= \alpha_{p_0}(r) = \alpha_{\gamma p_0}(r) = \alpha_a, \\ \alpha'_{\rho_0}(r) &= \alpha'_{p_0}(r) = \alpha'_{\gamma p_0}(r) = 0. \end{aligned} \quad (3.61)$$

This also implies the constancy for function k and η introduced in (2.17) in this region,

$$k^2(r) = k_a^2, \quad \eta(r) = \eta_a, \quad r \geq r_a, \quad (3.62)$$

with constants

$$k_a^2 := k_a^2 - \frac{\alpha_a^2}{4}, \quad \eta_a := \frac{\alpha_a}{\gamma_a} (2 - \gamma_a). \quad (3.63)$$

We also introduce the limiting/constant cut-off frequency ω_t which is defined as the limit in high atmosphere of the local cut-off wavenumber ω_c (3.38),

$$\omega_t := \lim_{r \rightarrow \infty} \omega_c. \quad (3.64)$$

In terms of the constants in (3.7), it takes value⁴

$$\omega_t := \frac{\alpha_a c_a}{2R_\odot}. \quad (3.66)$$

The value of ω_t associated with the model **S-AtmoI** is 5.20 mHz. Other meanings of k_a and ω_c are discussed in (3.68) and (3.72). We further compare the cut-off frequencies of the vector and scalar problems in Figure 3.

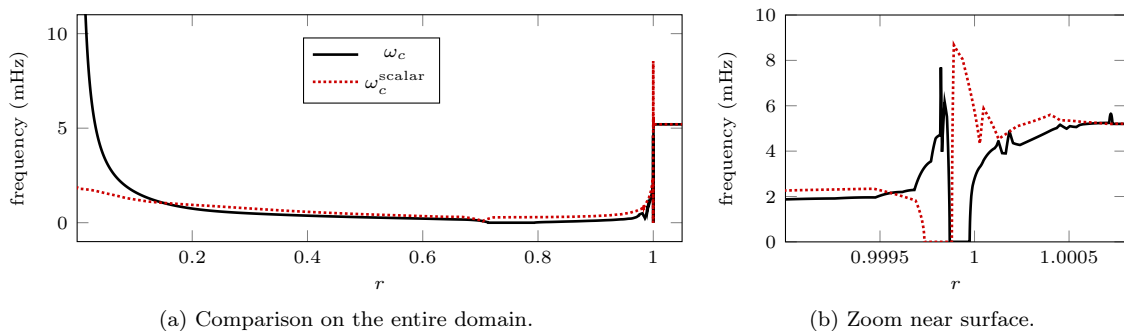


Figure 3: Comparison of the cut-off frequency for the vector problem, ω_c of (3.38), with the cut-off frequency associated with the scalar problem, ω_c^{scalar} of (3.46).

⁴In fact, ω_t has the asymptotic relation, cf. [6, Proposition 9],

$$\omega_c^2(r) = \omega_t^2 - \frac{\eta_a}{r} \left(\frac{c_a}{R_\odot} \right)^2 + 2 \left(\frac{c_a}{rR_\odot} \right)^2 - \frac{2Gm}{r^3} + \begin{matrix} \text{analytic and} \\ \text{exponentially decaying,} \\ \text{term} \end{matrix}, \quad r \geq r_a. \quad (3.65)$$

Scattering theory decomposition of V_ℓ In scattering theory⁵, one is interested in the decay or growth rate of the potential V_ℓ as $r \rightarrow \infty$. We are in the case of a potential that is non-growing, non-oscillatory and has finite limit at infinity. This limit is related to the energy of the system and determines the period of oscillation of the modal solutions (i.e. $\mathcal{L}_\ell w = 0$ or $\mathfrak{L}_\ell w = 0$). After subtracting out the energy, the remaining potential (also called normalized) is then decomposed into a long-range part which decays slower than or at the rate of r^{-1} , and a short-range one which decays faster than r^{-1} . The explicit decomposition which contains three parts is as follows,

$$V_\ell = \underbrace{-k_a^2}_{\text{energy level}} + \underbrace{\mathcal{V}(r)}_{\substack{\text{long-range potential} \\ \text{independent of } \ell}} + \underbrace{\frac{\mathcal{W}_\ell(r)}{r^2}}_{\substack{\text{short-range potential} \\ \text{dependent on } \ell}}, \quad (3.67)$$

where k_a^2 is called the energy level of the system the limiting value of $-V_\ell$

$$k_a^2 = \lim_{r \rightarrow \infty} -V_\ell, \quad (3.68)$$

and \mathcal{V} is a potential independent of ℓ , continuous on $[0, \infty)$ and long-range, which is in this case of Coulomb-type (i.e. dominantly behaves like $\frac{\text{constant}}{r}$).

We note that (3.68) provides a more appropriate definition of k_a^2 , which in fact takes value (3.63) for our particular V_ℓ (3.34b). The component $-k_a^2 + \mathcal{V}$ in (3.67) is important since it determines⁶ the oscillatory phase function ψ , which has the asymptotic relation,

$$\psi \sim i k_a, \quad r \rightarrow \infty.$$

Explicitly, $e^{i\psi}$ constitutes the structure of modal solutions as $r \rightarrow \infty$, and for a homogeneous solution w satisfying $\mathcal{L}_\ell w = 0$, then for some constant a, b (with l.o.t abbreviation for lower order terms),

$$w \sim e^{i\psi}(a + \text{l.o.t}) + e^{-i\psi}(a + \text{l.o.t}), \quad r \rightarrow \infty.$$

Additionally, at zero attenuation, $k = 0$ marks the transition between the oscillatory regime and the exponential decay regime of homogeneous modal solutions, cf. Remark 9. More detailed discussion is given in Subsection 3.3 for the construction of outgoing solutions.

A choice for the long-range part in the decomposition (3.67) is

$$\mathcal{V}(r) := k_a^2 - k^2(r) + \frac{\phi_0''(r)}{c_0^2(r)} - \frac{\eta(r)}{r+1}. \quad (3.69)$$

This also determines \mathcal{W}_ℓ of short-range potential $\frac{\mathcal{W}_\ell}{r^2}$, which in terms of the auxiliary functions ($\mathbf{v}_\ell, \mathbf{q}_\ell, \mathbf{t}_\ell$) in (3.35), is given by,

$$\mathcal{W}_0 = 2 - \eta \frac{r}{r+1} = 2 - r^2 \eta \left(\mathbf{v}_0 - \frac{1}{r+1} \right), \quad \text{since } \mathbf{v}_0 = \frac{1}{r}; \quad (3.70a)$$

$$\mathcal{W}_\ell = \ell(\ell+1) \mathbf{w}_\ell - r^2 \eta \left(\mathbf{v}_\ell - \frac{1}{r+1} \right) + \frac{[\ell(\ell+1)]^2}{4} (r \mathbf{t}_\ell)^2, \quad \ell > 0. \quad (3.70b)$$

Remark 8. The gravitation potential ϕ_0'' is a short-ranged potential with asymptotics, cf. [6, Equation 6.2],

$$\phi_0'' = -2 \frac{2G R_\odot^2}{r^3} \mathbf{m} + \text{a.e.d.t}, \quad r \geq r_a, \quad (3.71)$$

with constant $\mathbf{m} := 4\pi \int_0^{r_a} s^2 \rho_0(s) ds + 4\pi \rho_0(r_a) \frac{(\alpha_a r_a)^2 + 2r_a \alpha_a + 2}{(\alpha_a)^2}$.

Here, a.e.d.t stands for analytic and exponentially decaying term. The term $\frac{\phi_0''}{c_0^2}$ in (3.40) can thus be grouped as part of the long-range potential due to its independence of ℓ , as is done in (3.69), or it can simply be grouped with the short-range one. \diamond

⁵We refer to [5] for more details on scattering theory.

⁶This appears in the eikonal equation (3.76) which ψ satisfies.

Remark 9. *The following expression of k^2 shines light on the meaning of ω_t as a borderline frequency marking the transition between oscillatory and decay in high atmosphere,*

$$k_a^2 = \frac{\omega^2 - \omega_t^2}{\left(\frac{c_a}{R_\odot}\right)^2} + i \frac{2\omega\Gamma_a}{\left(\frac{c_a}{R_\odot}\right)^2}. \quad (3.72)$$

We have

$$(\Gamma = 0, r \geq r_a) \quad \implies \quad (k_a^2 = 0 \Leftrightarrow \omega = \omega_t). \quad (3.73)$$

This means that at zero attenuation and in high atmosphere, $k_a^2 = 0$ which corresponds to ω taking value ω_t marks the transition of the modal solutions from oscillatory to exponential decay. \diamond

The structure of V_ℓ in high atmosphere is further studied in [Subsection 6.1](#) where approximations of V_ℓ for $r \geq r_a$ are computed. These approximations serve to construct the impedance coefficient in radiation boundary conditions in [Section 6](#).

3.3 Existence and uniqueness of the outgoing modal Green's kernel

With ω_t defined in [\(3.66\)](#) and its meaning discussed in [Remark 9](#), under the assumption that

$$\Gamma > \delta' > 0, \quad 0 < \delta < \omega \neq \omega_t, \quad (3.74)$$

the set of singular points consists only of $r = 0$, and we stay away from the ‘energy threshold’ of scattering theory.

Results for the conjugate modal ODE \mathcal{L}_ℓ We have three main results

1. With κ_ℓ^+ given in [\(3.55\)](#), the first result gives the existence and uniqueness of solution φ_ℓ to

$$\begin{aligned} (-\partial_r^2 + V_\ell) \varphi_\ell &= 0, \quad r \in (0, \infty) \\ \text{satisfying } \varphi_\ell(r) &= r^{\kappa_\ell^+} (1 + o(1)), \quad \text{as } r \rightarrow 0. \end{aligned} \quad (3.75)$$

2. Secondly, with a global phase ψ chosen as a solution of the eikonal equation (cf. [\[1, Eq. \(1.10\)\]](#)),

$$\begin{aligned} |\nabla\psi|^2 &= k_a^2 - \mathcal{V}(r), \\ \text{satisfying } \psi(r, k_a) &= r k_a (1 + o(1)), \quad \text{as } r \rightarrow \infty, \end{aligned} \quad (3.76)$$

there exists a unique solution φ_ℓ^+ to

$$\begin{aligned} (-\partial_r^2 + V_\ell) \varphi_\ell^+ &= 0, \quad r \in (0, \infty), \\ \text{satisfying } \varphi_\ell^+(r) &= e^{i\psi(r, k_a)} (1 + o(1)), \quad \text{as } r \rightarrow \infty. \end{aligned} \quad (3.77)$$

A choice of the phase function $\psi(r, k_a)$ can be, for $r_0 > 0$,

$$\psi(r, k_a) = \int_{r_0}^r \sqrt{k_a^2 - \mathcal{V}(s)} ds = \int_{r_0}^r \sqrt{k^2(s) - \frac{\phi_0''(s)}{c_0^2(s)} + \frac{\eta(s)}{s+1}} ds. \quad (3.78)$$

Under assumption [\(3.74\)](#), and for model **S-AtmoI**, the real part of the quantity in the square root is sign definite (> 0 for $\omega > \omega_c$, and < 0 for $\omega < \omega_c$, both with $r_0 = r_a$). The constructed φ_ℓ is called a *regular solution* at $r = 0$ and φ_ℓ^+ a solution *outgoing-at-infinity*.

3. The third result is the existence and uniqueness of the outgoing Green's function \mathcal{G}_ℓ^+ , defined by

$$\mathcal{G}_\ell^+(r, s) := -\frac{\mathbb{H}(s-r) \varphi_\ell(r) \varphi_\ell^+(s) + \mathbb{H}(r-s) \varphi_\ell(s) \varphi_\ell^+(r)}{\mathbb{W}_\ell^+}, \quad r, s > 0, \quad (3.79)$$

which gives the unique solution to the conjugated equation, for $s > 0$,

$$\begin{aligned} & \left(-\partial_r^2 + V_\ell \right) \mathcal{G}_\ell(r, s) = \delta(r - s), \quad \text{on } (0, \infty), \\ & \text{satisfying } \mathcal{G}_\ell^+(r) = e^{i\psi(r, k_a)} (1 + o(1)), \quad \text{as } r \rightarrow \infty, \\ & \text{and } \mathcal{G}_\ell^+(r) = r^{\kappa_\ell^+} (1 + o(1)), \quad \text{as } r \rightarrow 0. \end{aligned} \tag{3.80}$$

In (3.79), H is the Heaviside function and W_ℓ^+ denotes the Wronskian W of $\varphi_\ell(s)$ and $\varphi_\ell^+(s)$,

$$W_\ell^+ := W\{\varphi_\ell, \varphi_\ell^+\} = \varphi_\ell(s) \varphi_\ell^{+\prime}(s) - \varphi_\ell'(s) \varphi_\ell^+(s). \tag{3.81}$$

Since the second order operator \mathcal{L}_ℓ lacks first order derivative and is thus symmetric, $s \mapsto W_\ell^+(s)$ is a constant function

$$\partial_s W_\ell^+ = 0. \tag{3.82}$$

This also results in the symmetry of \mathcal{G}_ℓ^+ ,

$$\mathcal{G}_\ell^+(r, s) = \mathcal{G}_\ell^+(s, r), \quad 0 < r, s. \tag{3.83}$$

Results for the original modal ODE \mathfrak{L}_ℓ The outgoing kernel G_ℓ^+ is uniquely determined by its relation to \mathcal{G}_ℓ^+ via (3.18) or equivalently⁷

$$\boxed{G_\ell^+(r, s) = \mathcal{G}_\ell^+(r, s) K_\ell(r, s) c_0^2(s) \rho_0(s) s^2}, \tag{3.84}$$

where the function $K_\ell(r, s)$ is defined with $\sqrt{\cdot}$ given in (2.14a) as

$$K_\ell(r, s) := \frac{1}{r c_0(r) \rho_0^{1/2}(r) s c_0(s) \rho_0^{1/2}(s)} \frac{\sqrt{F_\ell(s)} \sqrt{F_\ell(r)}}{\sqrt{F_0(s)} \sqrt{F_0(r)}}. \tag{3.85}$$

Remark 10. The form (3.84) is useful since it separates out the factors, K_ℓ and \mathcal{G}_ℓ^+ , that are symmetric in r and s . The symmetry of K_ℓ follows from its definition and that of \mathcal{G}_ℓ^+ from the form (3.79). \diamond

It can be more practical, e.g. for numerical computation, to work directly with the original modal operator \mathfrak{L}_ℓ and obtain G_ℓ^+ . The characterization of outgoing solutions for \mathfrak{L}_ℓ are still inherited from that for \mathcal{L}_ℓ through the relation (3.13). Similarly to \mathcal{G}_ℓ^+ , we have two ways to directly retrieve the outgoing kernel G_ℓ^+ (3.84).

1. In the first characterization, with factor K_ℓ coming from relation (3.84) and exponent λ_ℓ^+ given in (3.59), the kernel G_ℓ^+ is the unique solution to

$$\begin{aligned} & \left(-\partial_r^2 + V_\ell \right) G_\ell^+ = \delta(r - s), \quad r \in (0, \infty), \quad \text{satisfying} \\ & \frac{G_\ell^+(r, s)}{K_\ell(r, s) c_0^2(s) \rho_0(s) s^2} = e^{i\psi(r, k_a)} (1 + o(1)), \quad \text{as } r \rightarrow \infty, \\ & \text{and } G_\ell^+(r) = r^{\lambda_\ell^+} (1 + o(1)), \quad \text{as } r \rightarrow 0. \end{aligned} \tag{3.86}$$

2. In the second characterization, one uses the homogeneous solutions of \mathfrak{L}_ℓ to define G_ℓ^+ . With λ_ℓ^+ given in (3.59), there exists a unique solution denoted by ϕ_ℓ to

$$\begin{aligned} & (\hat{q}_\ell \partial_r^2 + q_\ell \partial_r + \tilde{q}_\ell) \phi_\ell = 0, \quad r \in (0, \infty), \\ & \text{satisfying } \phi_\ell(r) = r^{\lambda_\ell^+} (1 + o(1)), \quad \text{as } r \rightarrow 0, \end{aligned} \tag{3.87}$$

⁷This is seen by algebraic arrangement,

$$\frac{\mathfrak{I}_\ell(r) F_\ell(s)}{\mathfrak{I}_\ell(s) F_0(s)} = \frac{s c_0(s) \sqrt{\rho_0(s)} \sqrt{F_\ell(r)} \sqrt{F_0(s)} F_\ell(s)}{r c_0(r) \sqrt{\rho_0(r)} \sqrt{F_0(r)} \sqrt{F_\ell(s)} F_0(s)} = \frac{s c_0(s) \rho_0^{1/2}(s) \sqrt{F_\ell(s)} \sqrt{F_\ell(r)}}{r c_0(r) \rho_0^{1/2}(r) \sqrt{F_0(s)} \sqrt{F_0(r)}} = K_\ell(r, s) s^2 c_0^2(s) \rho_0(s).$$

and, with a choice of global phase in (3.76) and \mathfrak{J}_ℓ defined in (2.18), a unique solution denoted by φ_ℓ^+ to

$$\begin{aligned} (\hat{q}_\ell \partial_r^2 + q_\ell \partial_r + \tilde{q}_\ell) \phi_\ell^+ &= 0, \quad r \in (0, \infty), \\ \text{satisfying } \mathfrak{J}_\ell(r) \phi_\ell^+(r) &= e^{i\psi(r, k_a)} (1 + o(1)), \quad \text{as } r \rightarrow \infty. \end{aligned} \quad (3.88)$$

The existence and uniqueness of φ_ℓ and φ_ℓ^+ is obtain from that of ϕ_ℓ and ϕ_ℓ^+ via (3.13),

$$\varphi_\ell = \mathfrak{J}_\ell \phi_\ell, \quad \varphi_\ell^+ = \mathfrak{J}_\ell \phi_\ell^+, \quad \text{with } \mathfrak{J}_\ell \text{ defined in (2.18)}. \quad (3.89)$$

The kernel G_ℓ^+ defined in (3.84) (from \mathcal{G}_ℓ^+) is also given by ϕ_ℓ and ϕ_ℓ^+ as

$$G_\ell^+(r, s) = \frac{\mathbf{H}(s-r) \phi_\ell(r) \phi_\ell^+(s) + \mathbf{H}(r-s) \phi_\ell(s) \phi_\ell^+(r)}{\hat{q}_\ell(s) \mathcal{W}_\ell^+(s)}. \quad (3.90)$$

As in (3.79), \mathbf{H} is the Heavideside function and \mathcal{W} is the Wronskian, which for \mathfrak{L}_ℓ is dependent⁸ on s ,

$$\mathcal{W}_\ell^+(s) := \mathcal{W}\{\phi_\ell(s), \phi_\ell^+(s)\} = \phi_\ell(s) \phi_\ell^{\prime+}(s) - \phi_\ell^{\prime+}(s) \phi_\ell(s). \quad (3.91)$$

Remark on the choice of representative in the regular and outgoing family The sets of ‘regular-at-zero’ and outgoing solutions for \mathcal{L}_ℓ and \mathfrak{L}_ℓ are each one-dimensional. Specifically, with φ_ℓ and φ_ℓ^+ defined in (3.75) and (3.77), we have, for any ‘regular-at-zero’ and outgoing solution for \mathcal{L}_ℓ , for some constants $c, d \neq 0$,

$$\varphi_{\text{generic}}^+(r) = \tilde{c} \varphi_\ell^+(r), \quad \varphi_{\text{generic}}(r) = d \varphi_\ell(r). \quad (3.92)$$

A basis of solutions for \mathfrak{L}_ℓ is given by, for some constants $c, d, \tilde{c}, \tilde{d} \neq 0$,

$$\phi_{\text{generic}}^+(r) = c \mathfrak{J}_\ell(r) \varphi_\ell^+(r), \quad \phi_{\text{generic}}(r) = d \mathfrak{J}_\ell(r) \varphi_\ell(r). \quad (3.93)$$

Any choice in the ‘regular-at-zero’ and outgoing family gives the same Green’s kernel G_ℓ^+ and \mathcal{G}_ℓ^+ . We will now write out the explication for G_ℓ^+ .

With the generic solutions given in (3.93), the right-hand-side of (3.90) is written as,

$$\text{rhs of (3.90)} = \frac{\mathbf{H}(s-r) \phi_{\text{generic}}(r) \phi_{\text{generic}}^+(s) + \mathbf{H}(r-s) \phi_{\text{generic}}(s) \phi_{\text{generic}}^+(r)}{\hat{q}_\ell(s) \mathcal{W}\{\phi_{\text{generic}}(s), \phi_{\text{generic}}^+(s)\}}. \quad (3.94)$$

Next we use the following identity with the Wronskian,

$$\begin{vmatrix} \mathfrak{J}_\ell \varphi_\ell & \mathfrak{J}_\ell \tilde{\varphi}_\ell \\ (\mathfrak{J}_\ell \varphi_\ell)' & (\mathfrak{J}_\ell \tilde{\varphi}_\ell)' \end{vmatrix} = \begin{vmatrix} \mathfrak{J}_\ell \varphi_\ell & \mathfrak{J}_\ell \tilde{\varphi}_\ell \\ \mathfrak{J}_\ell' \varphi_\ell & \mathfrak{J}_\ell' \tilde{\varphi}_\ell \end{vmatrix} + \begin{vmatrix} \mathfrak{J}_\ell \varphi_\ell & \mathfrak{J}_\ell \tilde{\varphi}_\ell \\ \mathfrak{J}_\ell \varphi_\ell' & \mathfrak{J}_\ell \tilde{\varphi}_\ell' \end{vmatrix} = \mathfrak{J}_\ell^2 \mathcal{W}\{\varphi_\ell, \tilde{\varphi}_\ell\}, \quad (3.95)$$

and substitute the form (3.93) of ϕ_{generic} and ϕ_{generic}^+ in the right-hand side of (3.94). After simplification of constant c and d from numerator and denominator, we obtain

$$\begin{aligned} \text{rhs of (3.90)} &= \mathfrak{J}_\ell(r) \mathfrak{J}_\ell(s) \frac{\mathbf{H}(r-s) \varphi_\ell(r) \varphi_\ell^+(s) + \mathbf{H}(r-s) \varphi_\ell(s) \varphi_\ell^+(r)}{\hat{q}_\ell(s) \mathcal{W}\{\mathfrak{J}_\ell \varphi_\ell(s), \mathfrak{J}_\ell \varphi_\ell^+(s)\}} \\ &= -\frac{\mathfrak{J}_\ell(r) \mathfrak{J}_\ell(s)}{\hat{q}_\ell(s) \mathfrak{J}_\ell(s)^2} \mathcal{G}_\ell^+(r, s). \end{aligned} \quad (3.96)$$

As a result of this, (3.90) gives the same definition of Green’s kernel as (3.18). We list here the variants of G_ℓ^+

$$G_\ell^+(r, s) = -\mathcal{G}_\ell^+(r, s) \frac{\mathbf{F}_\ell(s)}{\mathbf{F}_0(s) \mathcal{W}_\ell^+(s)} = \mathcal{G}_\ell^+(r, s) K_\ell(r, s) c_0^2(s) \rho_0(s) s^2, \quad (3.97)$$

where K_ℓ is given in (3.85) and we introduce the quantity \mathbf{G}_ℓ^+ (further studied in Section 4),

$$\mathbf{G}_\ell^+(r, s) := \mathbf{H}(s-r) \phi_\ell(r) \phi_\ell^+(s) + \mathbf{H}(r-s) \phi_\ell(s) \phi_\ell^+(r). \quad (3.98)$$

Remark 11. The simplification of constant c and d from the ratio in (3.96) also means that in theory one can work with any choice of ‘regular-at-zero’ and outgoing family and obtain the same Green’s kernel G_ℓ^+ . However, due to the singularity at $r_{\omega, \ell}^*$ in \mathfrak{J}_ℓ , in actual numerical computation, certain choices are numerically more stable than others. See further discussion in Remark 16. \diamond

⁸On the other hand, in Lemma 1, it will be shown that the factor $s \mapsto \mathfrak{p} = \frac{\mathbf{F}_\ell}{\mathbf{F}_0} \frac{1}{\mathcal{W}_\ell^+} \frac{1}{c_0^2 \rho_0 s^2}$ is independent of s . Here we have substituted in the definition of $\frac{1}{\hat{q}_\ell} = -\frac{\mathbf{F}_\ell}{\mathbf{F}_0}$ given in (3.29).

Remark on the behavior of solutions in the neighborhood of $r_{\omega,\ell}^*$ From the value of the indicial exponents associated to $r_{\omega,\ell}^*$ given by, (3.56), at $\Gamma = 0$, in a neighborhood of $r_{\omega,\ell}^*$, both φ_ℓ and φ_ℓ^+ , and thus \mathcal{G}_ℓ^+ have the property:

$$(a + c \ln |r - r_{\omega,\ell}^*|) |r - r_{\omega,\ell}^*|^{3/2} h(r) + b |r - r_{\omega,\ell}^*|^{-1/2} \tilde{h}(r), \tag{3.99}$$

for some continuous functions h and \tilde{h} near $r_{\omega,\ell}^*$, and constant a, b, c . The presence of the logarithmic function \ln is due to $\kappa_\star^+ - \kappa_\star^- \in \mathbb{Z}$. Note that since a choice has already been made for φ_ℓ at $r = 0$, and for φ_ℓ^+ at $r \rightarrow \infty$, determining each one completely, these two solutions and kernel \mathcal{G}_ℓ^+ might contain both factor $|r - r_{\omega,\ell}^*|^{3/2}$ and $|r - r_{\omega,\ell}^*|^{-1/2}$. This means that they can be singular near $r_{\omega,\ell}^*$ when $\Gamma = 0$.

On the other hand, the indicial exponents for \mathfrak{L}_ℓ associated to $r_{\omega,\ell}^*$ are both positive, this means that in a neighborhood of $r_{\omega,\ell}^*$, any solution of $\mathfrak{L}_\ell w = 0$, and thus ϕ_ℓ, ϕ_ℓ^+ and thus G_ℓ^+ satisfy

$$(\tilde{a} + \tilde{c} \ln |r - r_{\omega,\ell}^*|) |r - r_{\omega,\ell}^*|^2 g(r) + \tilde{b} \tilde{g}(r), \tag{3.100}$$

for some constant $\tilde{a}, \tilde{b}, \tilde{c}$ and some continuous functions g and \tilde{g} near $r_{\omega,\ell}^*$. This means that, even when $\Gamma = 0$, they are continuous at $r_{\omega,\ell}^*$, (unlike $\varphi_\ell^+, \varphi_\ell$, and \mathcal{G}_ℓ^+). Together with the continuity when $\Gamma > 0$, we have that for all $\Gamma \geq 0$,

$$\phi_\ell^+, \phi_\ell \in \mathcal{C}(\mathbb{R}^+), \quad G_\ell^+(r, s) \in \mathcal{C}(\mathbb{R}_r^+ \times \mathbb{R}_s^+). \tag{3.101}$$

4 Theoretical results - Part 2: Coefficients of the formal expansion of the 3D Green's kernel in VSH basis

In this section, we first rewrite the above results in Proposition 1 to make appear the coefficients of the 3D kernel in VSH basis. These quantities are

$$G_\ell^{\text{PP}}, \quad G_\ell^{\text{PB}}, \quad G_\ell^{\text{BP}}, \quad G_\ell^{\text{BB}}. \tag{4.1}$$

How they are related to the 3D kernel \mathbb{G}^+ is formally discussed at the end of the section. Since the system of the ODE (3.12) of the coefficients of the unknown ξ can be reduced to a single ODE ((3.14), or equivalently (3.12a)) in terms of a_ℓ^m the coefficients in the radial direction, it follows that the components of \mathbb{G}^+ will be determined in terms of that in the radial direction (G_ℓ^{PP}) and its derivatives. This is the purpose of Proposition 1. In our second result, given by Proposition 2, we go further and obtain a ‘gluing’ formula for these components, in which they will be expressed directly in terms of the homogeneous (i.e. without source) solutions ϕ_ℓ^+ and ϕ_ℓ of \mathfrak{L}_ℓ . This result is the key ingredient for the computation algorithm in Section 5.

In the following proposition, we denote by $\mathcal{D}_+ := \mathcal{C}_c^\infty([0, \infty))$ the space of smooth functions having compact support on $[0, \infty)$, and \mathcal{D}'_+ its dual.

Proposition 1. For \mathbf{a}_ℓ^m and \mathbf{b}_ℓ^m defined in (3.17), we have

$$\mathbf{a}_\ell^m = R_\odot^2 \int_0^\infty G_\ell^{\text{PP}}(r, s) f_\ell^m(s) s^2 ds + R_\odot^2 \int_0^\infty G_\ell^{\text{PB}}(r, s) g_\ell^m(s) s^2 ds, \tag{4.2a}$$

$$\mathbf{b}_\ell^m = R_\odot^2 \int_0^\infty G_\ell^{\text{BP}}(r, s) f_\ell^m(s) s^2 ds + R_\odot^2 \langle G_\ell^{\text{BB}}(r, s), g_\ell^m(s) s^2 \rangle_{\mathcal{D}'_+, \mathcal{D}_+}, \tag{4.2b}$$

where

$$G_\ell^{\text{PP}}(r, s) = \frac{G_\ell^+(r, s)}{c_0^2(s)\rho_0(s)s^2}; \quad (4.3a)$$

$$G_\ell^{\text{PB}}(r, s) = -\frac{\sqrt{\ell(\ell+1)}}{F_\ell(s)} \left[s\partial_s G_\ell^{\text{PP}} + G_\ell^{\text{PP}} \left(2 - s\frac{\alpha_{p_0}(s)}{\gamma(s)} \right) \right]; \quad (4.3b)$$

$$G_\ell^{\text{BP}}(r, s) = -\frac{\sqrt{\ell(\ell+1)}}{F_\ell(r)} \left[r\partial_r G_\ell^{\text{PP}}(r, s) + G_\ell^{\text{PP}}(r, s) \left(2 - r\frac{\alpha_{p_0}(r)}{\gamma(r)} \right) \right]; \quad (4.3c)$$

and

$$G_\ell^{\text{BB}}(r, s) = -\frac{\sqrt{\ell(\ell+1)}}{F_\ell(r)} \left[r\partial_r G_\ell^{\text{PB}}(r, s) + G_\ell^{\text{PB}}(r, s) \left(2 - r\frac{\alpha_{p_0}(r)}{\gamma(r)} \right) \right] - \frac{r^2}{F_\ell(r)\gamma(r)p_0(r)} \frac{\delta(r-s)}{s^2} \quad (4.4a)$$

$$\begin{aligned} &= \frac{\ell(\ell+1)}{F_\ell(r)F_\ell(s)} \left[r\partial_r s\partial_s G_\ell^{\text{PP}} + \left(2 - s\frac{\alpha_{p_0}(s)}{\gamma(s)} \right) r\partial_r G_\ell^{\text{PP}} \right. \\ &\quad \left. + \left(2 - r\frac{\alpha_{p_0}(r)}{\gamma(r)} \right) s\partial_s G_\ell^{\text{PP}} + G_\ell^{\text{PP}} \left(2 - r\frac{\alpha_{p_0}(r)}{\gamma(r)} \right) \left(2 - s\frac{\alpha_{p_0}(s)}{\gamma(s)} \right) \right] \\ &\quad - \frac{r^2}{F_\ell(r)\gamma(r)p_0(r)} \frac{\delta(r-s)}{s^2}. \end{aligned} \quad (4.4b)$$

Proof. Part 1 : kernel for the radial coefficients We focus on (3.17),

$$a_\ell^m = \int_0^\infty G_\ell^+(r, s) f_\ell^m(s) ds \quad (4.5)$$

With f_ℓ^m comprised of three terms, we will compute each of them separately.

$$a_\ell^m = I_1 + I_2 + I_3 \quad (4.6)$$

with

$$\begin{aligned} I_1 &:= \int_0^\infty G_\ell^+(r, s) \frac{f_\ell^m(s)}{\gamma(s)p_0(s)} ds \\ I_2 &:= \int_0^\infty G_\ell^+(r, s) \frac{s\frac{\alpha_{p_0}(s)}{\gamma(s)} - s\alpha_{\gamma p_0}(s) - 1}{F_\ell(s)} \frac{\sqrt{\ell(\ell+1)} g_\ell^m(s)}{\gamma(s)p_0(s)} ds \\ I_3 &:= \int_0^\infty G_\ell^+(r, s) \frac{\sqrt{\ell(\ell+1)}}{r} \partial_s \left(\frac{s^2 g_\ell^m(s)}{F_\ell(s)\gamma(s)p_0(s)} \right) ds. \end{aligned} \quad (4.7)$$

• We first consider I_1 . We deduce from the above equality that

$$G_\ell^{\text{PP}}(r, s) = \frac{G_\ell^+(r, s)}{c_0^2(s)\rho_0(s)s^2}. \quad (4.8)$$

• We next consider I_2 ,

$$I_2 = \int_0^\infty \frac{s\frac{\alpha_{p_0}(s)}{\gamma(s)} - s\alpha_{\gamma p_0}(s) - 1}{F_\ell(s)} G_\ell^{\text{PP}} g_\ell^m(s) \sqrt{\ell(\ell+1)} s^2 ds \quad (4.9)$$

• We next consider I_3 . We are working with g_ℓ^m of compact support, in addition with $G_\ell^+(0) = 0$, we can carry out integration by parts in the above integral. This gives

$$\begin{aligned} I_3 &= - \int_0^\infty (s\partial_s G_\ell^{\text{PP}}) \frac{g_\ell^m(s)\sqrt{\ell(\ell+1)}}{F_\ell(s)} s^2 ds \\ &\quad + \int_0^\infty G_\ell^{\text{PP}} \alpha_{\gamma p_0}(s) \frac{s g_\ell^m(s)}{F_\ell(s)} \sqrt{\ell(\ell+1)} s^2 ds \\ &\quad - \int_0^\infty G_\ell^{\text{PP}} \frac{g_\ell^m(s)}{F_\ell(s)} \sqrt{\ell(\ell+1)} s^2 ds. \end{aligned} \quad (4.10)$$

Put together with (4.9), we obtain

$$\begin{aligned} G_\ell^{\text{PB}}(r, s) &= \sqrt{\ell(\ell+1)} \frac{s^{\frac{\alpha_{p_0}(s)}{\gamma(s)} - 2}}{F_\ell(s)} G_\ell^{\text{PP}} - \sqrt{\ell(\ell+1)} (s \partial_s G_\ell^{\text{PP}}) \frac{1}{F_\ell(s)} \\ &= -\frac{\sqrt{\ell(\ell+1)}}{F_\ell(s)} \left[s \partial_s G_\ell^{\text{PP}} + G_\ell^{\text{PP}} \left(2 - s^{\frac{\alpha_{p_0}(s)}{\gamma(s)}} \right) \right] \end{aligned} \quad (4.11)$$

Part 2a : kernel for the horizontal coefficients Consider \mathbf{b}_ℓ^m , we have

$$\frac{\mathbf{b}_\ell^m}{\sqrt{\ell(\ell+1)}} = -\frac{r}{F_\ell(r)} \partial_r a_\ell^m - \frac{2 - r^{\frac{\alpha_{p_0}(r)}{\gamma(r)}}}{F_\ell(r)} a_\ell^m - \frac{r^2}{F_\ell} \frac{R_\odot^2}{\gamma p_0} \frac{g_\ell^m}{\sqrt{\ell(\ell+1)}}. \quad (4.12)$$

Since

$$\partial_r a_\ell^m = R_\odot^2 \int_0^\infty (\partial_r G_\ell^{\text{PP}}(r, s)) f_\ell^m(s) s^2 ds + R_\odot^2 \int_0^\infty (\partial_r G_\ell^{\text{PB}}(r, s)) g_\ell^m(s) s^2 ds, \quad (4.13)$$

$$\begin{aligned} \frac{\mathbf{b}_\ell^m}{R_\odot^2} &= -\frac{r\sqrt{\ell(\ell+1)}}{F_\ell(r)} \left(\int_0^\infty (\partial_r G_\ell^{\text{PP}}(r, s)) f_\ell^m(s) s^2 ds + \int_0^\infty (\partial_r G_\ell^{\text{PB}}(r, s)) g_\ell^m(s) s^2 ds \right) \\ &\quad - \sqrt{\ell(\ell+1)} \frac{2 - r^{\frac{\alpha_{p_0}(r)}{\gamma(r)}}}{F_\ell(r)} \left(\int_0^\infty G_\ell^{\text{PP}}(r, s) f_\ell^m(s) s^2 ds + \int_0^\infty G_\ell^{\text{PB}}(r, s) g_\ell^m(s) s^2 ds \right) \\ &\quad - \frac{r^2}{F_\ell(r) \gamma(r) p_0(r)} \langle \delta(r-s), g_\ell^m(s) \rangle. \end{aligned} \quad (4.14)$$

Thus, we obtain

$$\begin{aligned} G_\ell^{\text{BP}} &= -\frac{\sqrt{\ell(\ell+1)}}{F_\ell(r)} \left[r \partial_r G_\ell^{\text{PP}}(r, s) + G_\ell^{\text{PP}}(r, s) \left(2 - r^{\frac{\alpha_{p_0}(r)}{\gamma(r)}} \right) \right] \\ G_\ell^{\text{BB}} &= -\frac{\sqrt{\ell(\ell+1)}}{F_\ell(r)} \left[r \partial_r G_\ell^{\text{PB}}(r, s) + G_\ell^{\text{PB}}(r, s) \left(2 - r^{\frac{\alpha_{p_0}(r)}{\gamma(r)}} \right) \right] + \frac{r^2}{F_\ell(r) \gamma(r) p_0(r)} \frac{\delta(r-s)}{s^2} \end{aligned} \quad (4.15)$$

Part 2b : Expression of G_ℓ^{BB} in terms of G_ℓ^{PP} We have,

$$\begin{aligned} -r \partial_r G_\ell^{\text{PB}} &= r \partial_r \left(\frac{\sqrt{\ell(\ell+1)}}{F_\ell(s)} \left[s \partial_s G_\ell^{\text{PP}} + G_\ell^{\text{PP}} \left(2 - s^{\frac{\alpha_{p_0}(s)}{\gamma(s)}} \right) \right] \right) \\ &= \frac{\sqrt{\ell(\ell+1)}}{F_\ell(s)} \left[r \partial_r s \partial_s G_\ell^{\text{PP}} + \left(2 - s^{\frac{\alpha_{p_0}(s)}{\gamma(s)}} \right) r \partial_r G_\ell^{\text{PP}} \right], \end{aligned} \quad (4.16)$$

$$\begin{aligned} -r \partial_r G_\ell^{\text{PB}} - G_\ell^{\text{PB}} \left(2 - r^{\frac{\alpha_{p_0}(r)}{\gamma(r)}} \right) &= \frac{\sqrt{\ell(\ell+1)}}{F_\ell(s)} \left[r \partial_r s \partial_s G_\ell^{\text{PP}} + \left(2 - s^{\frac{\alpha_{p_0}(s)}{\gamma(s)}} \right) r \partial_r G_\ell^{\text{PP}} \right. \\ &\quad \left. + \left(2 - r^{\frac{\alpha_{p_0}(r)}{\gamma(r)}} \right) s \partial_s G_\ell^{\text{PP}} + G_\ell^{\text{PP}} \left(2 - r^{\frac{\alpha_{p_0}(r)}{\gamma(r)}} \right) \left(2 - s^{\frac{\alpha_{p_0}(s)}{\gamma(s)}} \right) \right]. \end{aligned} \quad (4.17)$$

□

Derivatives of G_ℓ^{PP} We next compute the derivatives of G_ℓ^{PP} in terms of the homogeneous solutions ϕ_ℓ and ϕ_ℓ^+ defined in (3.87) and (3.88). For this purpose, we define the following quantities,

$$G_\ell^+(r, s) := \mathbf{H}(s-r) \phi_\ell(r) \phi_\ell^+(s) + \mathbf{H}(r-s) \phi_\ell(s) \phi_\ell^+(r); \quad (4.18a)$$

$$T_\ell^+(r, s) := \mathbf{H}(s-r) r \phi_\ell'(r) \phi_\ell^+(s) + \mathbf{H}(r-s) \phi_\ell(s) r \partial_r \phi_\ell^+(r); \quad (4.18b)$$

$$Q_\ell^+(r, s) := \mathbf{H}(s-r) r \phi_\ell'(r) s \partial_s \phi_\ell^+(s) + \mathbf{H}(r-s) s \phi_\ell'(s) r \partial_r \phi_\ell^+(r). \quad (4.18c)$$

For compact notation in the following derivation, we introduce

$$\mathfrak{F}(r) := c_0^2(r)\rho_0(r)F_0(r), \quad \mathbf{p}(s) := \frac{F_\ell(s)}{\mathcal{W}_\ell^+(s)\mathfrak{F}(s)} = \frac{F_\ell(s)}{\mathcal{W}_\ell^+(s)F_0(s)} \frac{1}{c_0^2(s)\rho_0(s)}. \quad (4.19)$$

We also denote the Wronskian associated to $\{\phi_\ell, \phi_\ell^+\}$ as

$$\mathcal{W}_\ell^+(s) := \phi_\ell(s)\partial_s\phi_\ell^+(s) - \phi_\ell^+(s)\partial_s\phi_\ell(s). \quad (4.20)$$

From the expression (4.3a) of G_ℓ^{PP} in Proposition 1 and (3.90) for G_ℓ^+ , we can write G_ℓ^{PP} as,

$$G_\ell^{\text{PP}}(r, s) = -G_\ell^+(r, s) \frac{\mathbf{p}(s)}{s^2}. \quad (4.21)$$

It remains to compute the derivatives of G_ℓ^{PP} . We start with some properties of the quantities in (4.18).

Lemma 1. – With ϕ_ℓ and ϕ_ℓ^+ both regular on $r > 0$, the functions $G_\ell^+(r, s)$, $\mathbb{T}_\ell^+(r, s)$ and $\mathbb{Q}_\ell^+(r, s)$ are regular for $r, s > 0$.

– Quantities G_ℓ^+ and \mathbb{Q}_ℓ^+ are symmetric in (r, s) :

$$\mathbb{Q}_\ell^+(r, s) = \mathbb{Q}_\ell^+(s, r), \quad G_\ell^+(r, s) = G_\ell^+(s, r). \quad (4.22)$$

On other hand, \mathbb{T}_ℓ^+ is not with

$$\mathbb{T}_\ell^+(s, r) = \mathbb{H}(s-r)\phi_\ell(r)s\partial_s\phi_\ell^+(s) + \mathbb{H}(r-s)s\phi_\ell'(s)\phi_\ell^+(r). \quad (4.23)$$

– Due to the symmetry of G_ℓ^{PP} , the quantity $\frac{\mathbf{p}(s)}{s^2}$ is independent of s , i.e.

$$\partial_s \frac{\mathbf{p}(s)}{s^2} = 0. \quad (4.24)$$

In addition, \mathfrak{F} of (4.19) is regular on $r > 0$, and $\mathcal{W}_\ell^+(s)$ defined in (4.20) is regular on $r > 0$.

Proof. We compute the derivative of the factor \mathbf{p} . Using Abel's identity⁹

$$-\frac{\partial_s \mathcal{W}\{\phi_\ell, \phi_\ell^+\}(s)}{\mathcal{W}_\ell\{\phi_\ell, \phi_\ell^+\}(s)} = \frac{q_\ell(s)}{\hat{q}_\ell(s)} = -\mathfrak{h}_\ell. \quad (4.26)$$

On the other hand, since $F_\ell - F_0 = -\ell(\ell+1)$,

$$\partial_s \frac{1}{c_0^2\rho_0 s^2} = \frac{1}{c_0^2\rho_0 s^2} \left(\alpha_{c_0^2\rho_0} - \frac{2}{s} \right), \quad \partial_s \frac{F_\ell}{F_0} = \frac{F'_\ell}{F_0} - \frac{F_\ell F'_0}{F_0^2} = \frac{F_\ell \ell(\ell+1)F'_0}{F_0 F_\ell F_0}. \quad (4.27)$$

This gives

$$\partial_s \frac{\mathbf{p}}{s^2} = \frac{\mathbf{p}}{s^2} \left(-\mathfrak{h}_\ell + \alpha_{c_0^2\rho_0} - \frac{2}{s} + \frac{\ell(\ell+1)F'_0}{F_\ell F_0} \right). \quad (4.28)$$

Result (4.24) is obtained by substituting in the definition of \mathfrak{h}_ℓ ,

$$-\mathfrak{h}_\ell = -\alpha_{\gamma\rho_0} + \frac{2}{r} - \ell(\ell+1) \frac{F'_0}{F_0 F_\ell}. \quad (4.29)$$

Regarding the constancy in (4.24), see also Remark 12 for a second approach. □

⁹Abel's identity: From its definition $\mathcal{W}_\ell\{\phi_\ell, \phi_\ell^+\}(s) = \phi_\ell(s)\phi_\ell^+(s) - \phi_\ell'(s)\phi_\ell^+(s)$, we have

$$\begin{aligned} \partial_s \mathcal{W}\{\phi_\ell, \phi_\ell^+\}(s) &= \phi_\ell'(s)\phi_\ell^+(s) + \phi_\ell(s)\partial_s^2\phi_\ell^+(s) - \phi_\ell''(s)\phi_\ell^+(s) - \phi_\ell'(s)\phi_\ell^+(s) \\ &= -\frac{\phi_\ell(s)}{\hat{q}_\ell} (q_\ell\phi_\ell^+(s) + \tilde{q}_\ell\phi_\ell^+(s)) + \frac{\phi_\ell^+(s)}{\hat{q}_\ell} (q_\ell\phi_\ell'(s) + \tilde{q}_\ell\phi_\ell(s)) = -\frac{q_\ell(s)}{\hat{q}_\ell(s)} \mathcal{W}\{\phi_\ell, \phi_\ell^+\}(s). \end{aligned} \quad (4.25)$$

Remark 12. There is another way to show the constancy of quantity $\frac{\mathbf{p}(s)}{s^2}$ in terms of s . It is useful to note that

$$\frac{\mathbf{p}(s)}{s^2} = \frac{1}{\mathcal{W}_\ell^+(s)}, \quad (4.30)$$

where \mathcal{W}_ℓ^+ is the Wronskian of the regular-at-zero and outgoing solutions associated with conjugate operator \mathcal{L}_ℓ , defined in (3.81):

$$\mathcal{W}_\ell^+(s) := \mathcal{W}\{\varphi_\ell(s), \varphi_\ell^+(s)\}.$$

To see this, we first recall the relation between the Wronskian \mathcal{W}_ℓ^+ and \mathcal{W}_ℓ^+ given by (3.95),

$$\mathcal{W}_\ell^+(s) = \mathfrak{J}_\ell^2(s) \mathcal{W}_\ell^+(s). \quad (4.31)$$

Also recall from (2.18), the definition of \mathfrak{J}_ℓ ,

$$\mathfrak{J}_\ell^2(s) = \frac{F_\ell(s)}{s^2 c_0(s)^2 \rho_0(s) F_0(s)}. \quad (4.32)$$

Substitute these quantities into the definition of $\frac{\mathbf{p}(s)}{s^2}$,

$$\begin{aligned} \frac{\mathbf{p}(s)}{s^2} &= \frac{1}{\mathcal{W}_\ell^+(s)} \frac{F_\ell(s)}{F_0(s) s^2 c_0^2(s) \rho_0(s)} = \frac{1}{\mathfrak{J}_\ell(s)^2 \mathcal{W}_\ell^+(s)} \frac{F_\ell(s)}{F_0(s) s^2 c_0^2(s) \rho_0(s)} \\ &= \frac{1}{\mathcal{W}_\ell^+(s)} \frac{s^2 c_0(s)^2 \rho_0(s) F_0(s)}{F_\ell(s)} \frac{F_\ell(s)}{F_0(s) s^2 c_0^2(s) \rho_0(s)}. \end{aligned} \quad (4.33)$$

After simplification, we obtain identity (4.30). Since $s \mapsto \mathcal{W}_\ell^+(s)$ is constant, cf. (3.82), so is $s \mapsto \frac{\mathbf{p}(s)}{s^2}$.
 \diamond

Corollary 1. The derivatives of G_ℓ^+ defined in (4.18a) are given in terms of T_ℓ^+ (4.18b) and Q_ℓ^+ (4.18c) as,

$$r\partial_r G_\ell^+(r, s) = T_\ell^+(r, s), \quad s\partial_s G_\ell^+(r, s) = T_\ell^+(s, r); \quad (4.34a)$$

$$s\partial_s r\partial_r G_\ell^+ = r\partial_r s\partial_s G_\ell^+ = Q_\ell^+(r, s) - r^2 \mathcal{W}_\ell^+(r) \delta(r - s). \quad (4.34b)$$

From its definition (4.21) and result (4.24), we obtain the derivatives of G_ℓ^{PP} ,

$$r\partial_r G_\ell^{\text{PP}}(r, s) = -\frac{\mathbf{p}(s)}{s^2} r\partial_r G_\ell^+(r, s) = -\frac{\mathbf{p}(s)}{s^2} T_\ell^+(r, s); \quad (4.35a)$$

$$s\partial_s G_\ell^{\text{PP}}(r, s) = -\frac{\mathbf{p}(s)}{s^2} s\partial_s G_\ell^+(r, s) = -\frac{\mathbf{p}(s)}{s^2} T_\ell^+(s, r); \quad (4.35b)$$

$$s\partial_s r\partial_r G_\ell^{\text{PP}}(r, s) = -\frac{\mathbf{p}(s)}{s^2} s\partial_s r\partial_r G_\ell^+(r, s) = \frac{\mathbf{p}(s)}{s^2} (-Q_\ell^+(r, s) + r^2 \mathcal{W}_\ell^+(r) \delta(r - s)). \quad (4.35c)$$

Proof. It remains to compute the derivatives of $G_\ell^+(r, s)$ and the factor $\frac{F_\ell(s)}{\mathcal{W}(s)F_0(s)}$. Using the identity with the distributional derivative of the Heaviside with a smooth function f ,

$$(f(x)H(x - x_0))' = f(x_0)\delta(x - x_0) + f'(x)H(x - x_0), \quad (4.36)$$

we obtain

$$\begin{aligned} r\partial_r G_\ell^+(r, s) &= H(s - r) r\phi_\ell'(r) \phi_\ell^+(s) + H(r - s) \phi_\ell(s) r\partial_r \phi_\ell^+(r) \\ &\quad - r\delta(s - r) \phi(s) \phi^+(s) + s\delta(r - s) \phi_\ell(s) \phi_\ell^+(s) \\ &= H(s - r) r\phi_\ell'(r) \phi_\ell^+(s) + H(r - s) \phi_\ell(s) r\partial_r \phi_\ell^+(r). \end{aligned} \quad (4.37)$$

We next compute the derivatives with respect to s in a similar manner and obtain,

$$\begin{aligned}
s\partial_s G_\ell^+(r, s) &= +\mathbf{H}(s-r)\phi_\ell(r)s\partial_s\phi_\ell^+(s) + \mathbf{H}(r-s)s\partial_s\phi_\ell(s)\phi_\ell^+(r); \\
s\partial_s r\partial_r G_\ell^+(r, s) &= \mathbf{H}(s-r)r\phi_\ell'(r)s\partial_s\phi_\ell^+(s) + \mathbf{H}(r-s)s\partial_s\phi_\ell(s)r\partial_r\phi_\ell^+(r) \\
&\quad + s^2\delta(s-r)\phi_\ell'(s)\phi_\ell^+(s) - s^2\delta(r-s)\phi_\ell(s)\partial_s\phi_\ell^+(s) \\
&= \mathbf{H}(s-r)r\phi_\ell'(r)s\partial_s\phi_\ell^+(s) + \mathbf{H}(r-s)s\partial_s\phi_\ell(s)r\partial_r\phi_\ell^+(r) \\
&\quad - s^2\delta(r-s)\mathcal{W}\{\phi_\ell, \phi_\ell^+\}(s).
\end{aligned} \tag{4.38}$$

□

Proposition 2. *In terms of the quantities G_ℓ^+ , \mathbf{T}_ℓ^+ and \mathbf{Q}_ℓ^+ (4.18a)–(4.18c), the components of the 3D Green's kernels are,*

$$G_\ell^{\text{PP}}(r, s) = -G_\ell^+(r, s) \frac{\mathbf{p}(s)}{s^2} = -G_\ell^+(r, s) \frac{F_\ell(s)}{\mathcal{W}_\ell^+(s) \mathfrak{F}(s) s^2}; \tag{4.39a}$$

$$G_\ell^{\text{BP}}(r, s) = \sqrt{\ell(\ell+1)} \left[\mathbf{T}_\ell^+(r, s) + G_\ell^+ \left(2 - r \frac{\alpha_{p_0}(r)}{\gamma(r)} \right) \right] \frac{1}{\mathcal{W}_\ell^+(r) \mathfrak{F}(r) r^2}; \tag{4.39b}$$

$$G_\ell^{\text{PB}}(r, s) = \sqrt{\ell(\ell+1)} \left[\mathbf{T}_\ell^+(s, r) + G_\ell^+(r, s) \left(2 - s \frac{\alpha_{p_0}(s)}{\gamma(s)} \right) \right] \frac{1}{\mathcal{W}_\ell^+(s) \mathfrak{F}(s) s^2}; \tag{4.39c}$$

and

$$G_\ell^{\text{BB}}(r, s) = G_\ell^{\text{BBreg}}(r, s) - \frac{r^2}{\mathfrak{F}_0(r) s^2} \delta(r-s), \tag{4.40}$$

where

$$\begin{aligned}
G_\ell^{\text{BBreg}}(r, s) &= -\frac{\ell(\ell+1)}{F_\ell(r)} \left[\mathbf{Q}_\ell^+(r, s) + \left(2 - s \frac{\alpha_{p_0}(s)}{\gamma(s)} \right) \mathbf{T}_\ell^+(s, r) + \left(2 - r \frac{\alpha_{p_0}(r)}{\gamma(r)} \right) \mathbf{T}_\ell^+(r, s) \right. \\
&\quad \left. + \left(2 - r \frac{\alpha_{p_0}(r)}{\gamma(r)} \right) \left(2 - s \frac{\alpha_{p_0}(s)}{\gamma(s)} \right) G_\ell^+(r, s) \right] \frac{1}{\mathcal{W}_\ell^+(s) \mathfrak{F}(s) s^2}.
\end{aligned} \tag{4.41}$$

We have the following symmetry of the kernels in r and s ,

$$\begin{aligned}
G_\ell^{\text{PP}}(r, s) &= G_\ell^{\text{PP}}(s, r), & G_\ell^{\text{PB}}(r, s) &= G_\ell^{\text{BP}}(s, r); \\
G_\ell^{\text{BBreg}}(r, s) &= G_\ell^{\text{BBreg}}(s, r).
\end{aligned} \tag{4.42}$$

Proof. • We start from the expression of G_ℓ^{BP} and G_ℓ^{PB} given in (4.3c) and (4.3b)

$$\begin{aligned}
G_\ell^{\text{BP}}(r, s) &= \frac{\sqrt{\ell(\ell+1)}}{F_\ell(r)} \left[\mathbf{T}_\ell^+(r, s) + G_\ell^+(r, s) \left(2 - r \frac{\alpha_{p_0}(r)}{\gamma(r)} \right) \right] \frac{\mathbf{p}(s)}{s^2} \\
&= \frac{\sqrt{\ell(\ell+1)}}{F_\ell(r)} \left[\mathbf{T}_\ell^+(r, s) + G_\ell^+(r, s) \left(2 - r \frac{\alpha_{p_0}(r)}{\gamma(r)} \right) \right] \frac{\mathbf{p}(r)}{r^2} \\
&= \sqrt{\ell(\ell+1)} \left[\mathbf{T}_\ell^+(r, s) + G_\ell^+(r, s) \left(2 - r \frac{\alpha_{p_0}(r)}{\gamma(r)} \right) \right] \frac{1}{\mathcal{W}_\ell^+(r) \mathfrak{F}(r) r^2}.
\end{aligned} \tag{4.43}$$

For the third equality, we have used the fact that $s \mapsto \frac{\mathbf{p}(s)}{s^2}$ is independent of s , thus we can interchange r and s , i.e.,

$$\frac{\mathbf{p}(s)}{s^2} = \frac{\mathbf{p}(r)}{r^2}. \tag{4.44}$$

The simplification in the last equality comes from the definition of \mathbf{p} ,

$$\frac{\mathbf{p}(s)}{s^2} = \frac{1}{s^2 \mathfrak{F}(s) \mathcal{W}_\ell^+(s)}. \tag{4.45}$$

For G_ℓ^{PB} , the derivation is more straightforward:

$$\begin{aligned} G_\ell^{\text{PB}}(r, s) &= \frac{\sqrt{\ell(\ell+1)}}{F_\ell(s)} \left[\mathbb{T}_\ell^+(s, r) + \mathbb{G}_\ell^+(r, s) \left(2 - s \frac{\alpha_{p_0}(s)}{\gamma(s)} \right) \right] \frac{\mathbf{p}(s)}{s^2} \\ &= \sqrt{\ell(\ell+1)} \left[\mathbb{T}_\ell^+(s, r) + \mathbb{G}_\ell^+(r, s) \left(2 - s \frac{\alpha_{p_0}(s)}{\gamma(s)} \right) \right] \frac{1}{\mathcal{W}_\ell^+(s) \mathfrak{F}(s) s^2}. \end{aligned} \quad (4.46)$$

• We next consider G_ℓ^{BB} , going back to the expression for G_ℓ^{BB} given in (4.4b) and decomposing this expression into three terms, we have

$$G_\ell^{\text{BB}} = I_1 + I_2 + I_3, \quad (4.47)$$

where

$$\begin{aligned} I_1 &= \frac{\ell(\ell+1)}{F_\ell(r) F_\ell(s)} r \partial_r s \partial_s G_\ell^{\text{PP}} - \frac{r^2}{F_\ell(r) \gamma(r) p_0(r)} \frac{\delta(r-s)}{s^2}; \\ I_2 &= \frac{\ell(\ell+1)}{F_\ell(r) F_\ell(s)} \left[\left(2 - s \frac{\alpha_{p_0}(s)}{\gamma(s)} \right) r \partial_r G_\ell^{\text{PP}} + \left(2 - r \frac{\alpha_{p_0}(r)}{\gamma(r)} \right) s \partial_s G_\ell^{\text{PP}} \right]; \\ I_3 &= \frac{\ell(\ell+1)}{F_\ell(r) F_\ell(s)} G_\ell^{\text{PP}} \left(2 - r \frac{\alpha_{p_0}(r)}{\gamma(r)} \right) \left(2 - s \frac{\alpha_{p_0}(s)}{\gamma(s)} \right). \end{aligned} \quad (4.48)$$

• Consider the first term,

$$\begin{aligned} I_1 &= \frac{\ell(\ell+1)}{F_\ell(r) F_\ell(s)} r \partial_r s \partial_s G_\ell^{\text{PP}} - \frac{r^2}{F_\ell(r) \gamma(r) p_0(r)} \frac{\delta(r-s)}{s^2} \\ &= -\frac{\ell(\ell+1)}{F_\ell(r) F_\ell(s)} \frac{\mathbf{p}(s)}{s^2} r \partial_r s \partial_s \mathbb{G}_\ell^+ - \frac{r^2}{F_\ell(r) \gamma(r) p_0(r)} \frac{\delta(r-s)}{s^2} \\ &= -\frac{\ell(\ell+1) \mathbf{p}(s)}{s^2 F_\ell(r) F_\ell(s)} \mathbb{Q}_\ell^+(r, s) + \ell(\ell+1) \frac{\mathbf{p}(s)}{s^2 F_\ell(r) F_\ell(s)} s^2 \delta(r-s) \mathcal{W}_\ell^+(s) \\ &\quad - \frac{r^2}{F_\ell(r) \gamma(r) p_0(r)} \frac{\delta(r-s)}{s^2} \\ &= -\frac{\ell(\ell+1) \mathbf{p}(s)}{s^2 F_\ell(r) F_\ell(s)} \mathbb{Q}_\ell^+(r, s) - \frac{\delta(r-s)}{\gamma(r) p_0(r) F_0(r)}. \end{aligned} \quad (4.49)$$

The last two terms involving $\delta(r-s)$ are simplified as follows, using $F_\ell = F_0 - \ell(\ell+1)$,

$$\begin{aligned} &\frac{\ell(\ell+1) \mathbf{p}(s)}{F_\ell(r) F_\ell(s)} s^2 \delta(r-s) \mathcal{W}_\ell^+(s) - \frac{r^2}{F_\ell(r) \gamma(r) p_0(r)} \frac{\delta(r-s)}{s^2} \\ &= \delta(r-s) \frac{\ell(\ell+1) - F_0(r)}{\gamma(r) p_0(r) F_0(r) F_\ell(r)} = -\frac{\delta(r-s)}{\gamma(r) p_0(r) F_0(r)}. \end{aligned} \quad (4.50)$$

• The second term gives

$$\begin{aligned} I_2 &= \frac{\ell(\ell+1)}{F_\ell(r) F_\ell(s)} \left(2 - s \frac{\alpha_{p_0}(s)}{\gamma(s)} \right) r \partial_r G_\ell^{\text{PP}} + \frac{\ell(\ell+1)}{F_\ell(r) F_\ell(s)} \left(2 - r \frac{\alpha_{p_0}(r)}{\gamma(r)} \right) s \partial_s G_\ell^{\text{PP}} \\ &= -\frac{\ell(\ell+1)}{F_\ell(r) F_\ell(s)} \left(2 - s \frac{\alpha_{p_0}(s)}{\gamma(s)} \right) \frac{\mathbf{p}(s)}{s^2} r \partial_r \mathbb{G}_\ell^+ - \frac{\ell(\ell+1)}{F_\ell(r) F_\ell(s)} \left(2 - r \frac{\alpha_{p_0}(r)}{\gamma(r)} \right) \frac{\mathbf{p}(s)}{s^2} s \partial_s \mathbb{G}_\ell^+. \end{aligned} \quad (4.51)$$

The final expression is obtained by using (4.45).

• **Symmetry result** With the symmetry of \mathbb{Q}_ℓ^+ , \mathbb{G}_ℓ^+ and constant $\frac{\mathbf{p}(s)}{s^2}$, we have

$$G_\ell^{\text{BBreg}}(r, s) = G_\ell^{\text{BBreg}}(s, r), \quad G_\ell^{\text{PP}}(r, s) = G_\ell^{\text{PP}}(s, r), \quad G_\ell^{\text{PB}}(r, s) = G_\ell^{\text{BP}}(s, r). \quad (4.52)$$

The symmetry of G_ℓ^{BBreg} is due to

$$\frac{1}{F_\ell(r)} \frac{1}{\mathcal{W}_\ell^+(s) \mathfrak{F}(s) s^2} = \frac{1}{F_\ell(r) F_\ell(s)} \frac{\mathbf{p}(s)}{s^2}. \quad (4.53)$$

□

Formal expansion of the 3D kernel For a source such that

$$\mathbf{f} = \mathbf{f}^\perp + \mathbf{f}^\parallel, \quad \mathbf{f}^\perp = f_r \mathbf{e}_r, \quad \mathbf{f}^\parallel = \mathbf{f}^h + \mathbf{f}^\times = \mathbf{f} - \mathbf{f}^\perp, \quad (4.54)$$

the solution $\boldsymbol{\xi}$ to $\mathcal{L}_{\text{SG}}\boldsymbol{\xi} = \mathbf{f}$ is given by

$$\boldsymbol{\xi}(\mathbf{x}) = \tilde{\boldsymbol{\xi}}(\mathbf{x}) - \frac{|\mathbf{x}|^2}{\mathfrak{F}(|\mathbf{x}|)} \mathbf{f}^\parallel(\mathbf{x}), \quad (4.55)$$

where

$$\tilde{\boldsymbol{\xi}}(\mathbf{x}) = \langle \mathbb{G}_{\text{reg}}(\mathbf{x}, \mathbf{y}), \mathbf{f}(\mathbf{y}) \rangle = \langle \mathbb{G}_\perp(\mathbf{x}, \mathbf{y}), \mathbf{f}^\perp(\mathbf{y}) \rangle + \langle \mathbb{G}_{\text{h-reg}}(\mathbf{x}, \mathbf{y}), \mathbf{f}^h(\mathbf{y}) \rangle, \quad (4.56)$$

with the scalar modal kernel given in [Proposition 2](#):

$$\mathbb{G}_{\text{reg}}(\mathbf{x}, \mathbf{y}) = \mathbb{G}_\perp(\mathbf{x}, \mathbf{y}) + \mathbb{G}_{\text{h-reg}}(\mathbf{x}, \mathbf{y}), \quad (4.57)$$

having formal decomposition

$$\begin{aligned} \mathbb{G}_\perp(\mathbf{x}, \mathbf{y}) &= \sum_{\ell=0}^{\infty} \sum_{m=-\infty}^{\infty} G_\ell^{\text{PP}}(|\mathbf{x}|, |\mathbf{y}|) \mathbf{P}_\ell^m(\hat{\mathbf{x}}) \otimes \overline{\mathbf{P}_\ell^m(\hat{\mathbf{y}})} \\ &\quad + \sum_{\ell=1}^{\infty} \sum_{m=-\infty}^{\infty} G_\ell^{\text{BP}}(|\mathbf{x}|, |\mathbf{y}|) \mathbf{B}_\ell^m(\hat{\mathbf{x}}) \otimes \overline{\mathbf{P}_\ell^m(\hat{\mathbf{y}})}; \\ \mathbb{G}_{\text{h-reg}}(\mathbf{x}, \mathbf{y}) &= \sum_{\ell=1}^{\infty} \sum_{m=-\infty}^{\infty} G_\ell^{\text{PB}}(|\mathbf{x}|, |\mathbf{y}|) \mathbf{P}_\ell^m(\hat{\mathbf{x}}) \otimes \overline{\mathbf{B}_\ell^m(\hat{\mathbf{y}})} \\ &\quad + \sum_{\ell=1}^{\infty} \sum_{m=-\infty}^{\infty} G_\ell^{\text{BBreg}}(|\mathbf{x}|, |\mathbf{y}|) \mathbf{B}_\ell^m(\hat{\mathbf{x}}) \otimes \overline{\mathbf{B}_\ell^m(\hat{\mathbf{y}})}. \end{aligned} \quad (4.58)$$

If we formally¹⁰ write (4.55) as

$$\boldsymbol{\xi} = \langle \mathbb{G}^+, \mathbf{f} \rangle, \quad (4.59)$$

then with \mathbb{P}_\parallel the projection on the tangential plane that is normal to \mathbf{e}_r (i.e. $\mathbb{P}_\parallel = \mathbb{I}d - \mathbf{e}_r(\hat{\mathbf{x}}) \otimes \mathbf{e}_r(\hat{\mathbf{y}})$),

$$\mathbb{G}^+(\mathbf{x}, \mathbf{y}) = \mathbb{G}_{\text{reg}}(\mathbf{x}, \mathbf{y}) - \frac{|\mathbf{x}|^2}{\mathfrak{F}(|\mathbf{x}|)} \delta(\mathbf{x} - \mathbf{y}) \mathbb{P}_\parallel. \quad (4.60)$$

Remark 13. Compared to the notation and choice of VSH basis in [10, Equation (11) or (A13)], cf. (2.27) in [Remark 2](#), we have the following identification,

$$\begin{aligned} G_\ell^{\text{PP}} &\leftrightarrow G_{(-1),\ell}^{(-1)}, & G_\ell^{\text{PB}} &\leftrightarrow G_{(1),\ell}^{(-1)}, \\ G_\ell^{\text{BP}} &\leftrightarrow G_{(-1),\ell}^{(1)}, & G_\ell^{\text{BB}} &\leftrightarrow G_{(1),\ell}^{(1)}. \end{aligned} \quad \diamond$$

5 Numerical computation working with original equation \mathfrak{L}_ℓ

In this section, we discuss how to implement the theoretical results of [Sections 3](#) and [4](#) to compute the coefficients in VSH expansions of the 3D Green's kernel

$$G_\ell^{\text{PP}}, \quad G_\ell^{\text{PB}}, \quad G_\ell^{\text{BP}}, \quad G_\ell^{\text{BB}}. \quad (5.1)$$

We recall that one can either work¹¹ with the conjugated operator \mathcal{L}_ℓ or the original one \mathfrak{L}_ℓ . However, due to the regularity (3.101) of the solutions of \mathfrak{L}_ℓ in the vicinity of the singular point r_* (without

¹⁰The discussion is heuristic since we have not specified \mathbb{G} as a mathematical object. To obtain this type of statement, one needs to study the convergence of the summand in (4.58), e.g., to give an object in the space of distribution. Such a result also establishes existence of \mathbb{G}^+ . At the same time, one will also need a uniqueness result for the outgoing kernel \mathbb{G}^+ . So far, the outgoingness is only characterized for the modal components. Due to the independence of the phase function ψ on ℓ , it should be expected for \mathbb{G}^+ .

¹¹This means that one computes G_ℓ^+ and the quantities (5.1) directly by solving equation with \mathfrak{L}_ℓ . In the approach using \mathcal{L}_ℓ , one first computes G_ℓ^+ and related homogeneous solutions φ_ℓ^+ , φ_ℓ , and the final quantities are constructed from these, using the relation between the original and the conjugated operator, cf. [Appendix A.1](#).

attenuation), as discussed in [Subsection 3.3](#), it is numerically more stable at small attenuation ($\Gamma \ll 1$) and $\ell > 0$, to work with the original problem, which we recall here:

$$\mathfrak{L}_\ell = \hat{q}_\ell \partial_r^2 + q_\ell \partial_r + \tilde{q}_\ell, \quad \text{cf. (3.29)}.$$

Numerical experiments in demonstrating the robustness of the approach (versus the conjugated one) are given in [Section 7](#). For this purpose, a brief discussion is also given in [Appendix A](#) for the approach working with \mathcal{L}_ℓ .

Within each choice (to work with \mathcal{L}_ℓ or \mathfrak{L}_ℓ), there are two approaches to arrive at the final quantities (5.1), cf. discussion in [Subsection 5.2](#). The first approach referred to as the *direct approach* is to discretize directly the right-hand side Dirac source. One first obtains G_ℓ^+ and then G_ℓ^{PP} for each source position. The remaining quantities in (5.1) are computed from G_ℓ^{PP} and its derivatives (e.g., by means of finite difference). The second approach is to exploit the gluing formula obtained in [Section 4](#), in particular [Proposition 2](#), which provides explicit expressions of (5.1) in terms of the regular-at-zero and outgoing solutions, respectively ϕ_ℓ and ϕ_ℓ^+ , of \mathcal{L}_ℓ and their derivatives.

We first formulate the problem and solve it using the Hybridizable Discontinuous Galerkin method (HDG), which works with the first-order formulation. A notable feature of HDG method is its global unknown which is the trace of the numerical solution on the skeleton of the mesh (i.e., only on the faces of the cells). The first-order system is discussed in [Subsection 5.3](#). The explicit discretized problems are given in [Subsection 5.4](#). A summary of the ‘gluing’ approach written in first-order formulation is given in [Algorithm 1](#). We will implement this algorithm using HDG method discussed in [Subsection 5.4](#) to carry out the numerical experiments of [Section 7](#). A summary for the direct approach is given at the end of [Subsection 5.3](#), see (5.29).

5.1 Boundary conditions

We first return to the problems (3.86)–(3.88) which define respectively G_ℓ^+ , ϕ_ℓ and ϕ_ℓ^+ , and replace the characterization at $r = 0$ and $r \rightarrow \infty$, by boundary conditions on the truncated domain $[0, r_{\max}]$. Note that this step was also carried out for the modal operator $\mathcal{L}_\ell^{\text{scalar}}$ (3.44) for the scalar equation in [3, Section 2.3]. The new boundary condition (5.3) at $r = 0$ is equivalent to the original one which serves to pick out the regular solution there. On the other hand, a new boundary condition imposed at $r = r_{\max}$ replaces the characterization at $r \rightarrow \infty$ and provides a mean to approximate numerically the outgoing solution.

Boundary conditions at $r = 0$ G_ℓ^+ and ϕ_ℓ are regular at $r = 0$ with exponent λ_ℓ^+ where

$$\lambda_0^+ = 1, \quad \lambda_0^- = 2; \quad \lambda_\ell^+ = \ell - 1, \quad \lambda_\ell^- = -\ell - 2, \quad \text{for } \ell > 0. \quad (5.2)$$

Thus the ‘regular-at-zero’ solution is chosen by

$$\boxed{\lim_{r \rightarrow 0} r \partial_r G_\ell^+ = 0.} \quad (5.3)$$

Remark 14. *In working with the original modal operator \mathfrak{L}_ℓ , to choose the regular-at-zero solution, there is no division by r in the BC at $r = 0$, unlike boundary condition (A.8) for \mathcal{L}_ℓ . Applying (A.8) to the homogeneous solutions of \mathfrak{L}_ℓ yields only expressions singular for $\ell = 1$ and would thus disqualify both families. See also discussion in [Remark 20](#). \diamond*

Radiation Boundary condition The behavior as $r \rightarrow \infty$ of G_ℓ^+ and ϕ_ℓ^+ come from \mathcal{G}_ℓ^+ and φ_ℓ^+ (outgoing Green’s function and solution of \mathcal{L}_ℓ). RBC are constructed by working with conjugate modal operator \mathcal{L}_ℓ due to its Schrödinger form. Concretely this facilitates the factorization of the operator. The constructed RBC associated to \mathcal{L}_ℓ are of impedance type and of the form,

$$\partial_n \tilde{u} = i\mathcal{Z}(r) \tilde{u}, \quad \text{in } r = r_{\max}. \quad (5.4)$$

More details on the constructions of the coefficient \mathcal{Z} are given in [Section 6](#). In this section, we discuss how the corresponding RBC for the original operator \mathfrak{L}_ℓ are obtained from (5.4) using the relation between the original and conjugate solutions (3.13).

The original and conjugate solutions u and \tilde{u} are related by

$$u = \tilde{u} \mathfrak{J}_\ell, \quad \text{and} \quad \tilde{u} \text{ satisfies (5.4) at } r = r_{\max}. \quad (5.5)$$

We also suppose that r_{\max} satisfies,

$$r_{\max} \neq r_\star \quad (\iff \quad \mathfrak{J}_\ell(r_{\max}) \neq 0). \quad (5.6)$$

Replacing \tilde{u} by u using relation (5.5) in (5.4),

$$\begin{aligned} \tilde{u}'(r_{\max}) &= i \mathcal{Z}(r_{\max}) \tilde{u}(r_{\max}) \\ \Leftrightarrow \quad \left(\frac{u}{\mathfrak{J}_\ell} \right)'(r_{\max}) &= i \mathcal{Z}(r_{\max}) \frac{u(r_{\max})}{\mathfrak{J}_\ell(r_{\max})} \\ \Leftrightarrow \quad \frac{u'(r_{\max})}{\mathfrak{J}_\ell(r_{\max})} &= \left(i \mathcal{Z}(r_{\max}) + \frac{\mathfrak{J}'_\ell(r_{\max})}{\mathfrak{J}_\ell(r_{\max})} \right) \frac{u(r_{\max})}{\mathfrak{J}_\ell(r_{\max})}. \end{aligned} \quad (5.7)$$

We thus arrive at the RBC for u ,

$$\mathfrak{J}_\ell(r_{\max}) u'(r_{\max}) = i \mathcal{N}(r_{\max}) u(r_{\max}), \quad (5.8)$$

with modified RBC coefficient \mathcal{N} ,

$$\boxed{\mathcal{N}(r) := \mathcal{Z}(r) \mathfrak{J}_\ell(r) - i \mathfrak{J}'_\ell(r)}. \quad (5.9)$$

The factor in front of u' in the last expression is to avoid division by $\mathfrak{J}_\ell(r_{\max})$ when r_{\max} is close to r_\star . In particular, to compute G_ℓ^+ numerically directly with \mathcal{L}_ℓ , one uses the RBC,

$$\boxed{\mathfrak{J}_\ell(r_{\max}) \partial_r G_\ell^+(r_{\max}) = i \mathcal{N}(r_{\max}) G_\ell^+(r_{\max})}. \quad (5.10)$$

5.2 Approaches to compute G_ℓ^+

In the rest of the section we assume (5.6).

Approach 1 (Direct) For a fixed value of $s_0 \in (0, r_{\max})$, this approach gives $G_\ell^+(r, s_0)$ for $r \in (0, r_{\max})$ as the solution of

$$\begin{cases} (\hat{q}_\ell \partial_r^2 + q_\ell \partial_r + \tilde{q}_\ell) G_\ell^+ = \delta(r - s_0) & \text{on } [0, r_{\max}]; \end{cases} \quad (5.11a)$$

$$\begin{cases} (r \partial_r G_\ell^+)(0) = 0; \end{cases} \quad (5.11b)$$

$$\begin{cases} \mathfrak{J}_\ell(r_{\max}) \partial_r G_\ell^+(r_{\max}) = i \mathcal{N}(r_{\max}) G_\ell^+(r_{\max}). \end{cases} \quad (5.11c)$$

Approach 2 (Assemblage) With $r_{\min} > 0$ and $r_b \leq r_{\max}$, this approach gives the value of $G_\ell^+(r, s)$ for all $r \in [0, r_{\max}]$ and $s \in [r_{\min}, r_b]$, as illustrated in Figure 4. One first computes a solution in the ‘regular-at-zero’ family ϕ_ℓ on $[0, r_b]$, that solves,

$$\begin{cases} (\hat{q}_\ell \partial_r^2 + q_\ell \partial_r + \tilde{q}_\ell) \phi_\ell = 0 & \text{on } [0, r_b]; \end{cases} \quad (5.12a)$$

$$\begin{cases} \lim_{r \rightarrow 0} r \partial_r \phi_\ell = 0; & \phi_\ell(r_b) = \mathfrak{J}_\ell(r_b). \end{cases} \quad (5.12b)$$

Secondly, one computes a solution ϕ^+ in the outgoing family on $[r_{\min}, r_{\max}]$, that solves,

$$\begin{cases} (\hat{q}_\ell \partial_r^2 + q_\ell \partial_r + \tilde{q}_\ell) \phi_\ell^+ = 0 & \text{on } [r_{\min}, r_{\max}]; \end{cases} \quad (5.13a)$$

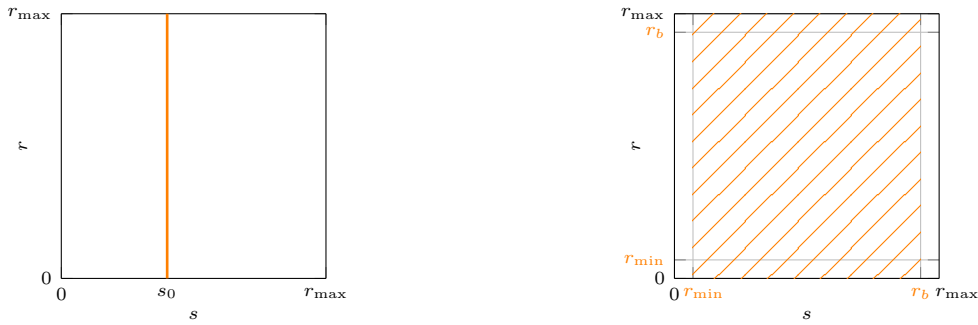
$$\begin{cases} \phi_\ell^+(r_{\min}) = \mathfrak{J}_\ell(r_{\min}); & \mathfrak{J}_\ell(r_{\max}) \partial_r \phi_\ell^+(r_{\max}) = i \mathcal{N}(r_{\max}) \phi_\ell^+(r_{\max}). \end{cases} \quad (5.13b)$$

The quantities in (5.1) and the Green's kernel $G_\ell^+(r, s)$ restricted on $r \in [0, r_{\max}]$, $s \in [r_{\min}, r_b]$ are then computed analytically from ϕ_ℓ , ϕ_ℓ^+ and their first-order derivatives as given in Proposition 2 and (3.90). As an example, G_ℓ^+ is obtained by formula,

$$G_\ell^+(r, s) := \frac{\mathbb{H}(s-r)\phi_\ell(r)\phi_\ell^+(s) + \mathbb{H}(r-s)\phi_\ell(s)\phi_\ell^+(r)}{\hat{q}_\ell(s)\mathcal{W}\{\phi_\ell, \phi_\ell^+\}(s)}. \quad (5.14)$$

Below we make a remark Remark 15 to point out the disadvantages of Approach 1. We will also discuss in Remark 16 the choice of the Dirichlet trace in (5.12b) and (5.13b).

Remark 15 (Downside of Approach 1). *Since Approach 1 gives $r \mapsto G_\ell^+(r, s_0)$ for each run at a fixed s_0 , by using first-order formulation, we can obtain $G_\ell^+(r, s_0)$ and its derivative $\partial_r G_\ell^+(\cdot, s_0)$. In order to obtain the derivative in s , one either uses finite difference assuming enough sources are calculated, or one will have to resort to reciprocity. As stated in Algorithm 1, the second approach gives explicitly (using HDG discretization) both derivatives in r and s , as well as the second derivative $\partial_r \partial_s$ in order to obtain the non radial components of the Green's kernels.* \diamond



(a) Approach 1: the solution of one problem for a delta-Dirac source in s_0 only gives $G_\ell^+(r, s = s_0)$.

(b) Approach 2: from the solutions of two boundary value problems, $G_\ell^+(r, s)$ is obtained for any position of $r \in [0, r_{\max}]$ and $s \in [r_{\min}, r_b]$.

Figure 4: Domain of definition (orange) for the modal Green's function G_ℓ^+ using Approach 1 and 2, defined respectively by (5.11) and (5.14).

Remark 16. Recall that from (3.92), any representative of the regular-at-zero and outgoing family is, for some constant $c, d \neq 0$,

$$\phi_{\text{generic}}^+(r) = c\mathfrak{I}_\ell(r)\varphi^+(r), \quad \phi_{\text{generic}}(r) = d\mathfrak{I}_\ell(r)\varphi(r).$$

The choice in (5.12) and (5.13) corresponds to $c = d = 1$ in (3.93), i.e.,

$$\phi_\ell(r) = \mathfrak{I}_\ell(r)\varphi_\ell(r); \quad \phi_\ell^+(r) = \mathfrak{I}_\ell(r)\varphi_\ell^+(r). \quad (5.15)$$

Normally, in working directly with the original operator \mathcal{L}_ℓ , a more canonical choice is the 'regular' solution $\check{\phi}_\ell$ which solves,

$$\begin{cases} (\hat{q}_\ell \partial_r^2 + q_\ell \partial_r + \tilde{q}_\ell) \check{\phi}_\ell = 0 & \text{on } [0, r_b]; \\ \lim_{r \rightarrow 0} r \partial_r \check{\phi}_\ell = 0; & \check{\phi}_\ell(r_b) = 1, \end{cases} \quad (5.16a)$$

$$\quad (5.16b)$$

and the outgoing solution $\check{\phi}_\ell^+$ which solves,

$$\begin{cases} (\hat{q}_\ell \partial_r^2 + q_\ell \partial_r + \tilde{q}_\ell) \check{\phi}_\ell^+ = 0 & \text{on } [r_{\min}, r_{\max}]; \\ \check{\phi}_\ell^+(r_{\min}) = 1; & \mathfrak{I}_\ell(r_{\max}) \partial_r \check{\phi}_\ell^+(r_{\max}) = i\mathcal{N}(r_{\max}) \check{\phi}_\ell^+(r_{\max}). \end{cases} \quad (5.17a)$$

$$\quad (5.17b)$$

they are related to φ_ℓ and φ_ℓ^+ and (ϕ_ℓ, ϕ_ℓ^+) as

$$\begin{aligned}\check{\phi}_\ell(r) &= \frac{\phi(r)}{\mathfrak{I}_\ell(r_b)} = \frac{\mathfrak{I}_\ell(r)}{\mathfrak{I}_\ell(r_b)} \varphi(r); \\ \check{\phi}_\ell^+(r) &= \frac{\phi^+(r)}{\mathfrak{I}_\ell(r_{\max})} = \frac{\mathfrak{I}_\ell(r)}{\mathfrak{I}_\ell(r_{\max})} \varphi^+(r).\end{aligned}\tag{5.18}$$

With ϕ_ℓ and ϕ_ℓ^+ continuous for $r > 0$, working with $\check{\phi}_\ell$ and $\check{\phi}_\ell^+$ can be numerically unstable due to the division by $\mathfrak{I}_\ell(r_{\max})$ for cases where r_{\max} is close to r_\star . \diamond

5.3 First-order formulation

We rewrite the boundary value problems (5.11)–(5.13) satisfied respectively by ϕ_ℓ , ϕ_ℓ^+ and G_ℓ^+ as first-order systems. First, we unify these problems under the generic form,

$$(\hat{q}_\ell \partial_r^2 + q_\ell \partial_r + \tilde{q}_\ell) w = f, \quad \text{on } [r_{\min}, r_{\max}], \tag{5.19a}$$

$$(\mathfrak{B}w)(r_{\min}) = g, \quad (\tilde{\mathfrak{B}}w)(r_{\max}) = \tilde{g}, \tag{5.19b}$$

where the boundary trace operators \mathfrak{B} and $\tilde{\mathfrak{B}}$ are given in Table 2. Additionally, we will need to introduce the regularized form of the equations due to the singularities of the coefficients, as discussed in Subsection 3.2.1.

Regularized first-order problem The variables for the first-order formulation of (5.19) are chosen to be compatible¹² with the BC (5.3) at $r = 0$. A choice is given by

$$w, \quad v := r w'. \tag{5.20}$$

New boundary conditions in terms of (w, v) , denoted by $\mathfrak{B}(w, v)$, are given in Table 2 with the original ones (in terms of w).

Table 2: Boundary conditions associated to the first-order formulation in terms of (w, v) with $v = r w'$ of the original modal equation $\hat{q}_\ell \partial_r^2 + q_\ell \partial_r + \tilde{q}_\ell$.

$r \in \Sigma_\bullet$	$\mathfrak{B}_\bullet w = g_\bullet$	$\mathfrak{B}_\bullet(w, v) = g_\bullet$
$\bullet = \text{d}$	$w(r) = g_{\text{d}}$	$w(r) = g_{\text{d}}$
$\bullet = \text{dv}$	$(r w')(r) = g_{\text{dv}}$	$v(r) = g_{\text{dv}}$
$\bullet = \text{a}$	$\mathfrak{I}_\ell(r) w'(r) - i \mathcal{N}(r) w(r) = g_{\text{a}}$	$\frac{\mathfrak{I}_\ell(r)}{r} v(r) - i \mathcal{N}(r) w(r) = g_{\text{a}}$

Due to the singularity of the coefficients (discussed in Subsection 3.2.1), we will also multiply the equations by a regularizing factor. We distinguish the following two cases.

1. For $\ell > 0$, with a chosen regularized factor f_{reg} , define the ‘regularized’ coefficients starting from \hat{q} , q and \tilde{q} ,

$$\hat{q}_{\text{reg}} := \frac{f_{\text{reg}} \hat{q}_\ell}{r^2}, \quad q_{\text{reg}} := -f_{\text{reg}} \frac{\hat{q}_\ell}{r^2} + f_{\text{reg}} \frac{q_\ell}{r}, \quad \tilde{q}_{\text{reg}} = \tilde{q}_\ell f_{\text{reg}}. \tag{5.21}$$

The assumption is that the coefficients in (5.21) are regular. We regularize (5.19a) by multiplying both sides by a factor f_{reg} and after some algebraic manipulation, we arrive at¹³,

$$\hat{q}_{\text{reg}} r v' + q_{\text{reg}} v + \tilde{q}_{\text{reg}} w = f_{\text{reg}} f; \quad v = r w'. \tag{5.23}$$

¹²We thus note a difference with the definition of the first-order variables (A.17) for the equation with \mathcal{L}_ℓ .

¹³This is seen by writing

$$\begin{aligned}\hat{q}_\ell \partial_r^2 + q_\ell \partial_r + \tilde{q}_\ell &= \frac{\hat{q}_\ell}{r^2} r^2 \partial_r^2 + \frac{q_\ell}{r} r \partial_r + \tilde{q}_\ell = \frac{\hat{q}_\ell}{r^2} \left((r \partial_r)^2 - r \partial_r \right) + \frac{q_\ell}{r} r \partial_r + \tilde{q}_\ell \\ &= \frac{\hat{q}_\ell}{r^2} (r \partial_r)^2 + \left(-\frac{\hat{q}_\ell}{r^2} + \frac{q_\ell}{r} \right) r \partial_r + \tilde{q}_\ell.\end{aligned}\tag{5.22}$$

2. When coefficient \hat{q} is a constant and the other two contain only singularity at $r = 0$, which is the case at $\ell = 0$ for the coefficients of \mathfrak{L}_ℓ , we define the regularized coefficients

$$\boxed{\hat{q}_{\text{reg}} := \hat{q}_0, \quad q_{\text{reg}} := -\hat{q}_0 + r q_0, \quad \tilde{q}_{\text{reg}} = \tilde{q}_0 r^2,} \quad (5.24)$$

and the regularized version of (5.21) is given as,

$$\hat{q}_{\text{reg}} r v' + q_{\text{reg}} v + \tilde{q}_{\text{reg}} w = r^2 f; \quad v = r w'. \quad (5.25)$$

We next compute the regularized coefficients associated with \mathfrak{L}_ℓ , starting from the explicit expression of its coefficients given in (3.28) and (3.29).

1. For $\ell > 0$, the singularities are at $r = 0$ and $r = r_*$, the latter creates difficulty for nonzero but small attenuation Γ see Subsection 7.2. We employ formula (5.21) with regularizing factor $f_{\text{reg}} = F_\ell^2$. Together with the explicit expression of \hat{q}_ℓ , q_ℓ and \tilde{q}_ℓ in (3.29), we obtain

$$\hat{q}_{\text{reg}} = -\frac{F_0}{r^2} F_\ell; \quad (5.26a)$$

$$q_{\text{reg}} = (r\alpha_{\gamma p_0} - 1) \frac{F_0}{r^2} F_\ell + \ell(\ell + 1) \frac{F_0'}{r}; \quad (5.26b)$$

$$\begin{aligned} \tilde{q}_{\text{reg}} = & \left(-k_0^2 + \frac{\phi_0''}{c_0^2} \right) F_0 F_\ell + \left(2 + 2r \left(\alpha_{\gamma p_0} - \frac{\alpha_{p_0}}{\gamma} \right) \right) \frac{F_0}{r^2} F_\ell \\ & + \ell(\ell + 1) F_\ell \left(k_0^2 - \frac{\phi_0''}{c_0^2} + \left(\frac{\alpha_{p_0}}{\gamma} \right)' + \frac{\alpha_{p_0}}{\gamma} \left(-\alpha_{\gamma p_0} + \frac{\alpha_{p_0}}{\gamma} \right) \right) \\ & + \ell(\ell + 1) \left(2 - r \frac{\alpha_{p_0}}{\gamma} \right) \frac{F_0'}{r}. \end{aligned} \quad (5.26c)$$

Note that $\frac{F_0(r)}{r^2}$ and $\frac{F_0'}{r}$ are regular functions¹⁴, and so are the functions in (5.26).

2. For $\ell = 0$, the regularized coefficients are computed using (5.24) and the definition of q_0 , \tilde{q}_0 and \hat{q}_0 in (3.28),

$$\begin{aligned} \hat{q}_{\text{reg}} &= -1; & q_{\text{reg}} &= r\alpha_{\gamma p_0} - 1; \\ \tilde{q}_{\text{reg}} &= -k_0^2 r^2 + \frac{\phi_0''}{c_0^2} r^2 + 2 + 2r \left(\alpha_{\gamma p_0} - \frac{\alpha_{p_0}}{\gamma} \right). \end{aligned} \quad (5.27)$$

In Figure 5, we plot the ratio of the different terms in the ODE in the case of solar background models. It highlights that the dominant term is \tilde{q}_{reg} in our experiments, which is greater than \hat{q}_{reg} by an three orders of magnitude, while it is greater than q_{reg} by four orders of magnitude.

Algorithms to compute the modal Green's kernels We restate explicitly the two approaches discussed in Subsection 5.2 to compute G_ℓ^+ and the quantities (5.1) in form of regularized first-order formulation, and with coefficients given by (5.27) for $\ell = 0$ and (5.26) for $\ell > 0$.

- **Approach 1** (direct approach): with right-hand side

$$f_0 = r^2 \delta(r - s), \quad f_\ell = f_{\text{reg}} \delta(r - s), \quad \text{for } \ell > 0, \quad (5.28)$$

find (v, w) that solves

$$\begin{cases} \hat{q}_{\text{reg}} r v' + q_{\text{reg}} v + \tilde{q}_{\text{reg}} w = f_\ell, & \text{on } (0, r_{\text{max}}), \\ v - r w' = 0, & \text{on } (0, r_{\text{max}}), \\ v(0) = 0, \quad \frac{\mathfrak{I}_\ell(r_{\text{max}})}{r_{\text{max}}} v(r_{\text{max}}) - i\mathcal{N}(r_{\text{max}}) w(r_{\text{max}}) = 0. \end{cases} \quad (5.29)$$

¹⁴We recall here their definition on $r \leq r_s$,

$$F_0(r) = k_0^2 r^2, \quad F_0'(r) = (k_0^2)' r^2 + k_0^2 2r, \quad \frac{F_0(r)}{r^2} = k_0^2, \quad \frac{F_0'}{r} = (k_0^2)' r + 2k_0^2.$$

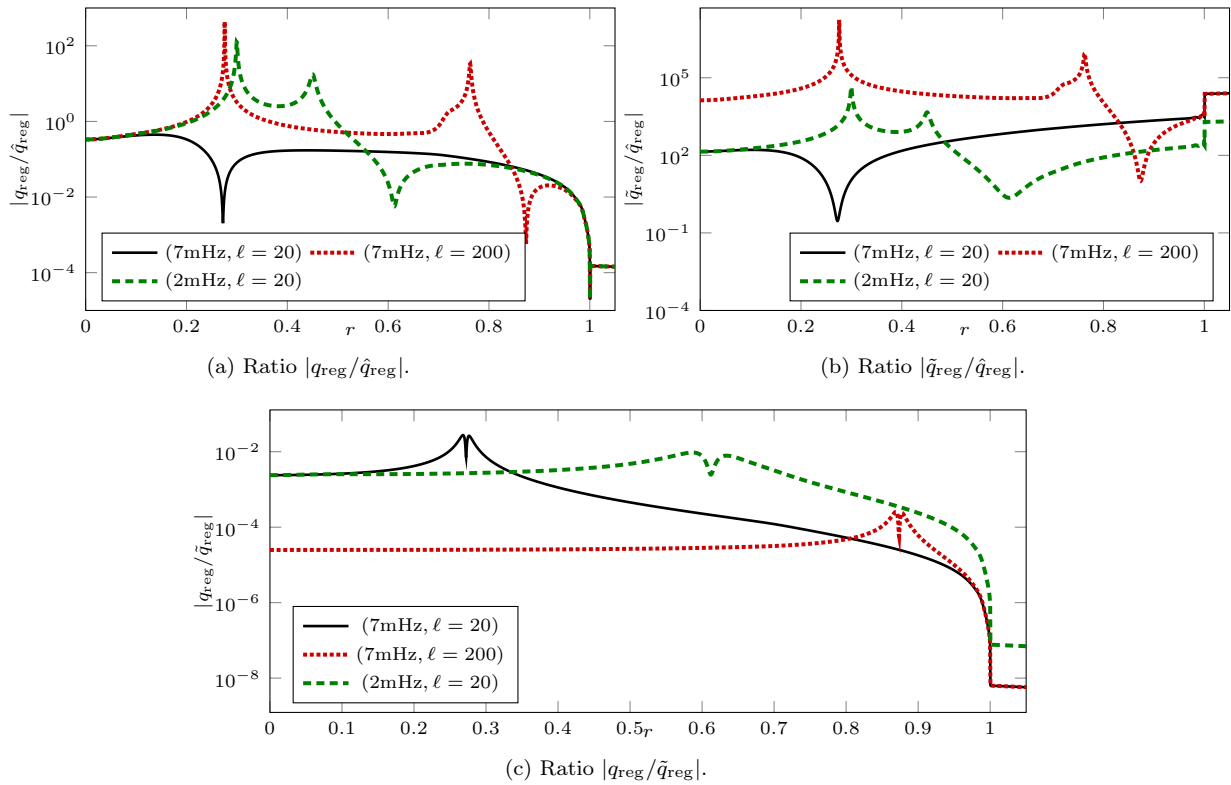


Figure 5: Comparison of the terms in the ODE considering the solar background model S-AtmoI for different modes and frequencies.

We can obtain the following quantities

$$\begin{aligned}
 G_\ell^+(\cdot, s) &= w, & r\partial_r G_\ell^+(\cdot, s) &= v, \\
 G_\ell^{\text{PP}}(r, s) &= \frac{G_\ell^+(\cdot, s)}{c_0^2(s)\rho_0(s)s^2}, & r\partial_r G_\ell^{\text{PP}}(r, s) &= \frac{r\partial_r G_\ell^+(r, s)}{c_0^2(s)\rho_0(s)s^2}.
 \end{aligned} \tag{5.30}$$

To obtain the quantities in (5.1), one has to differentiate numerically to obtain the derivatives $s\partial_s G_\ell^{\text{PP}}$ and $r\partial_r s\partial_s G_\ell^{\text{PP}}$. This also implies that one needs to obtain the value of $G_\ell^{\text{PP}}(r, s_0)$ for several values of s_0 in order to compute the derivative in s . This contributes to the downside of the approach, cf. Remark 15.

- **Approach 2** (assemblage approach): We use the gluing formula to compute the Green’s kernel, as described in Algorithm 1.

5.4 Discretization with HDG method

We discuss the main ingredients of solving the generic problem on $\Omega = (r_{\min}, r_{\max})$ with the HDG method,

$$\begin{cases}
 \hat{q}_{\text{reg}} r v' + q_{\text{reg}} v + \tilde{q}_{\text{reg}} w = 0, & \text{on } (r_{\min}, r_{\max}); & (5.36a) \\
 v - r w' = 0, & \text{on } (r_{\min}, r_{\max}); & (5.36b) \\
 \mathfrak{B}(w, v)|_{r_{\min}} = g_L; & \tilde{\mathfrak{B}}(w, v)|_{r_{\max}} = g_R. & (5.36c)
 \end{cases}$$

The boundary operators \mathfrak{B} are listed in Table 2. We only list here the final results, and refer to [4, Section 6] for more details on the HDG method¹⁵. Compared to [4, Section 6], and Appendix A.2, the

¹⁵We note that the discretization given in Appendix A.2 is slightly different from [4, Section 6] because it works with the regularized form. If the regularized factor in Appendix A.2 is set to 1, one obtains the form the elementary matrices of [4,

Algorithm 1 Approach 2: computation at fixed (ω, ℓ) of the quantities G_ℓ^{PP} , G_ℓ^{PB} and G_ℓ^{BBreg} , G_ℓ^{BP} using first-order formulation (in working with the original modal operator $\hat{q}_\ell \partial_r^2 + q_\ell \partial_r + \tilde{q}_\ell$). The regularized coefficients are given by (5.27) for $\ell = 0$ and (5.26) for $\ell > 0$. We have $0 < r_{\min}$ and $r_b \leq r_{\max}$.

Step 1a. With $c = 1$ or $\mathcal{I}_\ell(r_b)$. Find (v, w) that solves

$$\begin{cases} \hat{q}_{\text{reg}} r v' + q_{\text{reg}} v + \tilde{q}_{\text{reg}} w = 0, & \text{on } (0, r_b); \\ v - r w' = 0, & \text{on } (0, r_b); \\ v(0) = 0, \quad w(r_b) = c, \end{cases} \quad (5.31)$$

Set $\phi_\ell := w$, $\partial_r \phi_\ell := \frac{v}{r}$, and $r \partial_r \phi_\ell := v$.

Step 1b. With $d = 1$ or $\mathcal{I}_\ell(r_{\min})$. Find (v, w) that solves

$$\begin{cases} \hat{q}_{\text{reg}} r v' + q_{\text{reg}} v + \tilde{q}_{\text{reg}} w = 0, & \text{on } (r_{\min}, r_{\max}); \\ v - r w' = 0, & \text{on } (r_{\min}, r_{\max}); \\ w(r_a) = d, \quad \frac{\mathcal{I}_\ell(r_{\max})}{r_{\max}} v(r_{\max}) - i \mathcal{N}(r_{\max}) w(r_{\max}) = 0. \end{cases} \quad (5.32)$$

Set $\phi_\ell^+ := w$, $\partial_r \phi_\ell^+ := \frac{v}{r}$ and $r \partial_r \phi_\ell^+ = v$

Step 2a. Calculate for each point $s \in [r_{\min}, r_b]$ and $r \in [0, r_{\max}]$,

$$\begin{aligned} \mathcal{W}_\ell^+(s) &= \phi_\ell(s) \partial_s \phi_\ell^+(s) - \phi_\ell^+(s) \partial_s \phi_\ell(s); \\ \mathfrak{F}(r) &:= c_0^2(r) \rho_0(r) F_0(r), \end{aligned} \quad (5.33)$$

Step 2b. Compute G_ℓ^+ , T_ℓ^+ , Q_ℓ^+ for $r \in [0, r_{\max}]$. They are given by

$$G_\ell^+(r, s) := H(s - r) \phi_\ell(r) \phi_\ell^+(s) + H(r - s) \phi_\ell(s) \phi_\ell^+(r); \quad (5.34a)$$

$$T_\ell^+(r, s) := H(s - r) r \partial_r \phi_\ell(r) \phi_\ell^+(s) + H(r - s) \phi_\ell(s) r \partial_r \phi_\ell^+(r); \quad (5.34b)$$

$$Q_\ell^+(r, s) := H(s - r) r \partial_r \phi_\ell(r) s \partial_s \phi_\ell^+(s) + H(r - s) s \partial_s \phi_\ell(s) r \partial_r \phi_\ell^+(r). \quad (5.34c)$$

Step 2c. Assemble the Green's functions using Proposition 2

$$\begin{aligned} G_\ell^{\text{PP}}(r, s) &= -G_\ell^+(r, s) \frac{F_\ell(s)}{\mathcal{W}_\ell^+(s) \mathfrak{F}(s) s^2}; \\ G_\ell^{\text{BP}}(r, s) &= \sqrt{\ell(\ell + 1)} \left[T_\ell^+(r, s) + G_\ell^+(r, s) \left(2 - r \frac{\alpha_{p_0}(r)}{\gamma(r)} \right) \right] \frac{1}{\mathcal{W}_\ell^+(r) \mathfrak{F}(r) r^2}; \\ G_\ell^{\text{BBreg}}(r, s) &= -\frac{\ell(\ell + 1)}{F_\ell(r)} \left[Q_\ell^+(r, s) + \left(2 - s \frac{\alpha_{p_0}(s)}{\gamma(s)} \right) T_\ell^+(s, r) + \left(2 - r \frac{\alpha_{p_0}(r)}{\gamma(r)} \right) T_\ell^+(r, s) \right. \\ &\quad \left. + \left(2 - r \frac{\alpha_{p_0}(r)}{\gamma(r)} \right) \left(2 - s \frac{\alpha_{p_0}(s)}{\gamma(s)} \right) G_\ell^+(r, s) \right] \frac{1}{\mathcal{W}_\ell^+(s) \mathfrak{F}(s) s^2}. \end{aligned} \quad (5.35)$$

Step 2d. Calculate G_ℓ^{PB} by symmetry, $G_\ell^{\text{PB}}(r, s) = G_\ell^{\text{BP}}(s, r)$.

If needed, we can also compute $G_\ell^+(r, s) = -\frac{G_\ell^+(r, s)}{\mathcal{W}_\ell^+(s)} \frac{F_\ell(s)}{F_0(s)}$.

generic first-order original problem (5.36) uses first-order unknown v (5.20) which is different from that for the conjugate problem stated in (A.17). Secondly, (5.36) is written in the non-conservative form of a 1D convection-diffusion operator, while the first order conjugate problem has no convection term. For these reasons, the implementation of (5.36) will be slightly different from that for the conjugate problem, particularly in the definition of the final HDG problem and thus the elementary matrices of the discretized problem. For a discussion of applying HDG method for convection-diffusion problem in the time-domain, we refer to [23] for 1D spatial domain and [35] for higher dimension.

Section 6]. For an overview of the development of HDG method, we refer to [23].

Mesh and jump notation:

- We introduce a set of nodes,

$$\Sigma = \{r_k \mid 1 \leq k \leq |\Sigma|, r_1 = r_{\min}, r_{|\Sigma|} = r_{\max}\}, \quad (5.37)$$

which partitions the interval $\Omega = [r_{\min}, r_{\max}]$ into a collection \mathcal{T}_h of elements denoted by K^e ,

$$[r_{\min}, r_{\max}] = \bigcup_{e=1}^{|\mathcal{T}_h|} K^e, \quad \mathcal{T}_h = \{K^e, 1 \leq e \leq |\mathcal{T}_h|\}. \quad (5.38)$$

Here, $|\cdot|$ denotes the cardinality of a set. From the above definition, K^e is a connected subinterval in $[r_{\min}, r_{\max}]$,

$$K^e = (r^{(e,1)}, r^{(e,2)}), \quad \partial K^e = \{r^{(e,1)}, r^{(e,2)}\}, \quad \text{with } r^{(e,1)} < r^{(e,2)}. \quad (5.39)$$

We also have

$$|\Sigma| = |\mathcal{T}_h| + 1. \quad (5.40)$$

We denote the interior nodes by

$$\Sigma_{\text{int}} = \{r_k \mid 2 \leq k \leq |\Sigma| - 1\} = \Sigma \setminus \partial\Omega = \Sigma \setminus \{r_1, r_{|\Sigma|}\}. \quad (5.41)$$

- Each node $r \in \Sigma$ is labeled by two systems of indices, the global indices in which a node is written as seen in (5.37), i.e. as,

$$r = r_k, \quad \text{with } 1 \leq k \leq |\Sigma|, \quad (5.42)$$

and the local indices in which it is referred to as,

$$r = r^{(e,\ell)}, \quad \text{with } 1 \leq e \leq |\mathcal{T}_h|, \ell \in \{1, 2\}. \quad (5.43)$$

In the above equation, index e indicates the element K^e to which r belongs and forms one of its boundary, cf. (5.39).

- We denote by β the mapping

$$\beta : \{1, \dots, |\mathcal{T}_h|\} \times \{1, 2\} \longrightarrow \{1, \dots, |\Sigma|\}, \quad \beta(e, \ell) = k, \quad (5.44)$$

which assigns to the local index (e, ℓ) of a node its global index $k = \beta(e, \ell)$, i.e.

$$r^{(e,\ell)} = r^k = r^{\beta(e,\ell)}, \quad k = \beta(e, \ell). \quad (5.45)$$

For $1 \leq e \leq |\Sigma|$, the restriction operator \mathcal{R}^e to element K^e is defined on a vector of length $|\Sigma|$ as, for $V = (v_k)_{1 \leq k \leq |\Sigma|}$,

$$\mathcal{R}^e V = \begin{pmatrix} v^j \\ v^k \end{pmatrix} = \begin{pmatrix} v^{(e,1)} \\ v^{(e,2)} \end{pmatrix}, \quad \text{i.e. } j = \beta(e, 1), k = \beta(e, 2). \quad (5.46)$$

- Our sign convention for the normal vector at the boundary of element K^e is outward,

$$\nu_{\partial K^e}|_{r^{(e,1)}} = \nu^{(e,1)} = -1, \quad \text{and } \nu_{\partial K^e}|_{r^{(e,2)}} = \nu^{(e,2)} = 1. \quad (5.47)$$

We introduce the jump at an interface $\{r\} = \partial K^+ \cap \partial K^-$,

$$\llbracket v \rrbracket_r := \hat{v}^{K^+}(r) \nu^{K^+}(r) + \hat{v}^{K^-}(r) \nu^{K^-}(r). \quad (5.48)$$

In fact, this can be more explicitly written; for index $k = \beta(e, 2) = \beta(e, 1)$, and node $\{r_k\} = \partial K^e \cap \partial K^{e+1}$, the jump of v at r_k is

$$\begin{aligned} \llbracket v \rrbracket_{r_k} &:= v|_{K^e}(r^{(e,2)}) \nu^{(e,2)} + v|_{K^{e+1}}(r^{(e,1)}) \nu^{(e+1,1)} \\ &= v|_{K^e}(r^{(e,2)}) - v|_{K^{e+1}}(r^{(e,1)}). \end{aligned} \quad (5.49)$$

Unknowns in HDG method In HDG method, we distinguish between the value of the (continuous) unknown (u, v) in the interior of an element K^e and on its boundary. They are thus represented by different quantities. Those on the boundary are called the numerical traces.

$$\begin{array}{cccccc} \text{Continuous unknowns} & w|_{K^e}, & v|_{K^e}, & w|_{\partial K^e}, & v|_{\partial K^e} & \\ \text{Approximants} & w_h & v_h & \hat{w} & \hat{v} & \end{array} \quad (5.50)$$

Condition on the numerical traces is obtained from the continuity of the solution,

$$[[\hat{w}]]_r = 0, \quad [[\hat{v}]]_r = 0, \quad \forall r \in \Sigma_{\text{int}}. \quad (5.51)$$

Remark 17. *These conditions are also called conservativity condition. Note that the second condition in (5.51) is different from that in [36, Eqs (7) and (8)], since our equation is in nonconservative form. \diamond*

The primal unknowns in HDG will be the numerical traces. The volume unknowns are determined by local problems, cf. (5.57a), if either the trace of u or w on ∂K^e is given. As a result of this, the primal variables will contain only one or the other. A natural choice is working with Dirichlet local problem, i.e. the trace of w . Specifically, one introduces the Lagrangian unknown λ to represent the numerical trace of w , and that of v is related to λ and the trace of w via a relation containing the HDG stabilization parameter τ ,

$$\hat{w} := \lambda, \quad \hat{v} := v_h + \tau(w_h - \lambda). \quad (5.52)$$

We denote by $\mathcal{P}_k(T)$ the space of complex-valued polynomials of degree at most k defined on the domain T . We define the following piecewise polynomial space on $[r_{\min}, r_{\max}]$,

$$\begin{aligned} W_h(\Omega) &:= \{q \in L^2(\Omega) \mid q|_{K^e} \in \mathcal{P}_k(K^e), 1 \leq e \leq |\mathcal{T}_h|\}, \\ V_h(\Omega) &:= \{q \in L^2(\Omega) \mid q|_{K^e} \in \mathcal{P}_{\tilde{k}}(K^e), 1 \leq e \leq |\mathcal{T}_h|\}. \end{aligned} \quad (5.53)$$

HDG problem Find (w_h, v_h, λ) : that solves

- the local volume problem¹⁶ for all $K \in \mathcal{T}_h$, and test functions $\phi \in W_h(\Omega)$, $\psi \in V_h(\Omega)$,

$$\left\{ \begin{aligned} & \int_K r v'_h \hat{q}_{\text{reg}} \phi \, dr + \int_K q_{\text{reg}} v_h \phi \, dr + \int_K \tilde{q}_{\text{reg}} w_h \phi \, dr \\ & \quad + \sum_{r \in \partial K} \tau^K (w_h - \lambda)|_r (\hat{q}_{\text{reg}} r \phi)|_r \nu^K(r) = \int_K f_{\text{reg}} r^2 f \phi \, dr; \end{aligned} \right. \quad (5.57a)$$

$$\left\{ \begin{aligned} & \int_K v_h \psi \, dr + \int_K w_h (r \psi)' \, dr - \sum_{r \in \partial K} \lambda (r \psi)|_r \nu^K(r) = 0. \end{aligned} \right. \quad (5.57b)$$

- and problems on the nodes Σ ,

$$\left\{ \begin{aligned} & [[v_h + \tau(w_h - \lambda)]]|_r = 0, \quad \text{for } r \in \Sigma_{\text{int}}; \end{aligned} \right. \quad (5.58a)$$

$$\left\{ \begin{aligned} & \mathfrak{B}_L(w_h, v_h, \lambda_h)|_{r_{\min}} = g_L; \quad \mathfrak{B}_R(w_h, v_h, \lambda_h)|_{r_{\max}} = g_R. \end{aligned} \right. \quad (5.58b)$$

¹⁶It suffices to show the transformation of $\int_K \hat{q}_{\text{reg}} r v' \phi \, dr$. First by integrating by parts we obtain,

$$\int_K \hat{q}_{\text{reg}} r v' \phi \, dr = - \int_K v (r \hat{q}_{\text{reg}} \phi)' \, dr + \sum_{r \in \partial K} v (r \hat{q}_{\text{reg}} \phi) \nu(r). \quad (5.54)$$

In the above expression, we next replace the continuous quantities by corresponding numerical ones as shown in (5.50),

$$- \int_K v_h (r \hat{q}_{\text{reg}} \phi)' \, dr + \sum_{r \in \partial K} \hat{v} (r \hat{q}_{\text{reg}} \phi) \nu(r). \quad (5.55)$$

Replace the numerical trace \hat{v} by (5.52), and do a integration by parts,

$$\begin{aligned} & - \int_K v_h (r \hat{q}_{\text{reg}} \phi)' \, dr + \sum_{r \in \partial K} (v_h + \tau(w_h - \lambda)) (r \hat{q}_{\text{reg}} \phi) \nu(r) \\ & = \int_K (v_h)' r \hat{q}_{\text{reg}} \phi \, dr + \sum_{r \in \partial K} \tau (w_h - \lambda) (r \hat{q}_{\text{reg}} \phi) \nu(r). \end{aligned} \quad (5.56)$$

HDG discrete unknowns The discrete unknowns contain the coefficients of w_h, v_h, λ with respect to a chosen basis. Since we are in dimension one, λ is already a collection of scalar values, it suffices to specify the basis for w_h, v_h . In particular, with the basis functions for $\mathcal{P}_k(K^e)$ denoted by ψ_l^e , and for $\mathcal{P}_k(K^e)$ by ϕ_l^e , we write

$$w_h|_{K^e} = \sum_{k=1}^{n_e} W_k^e \phi_l^e, \quad v_h|_{K^e} = \sum_{k=1}^{m_e} V_k^e \psi_l^e. \quad (5.59)$$

The unknowns of the discrete problems are

$$\mathbf{U}^e = ((W_k^e)_{1 \leq k \leq n_e}^t, (V_k^e)_{1 \leq k \leq m_e}^t), \quad \Lambda = (\lambda^{(1)}, \dots, \lambda^{(|\Sigma|)})^t. \quad (5.60)$$

A summary of the dimension of the discretized problem is given in Table 3.

Table 3: Dimensions of discretization.

$\hat{n} = \Sigma $	number of edges = length of global unknown
$ \mathcal{T}_h = \Sigma - 1$	number of elements
n_e	dimension of set of basis functions $\{\phi_j^e, 1 \leq j \leq n_e\}$ for $\mathcal{P}_k(K^e)$
m_e	dimension of set of basis functions $\{\psi_j^e, 1 \leq j \leq m_e\}$ for $\mathcal{P}_k(K^e)$

Discretized HDG problems : Find $((\mathbf{U}^e)_{1 \leq e \leq |\mathcal{T}_h|}, \Lambda)$ which solves

$$\begin{cases} \mathbb{A}^e \mathbf{U}^e + \mathbb{C}^e \mathcal{R}_e \Lambda = \begin{pmatrix} \mathbf{F}^e \\ \mathbf{0}_{1 \times m_e} \end{pmatrix}, & \text{for } 1 \leq e \leq |\mathcal{T}_h|; \\ \sum_{e=1}^{|\mathcal{T}_h|} \mathcal{R}_e^t (\mathbb{B}^e \mathbf{U}^e + \mathbb{L}^e \mathcal{R}_e \Lambda) = \sum_{e=1}^{|\mathcal{T}_h|} \mathcal{R}_e^t \mathbf{s}^e. \end{cases} \quad (5.61a)$$

$$\quad (5.61b)$$

Here the restriction operator \mathcal{R}_e is defined in (5.46). We list below the definition of the matrices.

– The matrices of the local problem (5.61a)

$$\mathbf{F}_k^e = \int_{K^e} r^2 f_{\text{reg}} f \phi_k; \quad \mathbb{A}^e := \begin{pmatrix} \mathbb{Q}^e + \tau^e \mathbb{R}^e & \mathbb{T}^e \\ \mathbb{S}^k & \mathbb{M}^e \end{pmatrix}, \quad (5.62)$$

with component matrices

$$\begin{aligned} \mathbb{Q}_{kl}^e &= \int_{K^e} \tilde{q}_{\text{reg}} \phi_k \phi_l; & \mathbb{S}_{kl}^K &= \int_{K^e} \phi_k (\psi_l + r \psi_l'); \\ \mathbb{T}_{kl}^e &= \int_{K^e} (r \psi_k' \hat{q}_{\text{reg}} + q_{\text{reg}} \psi_k) \phi_l; & \mathbb{M}_{kl}^K &= \int_{K^e} \psi_k \psi_l; \\ \mathbb{R}^e &= -\hat{q}_{\text{reg}}(\mathbf{r}^{(e,1)}) \mathbf{r}^{(e,1)} \mathbb{E}_{11} + \hat{q}_{\text{reg}}(\mathbf{r}^{(e,2)}) \mathbf{r}^{(e,2)} \mathbb{E}_{n_e n_e}. \end{aligned} \quad (5.63)$$

and

$$\mathbb{C}^K = \begin{pmatrix} \tau^e \hat{q}_{\text{reg}}(\mathbf{r}^{(e,1)}) \mathbf{r}^{(e,1)} \mathbf{e}_1 & -\tau^e \hat{q}_{\text{reg}}(\mathbf{r}^{(e,2)}) \mathbf{r}^{(e,2)} \mathbf{e}_{n_e} \\ \mathbf{r}^{(e,1)} \mathbf{e}_1 & -\mathbf{r}^{(e,2)} \mathbf{e}_{m_e} \end{pmatrix}. \quad (5.64)$$

In the above equation, $\mathbf{e}_i, \mathbf{e}_i$ are the elementary row and column unit vectors respectively.

– The matrices of the global discrete problem (5.61b) are

$$\mathbb{B}^e = \begin{pmatrix} \mathbb{F}^{(e,1)} & \mathbb{Q}^{(e,2)} \\ \mathbb{F}^{(e,2)} & \mathbb{Q}^{(e,2)} \end{pmatrix}, \quad \mathbb{L}^e = \begin{pmatrix} L_1^e & 0 \\ 0 & L_2^e \end{pmatrix}, \quad \mathbf{s}^e = \begin{pmatrix} \mathbf{s}^{(e,1)} \\ \mathbf{s}^{(e,2)} \end{pmatrix}, \quad (5.65)$$

with components given by

$\mathbf{r}^{(e,i)} \in$	$\mathbb{F}^{(e,i)}$	$\mathcal{Q}^{(e,i)}$	L_i^e	$\mathbf{s}^{(e,i)}$	i
Σ_{int}	$-\tau^e \mathbf{e}_1$	$-\mathbf{e}_1$	τ^e	0	$i = 1$
	$\tau^e \mathbf{e}_{n_e}$	\mathbf{e}_{m_e}	$-\tau^e$	0	$i = 2$
Σ_a	$\frac{\mathcal{J}_\ell(r^{(e,2)})}{r^{(e,2)}} \tau^e \mathbf{e}_{n_e}$	$\frac{\mathcal{J}_\ell(r^{(e,2)})}{r^{(e,2)}} \mathbf{e}_{m_e}$	$-i\mathcal{N}(r^{(e,2)}) - \tau^e \frac{\mathcal{J}_\ell(r^{(e,2)})}{r^{(e,2)}}$	g_a	$i = 2$
Σ_d	0	0	1	g_{Ld}	$i = 1$
	0	0	1	g_{Rd}	$i = 2$
Σ_{dv}	$-\tau^e \mathbf{e}_1$	$-\mathbf{e}_1$	τ^e	g_{dv}	$i = 1$

(5.66)

Recall that Σ_{int} is the interior nodes (5.41), while Σ_\bullet for $\bullet = a, d, \text{dv}$ indicate the type of the boundary condition imposed at a boundary node.

6 Radiation boundary condition coefficients

In this section, we construct the coefficient \mathcal{Z} of the radiation boundary condition (5.4),

$$\partial_n u = i\mathcal{Z}(r)u, \quad \text{at } r = r_{\text{max}},$$

employed to approximate the physical solution. We also recall that (5.4) is the RBC associated with the conjugated modal operator \mathcal{L}_ℓ , while RBC (5.10) is for the operator \mathcal{L}_ℓ . There are three main groups of RBC coefficients. The nonlocal one obtained from factorizing the operator \mathcal{L}_ℓ , which formally is

$$\mathcal{L}_\ell = \left(\partial_r - \sqrt{V_\ell} \right) \left(\partial_r + \sqrt{V_\ell} \right) + \text{regularizing term}, \quad (6.1)$$

and the nonlocal coefficient $\mathcal{Z}_{\text{NL}}^\ell$ is given by $\sqrt{V_\ell}$. Its explicit form is given in (6.12). The remaining coefficients are approximation of the nonlocal coefficient $\mathcal{Z}_{\text{NL}}^\ell$ in two categories. The first category includes the high-frequency (HF) coefficients, and comes from approximations obtained by taking $k_a \rightarrow \infty$, as well as the small-angle-incident (SAI) family. For the HF family, the RBC coefficients are polynomials in k_a , cf. (6.19). The derivation of the high-frequency group is standard following [2] and [7, Section 6] for the scalar operator $\mathcal{L}_{\text{scalar}}$ (3.42). A second category is obtained by replacing V_ℓ inside the square root of the nonlocal coefficients by its approximation. For this purpose, approximation of V_ℓ will be discussed in Subsection 6.1. The coefficients related to this category include the approximate Whittaker family in (6.14), those from the long-range potential (6.15)–(6.17), and those from approximation of V_ℓ for large r cf. (6.18).

We note here two differences with the scalar equation (3.42) considered in [7, 8, 3].

- The conjugated modal operator $\mathbb{L}_\ell^{\text{scalar}}$ (3.43) of $\mathcal{L}_{\text{scalar}}$ is a Whittaker operator for $r \geq r_a$, and thus allows for analytic expressions of solutions in this region and exact Dirichlet-to-Neumann map, cf. [7, 8, 3]. To remedy the lack of analytical expression for solutions in the atmosphere in the case of vector equation, for purpose of preliminary analysis, a reference solution can be obtained, when there is attenuation, by placing a zero Dirichlet condition very high up in the atmosphere, i.e. at $r = r_{\text{max}}$ for $r_{\text{max}} \gg 1$. This technique was employed in [2].
- In addition to the classical high-frequency family obtained in the same manner for $\mathbb{L}_\ell^{\text{scalar}}$, there is a new high-frequency family which include additionally a term coming from the influence of gravity, cf. (6.19). We will see in the numerical experiments of Section 7 that the inclusion of this term will improve the precision by three orders of magnitude in most cases, see Subsection 7.3. The coefficients containing this term are distinguished by the letter ‘G’ in the suffix labeling the conditions \mathcal{Z} .

6.1 Approximation of V_ℓ in the atmosphere

We obtain approximations of V_ℓ as $r \rightarrow \infty$. In addition to the variant already obtained in [6, Proposition 10], we compute another one called a *Whittaker variant*. As mentioned above, in previous works [7, 8, 3] for the scalar operator $\mathbb{L}_\ell^{\text{scalar}}$, the potential V_ℓ^{scalar} in the atmosphere is indeed a Whittaker potential,

which means that a basis for the outgoing solution family is given by the Whittaker function W and explicit expression for the D-t-N operator is obtained in terms of this special function, cf. [3, Equation 2.38]. With the vector wave problem, while V_ℓ is not of Whittaker type, we can hope to approximate its outgoing solution by a Whittaker function if it is not too far from one. The RBC coefficients related to this are given in (6.14), and thus resemble the analytic D-t-N coefficient of L_ℓ^{scalar} .

We first recall the approximation obtained in [6, Proposition 6]. Define the index μ_ℓ such that

$$\mu_0^2 - \frac{1}{4} = 2, \quad \mu_\ell^2 - \frac{1}{4} = 2 + \ell(\ell+1) + \frac{\ell(\ell+1)\alpha_a}{k_a^2} \left(\frac{\alpha_a}{\gamma_a} - \alpha_a \right), \quad \ell > 0, \quad (6.2)$$

and potential

$$Q_\ell^G(r) = k_a^2 + \frac{\eta_a}{r} - \frac{\mu_\ell^2 - \frac{1}{4}}{r^2} + R_\odot^2 \frac{2G\mathbf{m}}{c_a^2 r^3}. \quad (6.3)$$

From [6, Proposition 9],

$$V_0(r) = -Q_0^G + \text{a.e.d.t}; \quad (6.4a)$$

$$V_\ell(r) = -Q_\ell^G + \frac{\ell(\ell+1)}{\Gamma_a^2} O(r^{-3}) + \frac{[\ell(\ell+1)]^2}{(\Gamma_a \omega)^2} O(r^{-6}), \quad \ell > 0. \quad (6.4b)$$

Numerical experiments We have provided an approximation for the potential in the atmosphere in Subsection 6.1. To evaluate its accuracy, we picture in Figure 6 the potential and the approximation Q_ℓ^G given in (6.3), for different modes and frequencies with an attenuation of 20 μ Hz. We see that, except for low frequencies, it is not possible to visually see the difference between V_ℓ and its approximation Q_ℓ^G . In Figures 6g and 6h, we show the relative error ϵ_{rel} given by

$$\epsilon_{\text{rel}}(r) = \frac{|V_\ell(r) - Q_\ell^G(r)|}{|V_\ell(r)|}. \quad (6.5)$$

We see that the relative error decreases with frequency and increases with the mode. Therefore, the case of low-frequency and high modes bears the most error. Here, using mode $\ell = 20$ and 7mHz shows an error of magnitude 10^{-10} while using $\ell = 750$ and 0.2mHz gives an error of magnitude 10^{-1} . We also observe that the error decreases only slightly with r and remains relatively constant for $r \in (4, 6)$.

Approximations in form of Whittaker equation We revisit the form (3.40) of V_ℓ ,

$$V_\ell = -k^2 + \frac{\phi_0''}{c_0^2} - \frac{\eta}{r} + \frac{\nu_\ell^2 - \frac{1}{4}}{r^2}, \quad \nu_\ell \text{ defined in (3.41)}.$$

Due to its decay of order r^{-3} and independence of ℓ , we can absorb the term $\frac{\phi_0''}{c_0^2}$ into any of the term $-k^2$, $\frac{\eta}{r}$, and $\frac{\nu_\ell^2 - 1/4}{r^2}$ and define new functions from old ones by adding this factor,

$$\begin{aligned} k_G^2 &:= k^2 - \frac{\phi_0''}{c_0^2}, & \eta_G(r) &:= \eta(r) - r \frac{\phi_0''(r)}{c_0^2(r)}, \\ [\nu_\ell^G(r)]^2 &= [\nu_\ell(r)]^2 + r^2 \frac{\phi_0''}{c_0^2}. \end{aligned} \quad (6.6)$$

Then V_ℓ can be written as

$$V_\ell = -k^2 - \frac{\eta_G}{r} + \frac{\nu_\ell^2 - \frac{1}{4}}{r^2} = -k_G^2 - \frac{\eta}{r} + \frac{\nu_\ell^2 - \frac{1}{4}}{r^2} = -k^2 - \frac{\eta}{r} + \frac{(\nu_\ell^G)^2 - \frac{1}{4}}{r^2}. \quad (6.7)$$

The above expressions (6.7) have the properties that: k_\bullet^2 , η_\bullet , and ν_\bullet^2 are continuous and bounded on $[0, \infty)$ for $\Gamma > 0$, k_\bullet^2 and η_\bullet are independent of ℓ , and limit of k_\bullet^2 as $r \rightarrow \infty$ is k_a^2 . We also note that due to (3.71), μ_ℓ in (6.2) is the limiting value of $\nu_\ell^G(r)$,

$$\lim_{r \rightarrow \infty} \nu_\ell^G(r) = \mu_\ell. \quad (6.8)$$

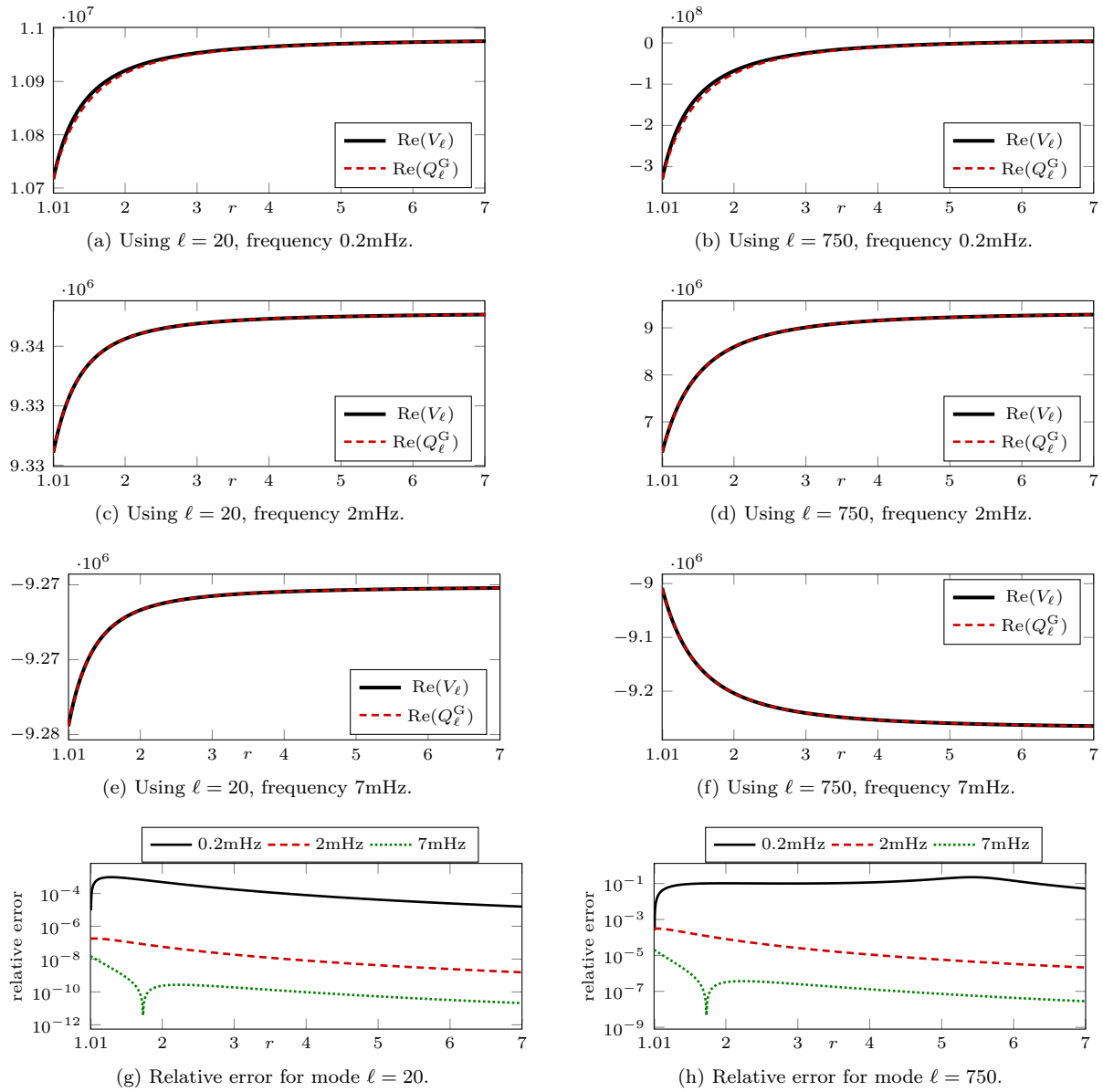


Figure 6: Comparisons of the potential V_ℓ and its approximation Q_ℓ^G given in (6.3). The relative error ϵ_{rel} is computed by (6.5). In the computations, the attenuation is set to $\Gamma/(2\pi) = 20\mu\text{Hz}$.

The expressions in (6.7) are interesting for the reason that on a small neighborhood of a position $r \geq r_a$, if we approximate the function k_\bullet^2 , η_\bullet and ν_\bullet by constants, then V_ℓ is the potential of the Whittaker operator. With three choices of constants,

$$\begin{array}{ccc} & k_\star & \eta_\star & \nu_\ell \\ \hline Q_\ell^{\text{W1}} & k(r) & \eta_G(r) & \nu_\ell(r) \end{array} \quad (6.9a)$$

$$\begin{array}{ccc} & k_\star & \eta_\star & \nu_\ell \\ \hline Q_\ell^{\text{W2}} & k_G(r) & \eta(r) & \nu_\ell(r) \end{array} \quad (6.9b)$$

$$\begin{array}{ccc} & k_\star & \eta_\star & \nu_\ell \\ \hline Q_\ell^{\text{W3}} = Q_\ell^G & k(r) & \eta(r) & \nu_\ell^G(r) \end{array} \quad (6.9c)$$

then V_ℓ is approximated

$$V_\ell(r)|_{(r-\epsilon, r+\epsilon)} = \underbrace{-k_\star^2 - \frac{\eta_\star}{r} - \frac{\nu_\ell^2 - \frac{1}{4}}{r^2}}_{-Q_\ell^{W,i}(r)} + \mathcal{O}(\epsilon). \quad (6.10)$$

The solutions of $(-\partial_r^2 + V_\ell)w = 0$ can then be approximated by Whittaker functions on $(r - \epsilon, r + \epsilon)$. In particular, an outgoing solution can be approximated by the Whittaker function W ,

$$w|_{(r-\epsilon, r+\epsilon)} \sim W_{-\chi, \nu_\ell}(-2i k_\star r), \quad \text{with } \chi = -i \frac{\eta_\star}{2k_\star}. \quad (6.11)$$

Corresponding η_\star and k_\star are listed in (6.9).

6.2 List of Radiation boundary conditions

1. Nonlocal condition: subscript NL stands for nonlocal coefficient, we have

$$\mathcal{Z}_{\text{NL}}^\ell(r) := i\sqrt{-V_\ell(r)} = i k_a \left(\frac{-V_\ell(r)}{k_a^2} \right)^{1/2}. \quad (6.12)$$

2. Approximate Whittaker coefficients are approximation of the nonlocal coefficient $\mathcal{Z}_{\text{NL}}^\ell$ in the form of Whittaker functions (specifically (6.10) or (6.4)). They arise from approximations discussed in Subsection 6.1 of V_ℓ by Bessel-type operator. Associated with constant (k, η, ν_ℓ) define (generic) coefficient,

$$\mathcal{Z}_{\text{aW}}^\ell(r) = -2i k(r) \frac{W'_{-\chi(r), \nu_\ell(r)}(-2i k(r) r)}{W_{-\chi(r), \nu_\ell(r)}(-2i k(r) r)}, \quad (6.13)$$

with $\chi(r) := i \frac{(-\eta(r))}{2k(r)}$.

We then use formula (6.13) associated with the following four choices of (k, η, ν_ℓ) to define the approximate Whittaker (aW) RBC coefficients at r ,

aW RBC coefficient at r	Define using (6.13) with			Approximation of V_ℓ
$\mathcal{Z}_{\text{aW-1}}^\ell$	$k(r)$	$\eta^G(r)$	$\nu_\ell(r)$	(6.10) with (6.9a)
$\mathcal{Z}_{\text{aW-2}}^\ell$	$k_G(r)$	$\eta(r)$	$\nu_\ell(r)$	(6.10) with (6.9b)
$\mathcal{Z}_{\text{aW-3}}^\ell$	$k(r)$	$\eta(r)$	$\nu_\ell^G(r)$	(6.10) with (6.9c)
$\mathcal{Z}_{\text{aW-4}}^\ell$	k_a	η_a	μ_ℓ (6.2)	(6.4)

(6.14)

3. Approximate nonlocal family is obtained by replacing V_ℓ in the defining expression (6.12) of the nonlocal coefficient by an approximation of V_ℓ , which captures to the highest order as $r \rightarrow \infty$. We divide this family further into the long-range approximate nonlocal family and those obtained with approximation (6.4).

- (a) To define coefficients in this family, we replace V_ℓ in (6.12) by $k^2 - V_{\text{longrange}}$. This is inspired by the fact that the oscillatory behavior of the solution as $r \rightarrow \infty$ is characterized by the solution of the eikonal equation (3.76), which involves only the energy level and the long range part of the potential. Recall that a choice of long-range part is \mathcal{V} (3.69). Since we work with $r \geq r_a$, in the definition of \mathcal{V} in (3.69), we can work directly with factor $\frac{\eta}{r}$ instead of $\frac{\eta}{r+1}$. In this way, we define

$$\mathcal{Z}_{\text{G-LR}} = i\sqrt{k^2(r) - \frac{\phi_0''(r)}{c_0^2(r)} + \frac{\eta(r)}{r}} = i k_a \left(1 - \frac{\phi_0''(r)}{(k_a c_0(r))^2} + \frac{\eta(r)}{(k_a)^2(r)} \right)^{1/2}. \quad (6.15)$$

The subscript LR stands for long range, and G denotes the inclusion of the term with gravitational potential. We can add to this potential any long-range term that is independent of ℓ and continuous (only needed on $r \geq r_a$).

$$\tilde{\mathcal{Z}}_{G-LR} = i\sqrt{k^2(r) - \frac{\phi_0''(r)}{c_0^2(r)} + \frac{\eta(r)}{r} - \frac{2}{r^2}}. \quad (6.16)$$

In this way, we can remove the contribution of the term with the gravitational potential ϕ_0 from the above coefficients, since it is of order r^{-2} , introducing

$$\mathcal{Z}_{LR} = i\sqrt{k^2(r) + \frac{\eta(r)}{r}} = ik_a \left(1 + \frac{\eta(r)}{(k_a r)^2}\right)^{1/2}; \quad (6.17a)$$

$$\tilde{\mathcal{Z}}_{LR} = i\sqrt{k^2(r) + \frac{\eta(r)}{r} - \frac{2}{r^2}}. \quad (6.17b)$$

- (b) The second subfamily written with subscript aNL arise from approximation (6.4) of V_ℓ by potentials¹⁷ Q_ℓ and Q_ℓ^G ,

$$\mathcal{Z}_{aNL-G}^\ell = i\sqrt{Q_\ell^G} = ik_a \left(1 + \frac{\eta_a}{k_a} \frac{1}{k_a r} + \frac{\frac{1}{4} - \mu_\ell^2}{(k_a r)^2} + 2\frac{Gm}{c_0^2} \frac{1}{(k_a r)^2 r}\right)^{1/2}; \quad (6.18a)$$

$$\mathcal{Z}_{aNL}^\ell = i\sqrt{Q_\ell} = ik_a \left(1 + \frac{\eta_a}{k_a} \frac{1}{k_a r} + \frac{\frac{1}{4} - \mu_\ell^2}{(k_a r)^2}\right)^{1/2}. \quad (6.18b)$$

4. We introduce the HF family enriched with the gravity term, obtained as approximations of the nonlocal coefficient as $k_a \rightarrow \infty$,

$$\mathcal{Z}_{S-HFG-0} = ik_a \left(1 + \frac{Gm}{c_0^2} \frac{1}{(k_a r)^2 r}\right), \quad (6.19a)$$

$$\mathcal{Z}_{S-HFG-1} = ik_a \left(1 + \frac{1}{2k_a^2} \frac{\eta_a}{r} + \frac{Gm}{c_0^2} \frac{1}{(k_a r)^2 r}\right), \quad (6.19b)$$

$$\mathcal{Z}_{S-HFG-2}^\ell = ik_a \left(1 + \frac{1}{2k_a^2} \left(\frac{\eta_a}{r} + \frac{\frac{1}{4} - \mu_\ell^2}{r^2}\right) + \frac{Gm}{c_0^2} \frac{1}{(k_a r)^2 r}\right), \quad (6.19c)$$

$$\mathcal{Z}_{S-HFG-3}^\ell = ik_a \left(1 + \frac{1}{2k_a^2} \left(\frac{\eta_a}{r} + \frac{\frac{1}{4} - \mu_\ell^2}{r^2} - \frac{1}{8k_a^2} \frac{\eta_a^2}{r^2}\right) + \frac{Gm}{c_0^2} \frac{1}{(k_a r)^2 r}\right). \quad (6.19d)$$

When $G = 0$, we retrieve the usual HF family

$$\mathcal{Z}_{S-HF-i} = \mathcal{Z}_{S-HFG-i}|_{G=0}, \quad i = 0, 1, 2, 3. \quad (6.20)$$

5. For completeness of the discussion, we also include three conditions in the SAI (Small Angle of Incidence) family obtained in the same technique introduced in [2, section 3.3] (see also [7, section 6.3]),

$$\mathcal{Z}_{SAI-0} = ik_a \left(1 + \frac{\eta_a}{r} \frac{1}{k_a^2}\right)^{1/2}, \quad (6.21a)$$

$$\mathcal{Z}_{SAI-1}^\ell = ik_a \left(1 + \frac{\eta_a}{r} \frac{1}{k_a^2}\right)^{1/2} \left(1 + \frac{1}{2k_a^2 r^2} \frac{\frac{1}{4} - \mu_\ell^2}{1 + \frac{\eta_a}{r} \frac{1}{k_a^2}}\right), \quad (6.21b)$$

$$\mathcal{Z}_{SAI-2}^\ell = ik_a \left(1 + \frac{\eta_a}{r} \frac{1}{k_a^2}\right)^{1/2} \left(1 + \frac{1}{2k_a^2 r^2} \frac{\frac{1}{4} - \mu_\ell^2}{1 + \frac{\eta_a}{r} \frac{1}{k_a^2}} - \frac{1}{8k_a^4 r^2} \left(\frac{\frac{1}{4} - \mu_\ell^2}{1 + \frac{\eta_a}{r} \frac{1}{k_a^2}}\right)^2\right). \quad (6.21c)$$

¹⁷We recall from (6.3) potentials $Q_\ell := k_a^2 + \frac{\eta_a}{r} - \frac{\mu_\ell^2 - \frac{1}{4}}{r^2}$ and $Q_\ell^G = Q_\ell + \frac{2}{r^3} \frac{Gm}{(c_a/R_\odot)^2}$.

6. The following coefficients are related to coefficients in the SAI family and are obtained by setting $\ell = 0$ in $\mathcal{Z}_{\text{aNL-G}}^\ell$ and $\mathcal{Z}_{\text{aNL}}^\ell$,

$$\mathcal{Z}_{\text{aNL-G}}^0 = i k_a \left(1 + \frac{\eta_a}{r} \frac{1}{k_a^2} + \frac{2Gm}{c_0^2} \frac{1}{(k_a r)^2 r} \right)^{1/2}, \quad (6.22a)$$

$$\mathcal{Z}_{\text{S-G}} = i k_a \left(1 + \frac{2Gm}{c_0^2} \frac{1}{(k_a r)^2 r} \right)^{1/2}. \quad (6.22b)$$

7 Numerical experiments using solar background models

In this section, we perform numerical experiments using the solar background model S-AtmoI of [22]. We first illustrate the corresponding potentials in Subsection 7.1 and their different structures depending on the frequency and mode. We then compare the numerical behaviour when solving the original or conjugated modal problem in Subsection 7.2. In Subsection 7.3, we investigate the efficiency of the radiation conditions. We compute the Green's kernel in Subsection 7.4 and picture solutions at multiple frequencies and modes in Subsection 7.5. All of the subsequent simulations have been performed using the open-source software `hawen`¹⁸, see [21].

These numerical illustrations and experiments aim to illustrate the following features.

1. We highlight the difference between the potential V_ℓ from the vector modal operator and the scalar modal one V_ℓ^{scalar} , especially the differences brought out due to the inclusion of gravity effects. This will be first illustrated in terms of sign variation in the maps of the potentials. We observe the emergence of new (propagative) regions in the vector case compared to the scalar one: firstly a region at low frequencies in the interior of the Sun ($r \leq 1$) for all modes ℓ , which explains the gravity waves. Secondly, propagative regions appear with the vector-wave potential in the atmosphere for low frequencies and high modes.
2. The new propagative regions in the atmosphere have repercussion on how the RBCs are implemented, particularly in terms of the position of the artificial boundary. In this case, the potential V_ℓ has the profile of a well instead of a horizontal asymptote, i.e., intuitively it is still evolving in a region right above the surface instead of leveling and entering in the infinity asymptotic region. This behavior diverges from what is normally observed for V_ℓ^{scalar} at all frequencies and modes. The same observations hold for V_ℓ at small modes for all frequencies, and at high modes for high frequencies. On the one hand, the behavior of solution associated with V_ℓ^{scalar} is distinguished by the atmospheric cut-off frequency ω_t . On the other hand, for V_ℓ at large ℓ , we will see a new demarcation given by the Lamb frequency S_ℓ . Following this feature and the inclusion of the gravity, we investigate new families of RBC coefficients. In particular, with the emerging new propagative region, the artificial boundary has to be placed sufficiently high up in the atmosphere to capture the correct behaviour.
3. We compare the numerical efficiency of solving the original equation or the conjugated one. We highlight that for low level of attenuation, simulations using the conjugated problem must use a mesh refinement at r^* to capture the correct solutions while, in the case without attenuation, the conjugated problem fails in terms of accuracy. On the other hand, solving the original equation is robust in all configurations, i.e., even in the case without attenuation.
4. The numerical tests show how the assemblage method given in Algorithm 1 is implemented to compute all of the coefficients of the 3D Green's kernel in the vector spherical expansion, i.e., $G_{\ell,\omega}^{\text{PP}}$, $G_{\ell,\omega}^{\text{PB}}$ and $G_{\ell,\omega}^{\text{BB}}$ ¹⁹, with P denoting the radial direction \mathbf{e}_r and B the horizontal direction given by $\nabla_{\mathbb{S}^2} Y_\ell^m$.

A summary of the numerical results is given in Subsection 7.6.

¹⁸<https://ffaucher.gitlab.io/hawen-website/>

¹⁹Each modal kernel is a function of (ω, ℓ, r, s) with position of receiver r and source s . For lightness of notation, we only write $G_{\ell}^{\bullet\bullet}$ or $G_{\ell}^{\bullet\bullet}(r, s)$, without indicating the dependence on ω .

7.1 Maps of the solar potentials

In Figure 7, we provide 2D maps of the real part of the potential V_ℓ for two selected modes, $\ell = 20$ and $\ell = 750$, with attenuation $\Gamma/(2\pi) = 20\mu\text{Hz}$, i.e. plot V_{20} and V_{750} as a function of $(\omega, r) \mapsto V_\ell(\omega, r)$. In these figures, we superimpose the Lamb frequency S_ℓ and the real part of Brunt-Väisälä frequency N as functions of r ,

$$r \mapsto S_\ell(r), \quad r \mapsto \text{Re} N(r). \quad (7.1)$$

We note that the 1D parametrizations $r \mapsto S_\ell(r)$ and $\omega \mapsto r^*(\omega)$ are defining the same curves in Figure 7. The two frequencies S_ℓ and N are fundamental to characterize the potential which can be approximated by

$$V_\ell^{\text{approx}} = -\frac{(\sigma^2 - N^2)(\sigma^2 - S_\ell^2)}{\sigma^2 c_0^2}, \quad (7.2)$$

as shown in [18]. The approximate potential is represented in Figures 7 and 10, and is valid far away from the surface and the location of r^* .

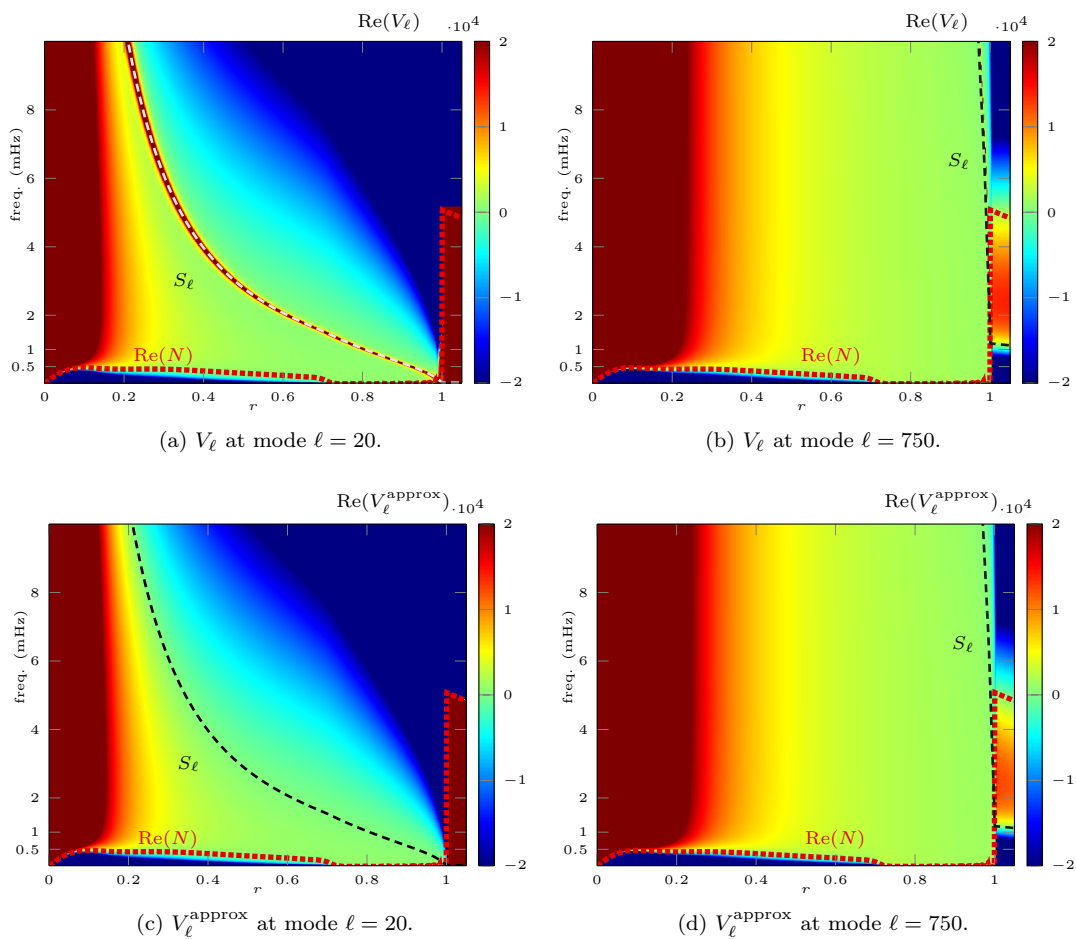
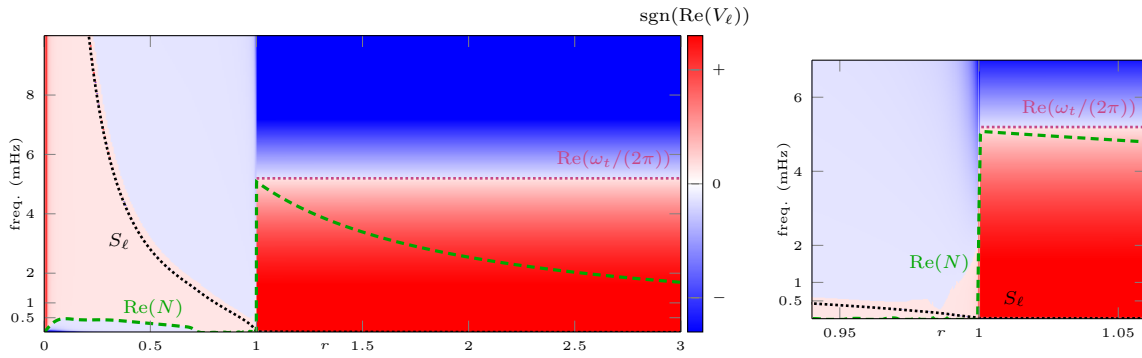


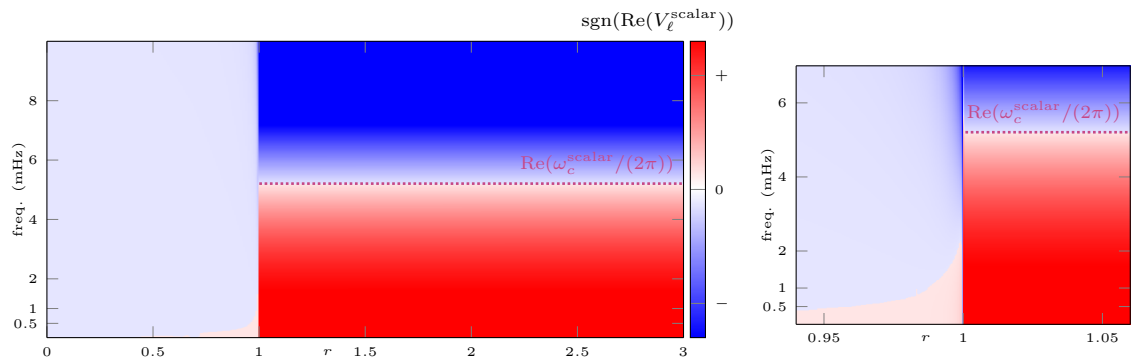
Figure 7: Real part of the potential V_ℓ of (3.34b) and V_ℓ^{approx} of (7.2) for the solar model S-AtmoI with attenuation $\Gamma/(2\pi) = 20\mu\text{Hz}$. The position of the Brunt-Väisälä and Lamb frequencies, (2.20) and (2.21), are pictured with dashed lines.

Since the sign of potential V_ℓ is an indicator of the properties of the solution, in particular solutions are propagative when $V_\ell < 0$ while evanescent for $V_\ell > 0$, we provide a better visualization of the sign of the potentials, in Figures 8 to 10, respectively for modes $\ell = 20$ and $\ell = 750$. In these figures, the region on which $V_\ell > 0$ is colored in red, and those on which $V_\ell < 0$ are blue. For purpose of comparison, the 2D plots of the potential of the scalar operator V_ℓ^{scalar} of (3.44), cf. [8] are also given. In each of the pictures, r varies from 0 to 3, and we also detail the pattern of three frequencies: 0.20mHz, 3mHz, and

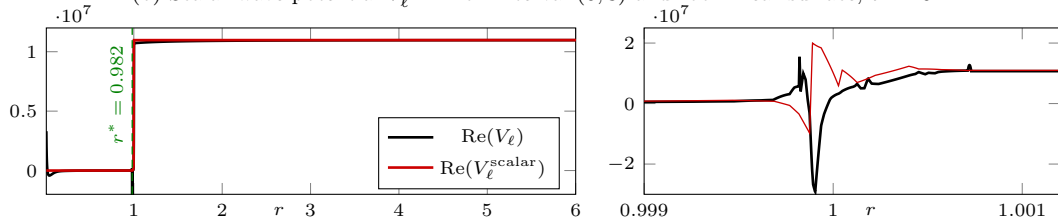
7mHz. The cut-off frequencies ω_t associated to the vector and the scalar problems are given in (3.38) and (3.46).



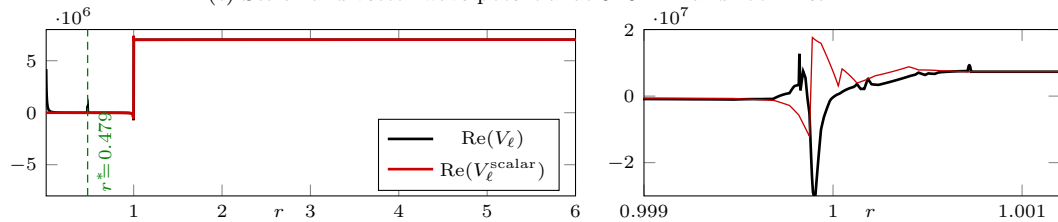
(a) Vector-wave potential V_ℓ on interval $(0, 3)$ and zoom near surface, $\ell = 20$.



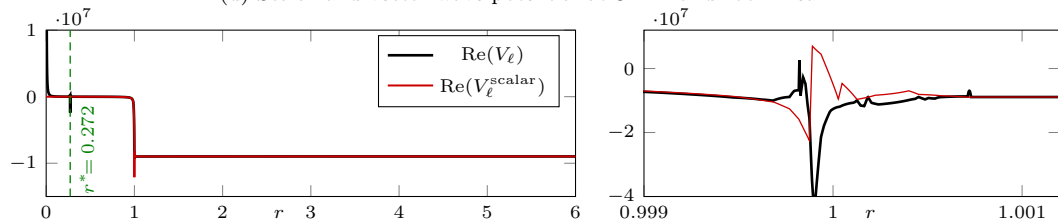
(b) Scalar-wave potential V_ℓ^{scalar} on interval $(0, 3)$ and zoom near surface, $\ell = 20$.



(c) Scalar and vector-wave potential at 0.20mHz and zoom near 1.

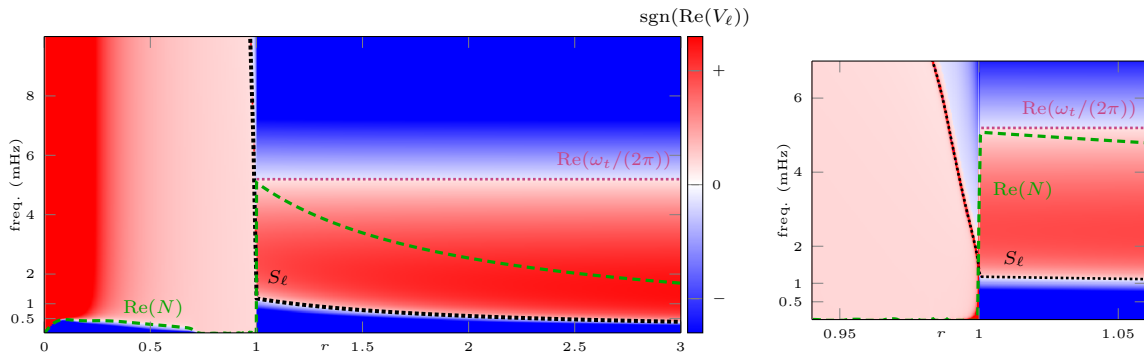
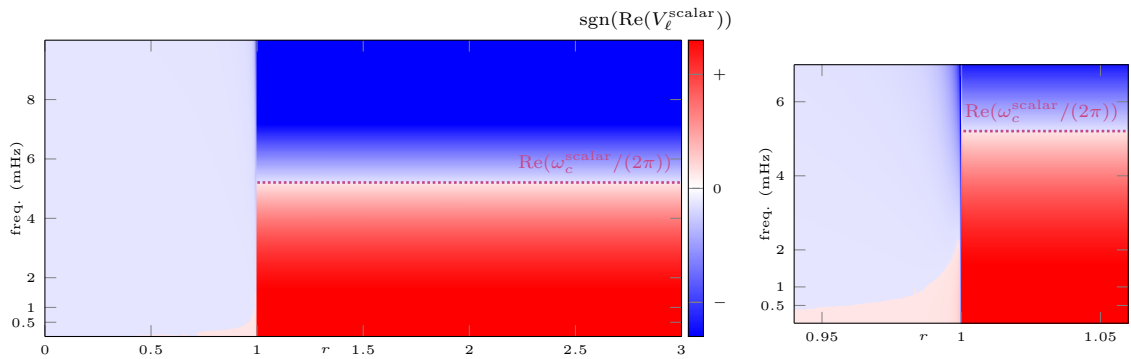
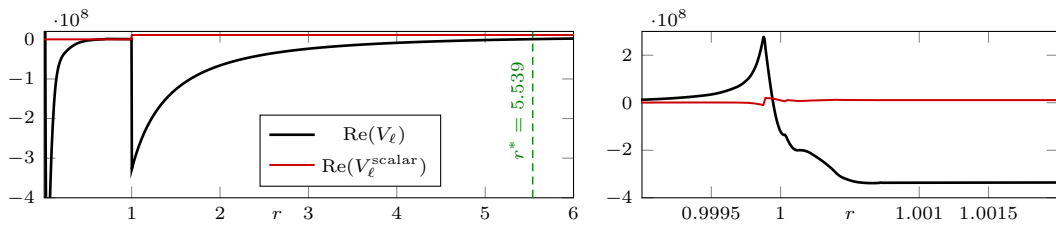


(d) Scalar and vector-wave potential at 3mHz and zoom near 1.

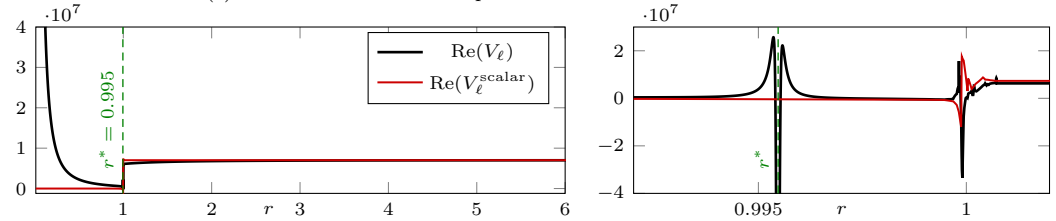


(e) Scalar and vector-wave potential at 7mHz and zoom near 1.

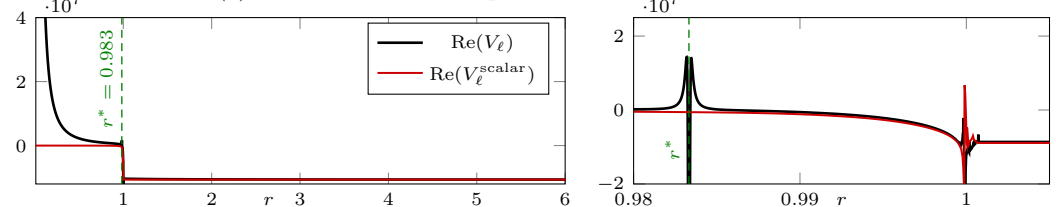
Figure 8: Comparisons of the vector potential V_ℓ , (3.34b), and the scalar potential V_ℓ^{scalar} of (3.44) for mode $\ell = 20$ using attenuation $\Gamma/(2\pi) = 20\mu\text{Hz}$. In the atmosphere, $\omega_t/(2\pi) = 5.19\text{mHz}$ and $\omega_c^{\text{scalar}}(r=5)/(2\pi) = 5.20\text{mHz}$.


 (a) Vector-wave potential V_ℓ on interval $(0, 3)$ and zoom near surface, $\ell = 750$.

 (b) Scalar-wave potential V_ℓ^{scalar} on interval $(0, 3)$ and zoom near surface, $\ell = 750$.


(c) Scalar and vector-wave potential at 0.20mHz and zoom near 1.



(d) Scalar and vector-wave potential at 3mHz, and zoom near 1.



(e) Scalar and vector-wave potential at 7mHz and zoom near 1.

Figure 9: Comparisons of the vector potential V_ℓ , (3.34b), and the scalar potential V_ℓ^{scalar} of (3.44) for mode $\ell = 750$ using attenuation $\Gamma/(2\pi) = 20\mu\text{Hz}$. In the atmosphere, $\omega_t/(2\pi) = 5.19\text{mHz}$ and $\omega_c^{\text{scalar}}(r = 5)/(2\pi) = 5.20\text{mHz}$.

The main characteristics of the potential are well represented by V_ℓ^{approx} , we can in particular distinguish three different regions depending on the location of ω with respect to the Lamb and Brunt-Väisälä

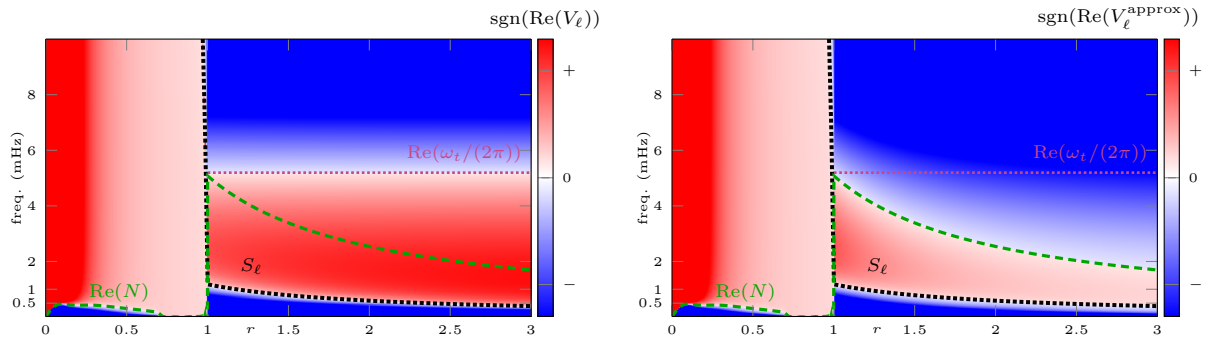


Figure 10: Comparisons of signs of the vector potential V_ℓ of (3.34b), and the approximate potential V_ℓ^{approx} of (7.2) for mode $\ell = 750$ and $r \in (0, 3)$, using attenuation $\Gamma/(2\pi) = 20\mu\text{Hz}$. In the atmosphere, $\omega_t/(2\pi) = 5.19\text{mHz}$.

frequencies, S_ℓ and N respectively.

- $\omega < \text{Re}(N), S_\ell$: it corresponds to a propagative region ($V_\ell < 0$) and occurs at low frequencies.
 - In the interior ($r < 1$) the potential is negative in the radiative zone ($0 \leq r \leq 0.7$) for $\omega/2\pi \leq 0.5\text{mHz}$, cf. Figures 8 and 9. Concretely, for each frequency $\omega/2\pi \leq 0.5\text{mHz}$, there exists a region $([0, r_t])$, with $r_t \leq 0.7$ on which $V_\ell < 0$ and the solution propagates in this region. It corresponds to the propagative region of the internal gravity waves. This is a new feature of the vector modal operator \mathcal{L}_ℓ , since this type of region does not exist for the potential of the scalar modal operator, as shown on the right column of Figure 8 and Figure 9. Note that $\mathcal{L}_\ell^{\text{scalar}}$ ignores the effect of gravity.
 - In the atmosphere ($r > r_a = 1.00073$), the potential is negative for large values of ℓ ($\omega \leq 1.2\text{mHz}$ for $\ell = 750$, see Figure 9). The frequency limit below which the potential is negative increases with increasing ℓ , for instance, this region exists at mode $\ell = 100$ for frequencies below 0.2mHz (compared to frequencies below 1.2mHz for $\ell = 750$). It is important to stress that having a propagative region below the Lamb frequency for high degree modes is a particularity of the vector-wave problem, and has a direct impact on the computational experiments. It represents the most challenging case for the radiation boundary conditions which are innately less effective at low frequencies. In this case, one needs to place the artificial boundary further out to ensure the accuracy of the solution.
- $\omega > \text{Re}(N), S_\ell$: it corresponds to a propagative region of the solar acoustic waves. For $\omega < \omega_t$, this region is located between S_ℓ and the solar surface. For $\omega > \omega_t$, these waves can propagate in the atmosphere, cf. the blue region in the upper right of Figures 8 and 9. This behavior is shared by both the vector and scalar potentials.
- $\text{Re}(N) < \omega < S_\ell$: in this region the potential is negative and the waves are decaying exponentially (see red region in the interior in Figures 8 and 9). This region also exists in the scalar problem but is located between 0 and S_ℓ as the gravity waves are not present.

However, the approximation of the potential by V_ℓ^{approx} is not accurate in particular close to the surface and r^* , see Figure 10. In addition, contrary to what is expected with V_ℓ^{approx} , the change of sign of the potential does not exactly occur at r^* . In Figure 11, we further highlight the difference in position between the zero of V_ℓ and r^* , which can be seen on Figures 8 and 9 with a tiny red area for $r > r^*$. We plot the potential V_ℓ at 7mHz for mode $\ell = 20$ in Figure 11, with a zoom near r^* which is located in this case in $r^* = 0.272$. We can clearly see that the change of sign in the potential appears after r^* , here for $r = 0.296$. We also compare in Figure 11 two levels of attenuation, to show that the width and height of the peak that appears at r^* depend on it. Namely, the width (i.e., the size between the two positions where $V_\ell = 0$ around r^*) is twice as large when the attenuation is increased by two. This is the expected behavior for a damped harmonic oscillator.

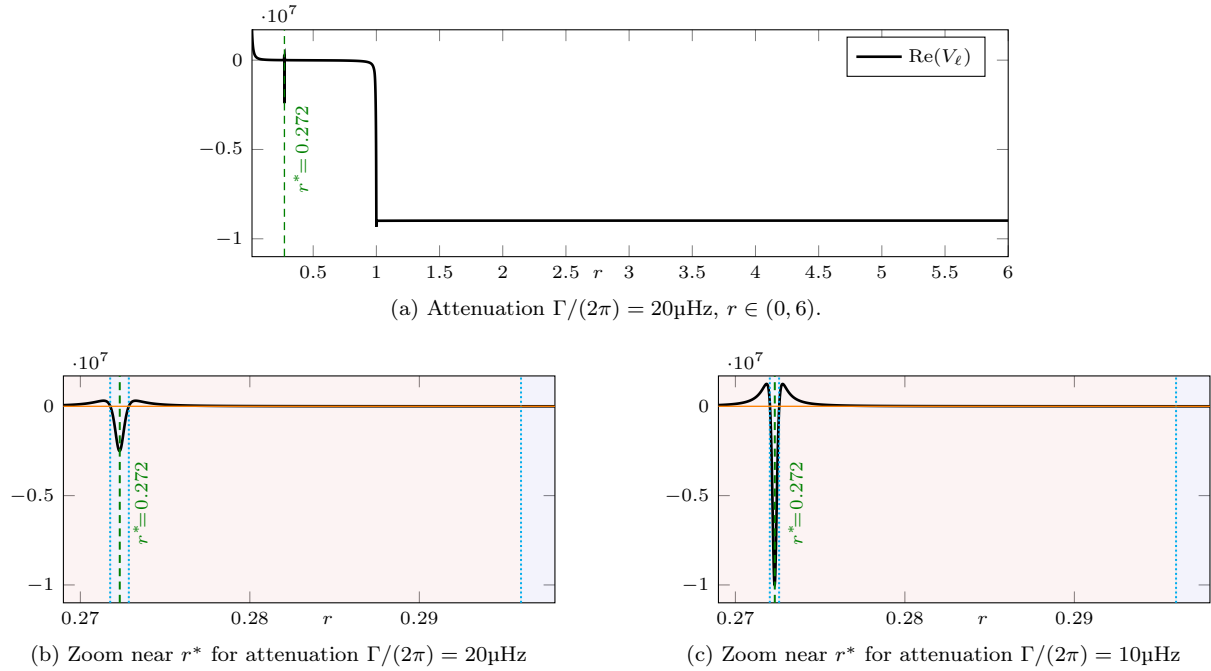


Figure 11: Vector potential V_ℓ of (3.34b) at 7mHz for mode $\ell = 20$, with zoom near r^* for different level of attenuation. The background color indicates when the potential is positive (red) and negative (blue). The horizontal line shows $y = 0$.

7.2 Original and conjugated regular solutions, effect of attenuation

We compare the original and conjugated solutions of regular problems where we use the background coefficients of the solar model S-AtmoI of [22]. We consider the (scaled) interval $(0, 1.0008)$ for the simulations, with Neumann boundary condition in $r_{\min} = 0$ and Dirichlet boundary condition in $r_{\max} = 1.0008$.

7.2.1 Original and conjugated problems

We remind below the two equivalent problems that are solved, namely the ‘original’ and ‘conjugated’, whose operators are referred to as \mathfrak{L} and \mathcal{L} such that

$$\text{original problem:} \quad \mathfrak{L} := \hat{q}_\ell(r) \partial_r^2 + q_\ell(r) \partial_r + \tilde{q}_\ell(r). \quad (7.3)$$

$$\text{conjugated problem:} \quad \mathcal{L} := -\partial_r^2 + V_\ell(r). \quad (7.4)$$

The solutions of the problems are respectively labeled as w_o and w_c .

The numerical discretization uses the HDG method depicted in Subsection 5.4, and is based upon the solutions of the corresponding first-order systems:

$$\text{original problem} \quad \tilde{\mathfrak{L}}(w_o, v_o) = \begin{pmatrix} \hat{q}_\ell r \partial_r + q_\ell(r) & \tilde{q}_\ell(r) \\ 1 & -r \partial_r \end{pmatrix} \begin{pmatrix} v_o \\ w_o \end{pmatrix}, \quad (7.5)$$

and

$$\text{conjugated problem} \quad \tilde{\mathcal{L}}(w_c, v_c) = \begin{pmatrix} -r - r^2 \partial_r & r^2 V_\ell \\ r & 1 - r \partial_r \end{pmatrix} \begin{pmatrix} v_c \\ w_c \end{pmatrix}. \quad (7.6)$$

Relation for boundary value problems We consider the wave propagation on the interval (r_{\min}, r_{\max}) with Neumann condition in r_{\min} and Dirichlet condition set to 1 in r_{\max} such that we have

$$\text{original problem} \quad \begin{cases} \tilde{\mathfrak{L}}(w_o, w_o) = 0 & \text{in } (r_{\min}, r_{\max}), \\ v_o(r = r_{\min}) = 0, & w_o(r = r_{\max}) = 1, \end{cases} \quad (7.7a)$$

$$(7.7b)$$

$$\text{conjugated problem} \quad \begin{cases} \tilde{\mathcal{L}}(w_c, w_c) = 0 & \text{in } (r_{\min}, r_{\max}), \\ v_c(r = r_{\min}) = 0, & w_c(r = r_{\max}) = 1. \end{cases} \quad (7.8a)$$

$$(7.8b)$$

In this case, the relation between w_o and w_c is given as follows,

$$w_c(r) = w_o(r) \frac{\mathfrak{J}_\ell(r_{\max})}{\mathfrak{J}_\ell(r)} = w_o(r) \frac{F_\ell(r_{\max})}{F_0(r_{\max}) K_\ell(r, r_{\max}) r_{\max}^2 c(r_{\max})^2 \rho(r_{\max})}, \quad (7.9)$$

where \mathfrak{J}_ℓ is given by (4.32), and the second equality is obtained using the definition of F_ℓ and K_ℓ respectively given in (2.19) and (3.85). In particular, we have that

$$K_\ell(r, s) = \mathfrak{J}_\ell(r) \mathfrak{J}_\ell(s). \quad (7.10)$$

To evaluate the accuracy of the discretization methods, we define the reconstructed conjugated solution obtained from the scaling of the original solution:

$$w_{oc}(r, s) := w_o(r) \frac{\mathfrak{J}_\ell(s)}{\mathfrak{J}_\ell(r)}. \quad (7.11)$$

Theoretically, $w_{oc} = w_c$, however this equality is not always achieved numerically. As pointed in [Subsection 3.2.1](#), the original solution is regular at r^* , and we use the reconstructed conjugated solution as a reference solution, which gives the true solution of \mathcal{L}_ℓ . An evaluation of the accuracy is given by comparing w_c with w_{oc} .

7.2.2 Numerical comparisons

In [Figure 12](#), we show the solutions of the original and conjugated problems for different frequencies and modes, using the background coefficients of solar model **S-AtmoI** and attenuation $\Gamma/(2\pi) = 20\mu\text{Hz}$. We see that the solution of the original problem gives high variation in amplitude, with five order of magnitude difference between the values near the origin and the atmosphere. On the other hand, the solution of the conjugated equation has the same order of magnitude in the entire interval. We see that w_{oc} , obtained after scaling the solution w_o by (7.11), corresponds to the solution of the conjugated problem, cf. [Figures 12c](#) and [12d](#). In the case where the mode is non-zero, we further see that the amplitude of the signal tends rapidly to zero after r^* (from right to left, i.e., in the interval $(0, r^*)$). We further see that a peak appears in the solution of the conjugated equation at this position (we remind that r^* corresponds to a singularity in the case without attenuation). On the other hand, the signal remains smooth for the solution of the original problem.

In [Figure 13](#), we picture the solutions using a lower level of attenuation, with $\Gamma/(2\pi) = 1\mu\text{Hz}$. Contrary to the previous case where $\Gamma = 20\mu\text{Hz}$, we observe a discrepancy between the solution of the conjugated problem w_c and the scaled solution w_{oc} , see [Figures 13a](#) and [13d](#). While the peak indicating the position of r^* appears in w_{oc} , it is missing in w_c , indicating that the discretization of the conjugated equation is not able to accurately describe the phenomenon. This observation is confirmed when computing w_c using a refined mesh (corresponding to the distance between nodes divided by five), see [Figure 13c](#). The solution using the refined mesh shows the appropriate peak and corresponds to w_{oc} . This computation highlights the difficulty of simulating the conjugated problem, which needs to be sufficiently accurate in the area near r^* to capture the appropriate behaviour. Here, one needs to refine the mesh, and we had to increase by 5 the number of nodes to capture the correct solution. It is also possible to use only a local refinement, that is, to refine only near the position of r^* . However, this means having to adapt the mesh for each frequency and mode, with a preliminary computation of the position r^* . On the other hand, the solution of the original problem is accurate without refinement, because the behaviour near r^* is encoded in the scaling factor to compute w_{oc} in (7.11).

We picture the limiting case, without attenuation ($\Gamma = 0$), in [Figure 14](#), for which the conjugated problem is expected to show a singularity in $r = r^*$. Here, despite the use of the refined mesh, the singularity does not appear in w_c , while it is visible when plotting w_{oc} . In addition, not only the singularity is not described by w_c , but also the amplitude of the signal is not correct in the interval compared to w_{oc} .

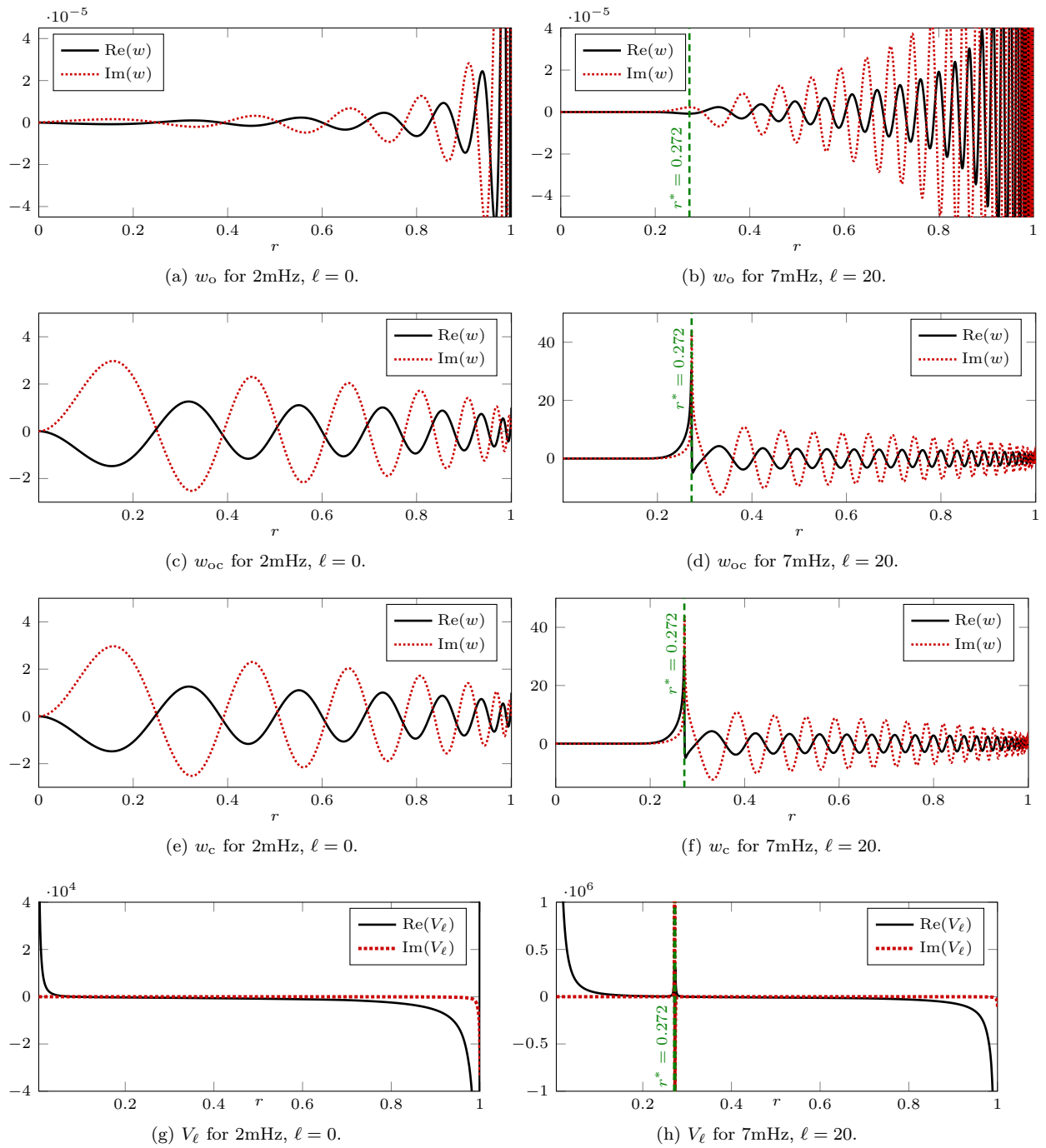


Figure 12: Comparisons of the solutions of the boundary value problems (7.7) and (7.8) on $(0, 1.0008)$, and w_{oc} obtained with (7.11). The computations use the background coefficients of model S-AtmoI for different modes and frequencies, with attenuation $\Gamma/(2\pi) = 20\mu\text{Hz}$. For non-zero modes, the position of r^* is given by a vertical dashed line.

As a conclusion of this group of experiments, the conjugated equation to solve the problem must be carefully used: with a sufficient level of attenuation, e.g., $\Gamma/(2\pi) = 20\mu\text{Hz}$ in Figure 12, it allows to visualize a signal which maintains a constant magnitude in the entire interval. On the other hand, with low attenuation, the position of r^* must be discretized finely to identify the peaks. In the limiting case without attenuation, the conjugated approach has to be avoided as it is not able to capture the singularity. As an alternative, solving the original problem, and obtaining the conjugated solution with

the appropriate scaling given by (7.11) gives a robust result and allows to capture the correct behaviour of the solutions in all cases.

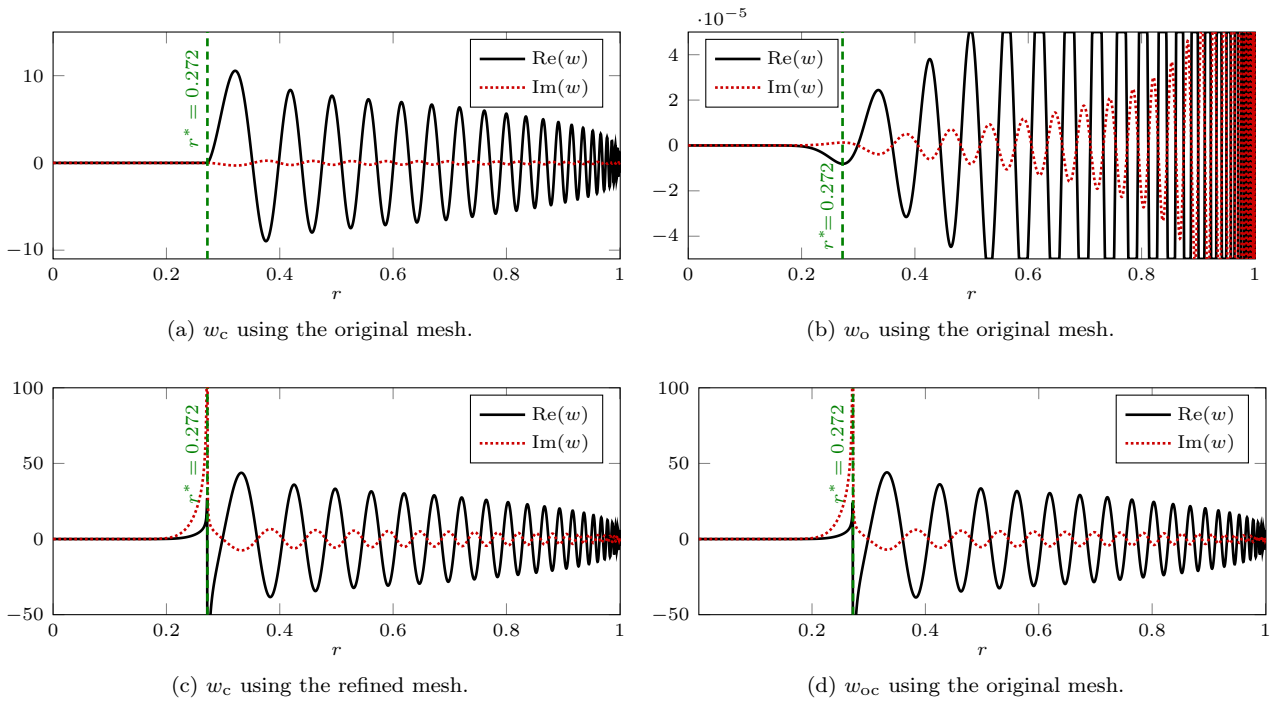


Figure 13: Comparisons of the solutions of the boundary value problems (7.7) and (7.8) on $(0, 1.0008)$, and w_{oc} obtained with (7.11). The computations use the background coefficients of model **S-AtmoI** with frequency 7mHz and mode $\ell = 20$, with attenuation $\Gamma/(2\pi) = 1\mu\text{Hz}$. The position of r^* is given by a vertical dashed line. The ‘refined’ mesh is obtained dividing by five the distance between the nodes of the original mesh.

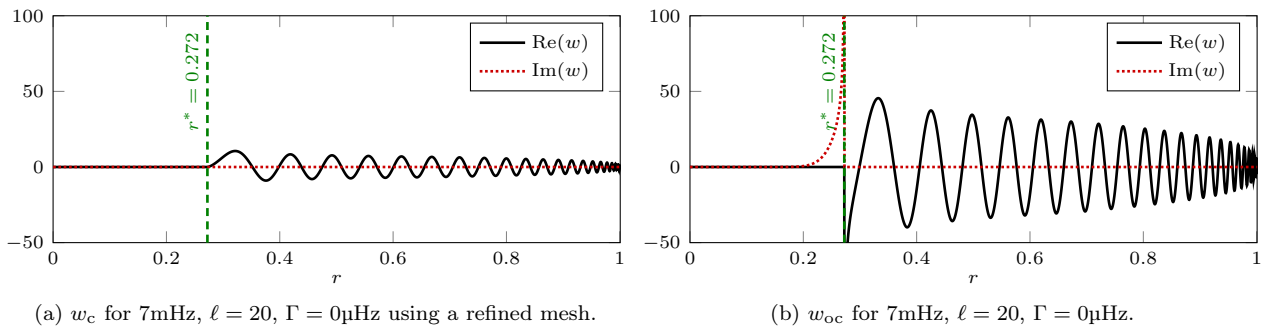


Figure 14: Comparisons of the solutions w_c and w_{oc} , respectively (7.6) and (7.11), using the background coefficients of model **S-AtmoI** at frequency 7mHz and mode $\ell = 20$, without attenuation. A Neumann boundary condition is implemented in $r = 0$ and a Dirichlet boundary condition set to one in $r = r_{\max} = 1.0008$. The position of r^* is given by a vertical dashed line. The refined mesh is obtained by dividing by five the distance between the nodes of the initial mesh.

Remark 18. *In terms of computation, one advantage of the discretization of the conjugated equation (7.4) is to provide a symmetric matrix, contrary to the discretization of the original problem (7.3). While this may not appear important for the modal one-dimensional problem we currently solve, this will drastically reduce the computational time when considering three-dimensional problems, hence the conjugated equation cannot be discarded.* \diamond

7.3 Efficiency of the radiation boundary conditions

To implement and compare the radiation boundary conditions (RBC) given in Section 6, we consider an interior source problem with a Robin boundary condition at $r = r_{\max}$ and a delta-Dirac source. We have

$$\text{original problem} \quad \begin{cases} \tilde{\mathcal{L}}(w_o, w_o) = \delta(s) & \text{in } (r_{\min}, r_{\max}), \\ v_o(r = r_{\min}) = 0, \quad w_o(r = r_{\max}) = i\mathcal{Z}_{\bullet}(r_{\max})w_o(r_{\max}). \end{cases} \quad \begin{matrix} (7.12a) \\ (7.12b) \end{matrix}$$

$$\text{conjugated problem} \quad \begin{cases} \tilde{\mathcal{L}}(w_c, w_c) = \delta(s) & \text{in } (r_{\min}, r_{\max}), \\ v_c(r = r_{\min}) = 0, \quad w_c(r = r_{\max}) = i\mathcal{Z}_{\bullet}(r_{\max})w_c(r_{\max}). \end{cases} \quad \begin{matrix} (7.13a) \\ (7.13b) \end{matrix}$$

Remark 19 (Computational cost). *One motivation for investigating the efficiency of radiation conditions is to reduce the computational domain while maintaining the accuracy of the solution, hence reducing the computational cost. Here, we use the open-source software `hawen`, [21], which enables for parallel computation. To give an idea of the computational cost, the resolution of the ODE with 4 processors on the domain $(0, 10)$ takes about 12sec on a laptop, while it takes about 5sec on domain $(0, 1.0008)$. Using 1 processor (i.e., sequential run), the computational time on domain $(0, 10)$ is about 36sec, and about 14sec for domain $(0, 1.0008)$. While we already observe the computational benefit of the domain truncation with our one-dimensional problem, it is obviously even more important in higher dimensions.*

◇

7.3.1 Construction of a reference solution

We generate a “reference” solution by considering the problem on a large interval (r_{\min}, r_{\max}^D) , where a Dirichlet boundary condition is selected in $r_{\max}^D \gg r_{\max}$ with $w_{\bullet}(r_{\max}^D) = 0$. In these experiments, the Dirac source is positioned in $s = 1$ and the background coefficients follow the solar model `S-AtmoI` with attenuation $\Gamma/(2\pi) = 20\mu\text{Hz}$. We illustrate the different configurations of potentials observed in Subsection 7.1:

- In Figure 15, we use 7 mHz and mode $\ell = 20$: the simulated frequency is above the atmospheric cut-off frequency, hence waves propagate. Furthermore, r^* is positioned in the interior.
- In Figure 16, we use 2 mHz and mode $\ell = 20$: the simulated frequency is below the atmospheric cut-off frequency, and above the Lamb frequency there, hence waves are evanescent in the exterior.
- In Figure 17, we use 0.2mHz and mode $\ell = 750$: the simulated frequency is below atmospheric cut-off and Lamb frequencies, hence the potential has the profile of a well in the exterior. In addition, r^* is positioned in the atmosphere.

The computational interval is $(0, 10)$, while with our solar model `Atmo-I`, the atmosphere starts in $r_a = 1.00073$. Here we use the conjugated wave problem for the simulations, which is sufficiently accurate with such a level of attenuation. It also allows us to easily implement the non-local RBC $\mathcal{Z}_{\text{NL}}^{\ell}$.

Accordingly to Subsection 7.1, we observe different situations depending on the sign of the potential, with propagating or evanescent waves. Due to the presence of attenuation, the solution always tends to zero at the end of the interval, with an oscillatory pattern of the solution as further studied below. This allows us to consider such simulations on large interval as “reference” solutions to investigate the accuracy of the RBC for domain truncation.

7.3.2 Oscillatory pattern of solutions and Whittaker’s function

We further highlight the oscillatory pattern of solutions (those that propagate in the atmosphere) that was already visible for example in Figure 15c. In Figure 18, we represent the solution for different values of ℓ . Their periods are constant, whether they are evaluated close to the surface, $(0.002105$ for interval $r \in (1.0008, 10)$), or if we restrict to the part further away (same period in the interval $r \in (5, 10)$). While solutions may not be superposed as the phases are different at the origin, the key-point is that the period of the oscillations of the solution is the same for all modes, and corresponds accurately to the one given by $(k_a/(2\pi))^{-1} = 0.002105$.

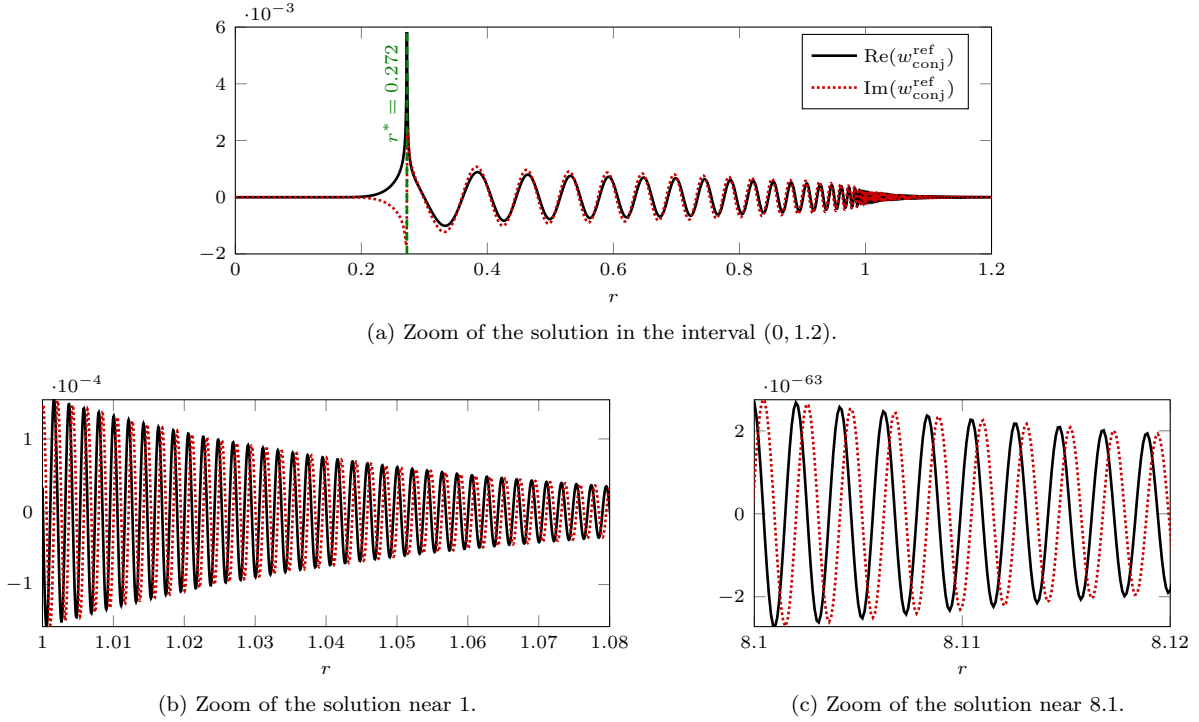


Figure 15: Reference solution at 7mHz for mode $\ell = 20$ with attenuation $\Gamma/(2\pi) = 20\mu\text{Hz}$. The solution is computed considering a domain $(0, 10)$ with a Dirichlet condition set in $r_{\max}^D = 10$. Here, the potential is negative in the atmosphere (see Figure 8), such that waves propagate in the exterior, nonetheless with very low amplitudes due to the attenuation.

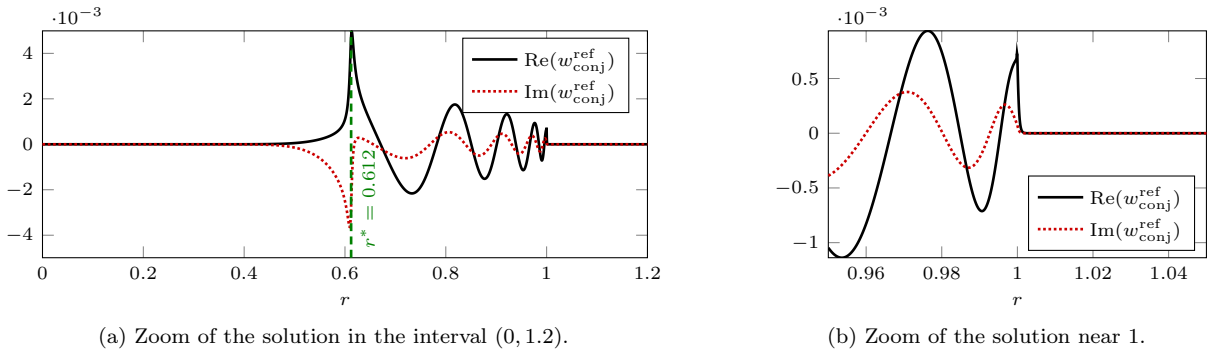


Figure 16: Reference solution at 2mHz for mode $\ell = 20$ with attenuation $\Gamma/(2\pi) = 20\mu\text{Hz}$. The solution is computed considering a domain $(0, 10)$ with a Dirichlet condition set in $r_{\max}^D = 10$. Here, the potential is positive in the atmosphere (see Figure 8), such that waves are evanescent in the exterior.

In Figure 19, we plot the Whittaker's function for mode $\ell = 20$ and 200 at a frequency of 7 mHz. The appropriate period is recovered but only when considering an interval sufficiently far from the surface. Namely, we need to consider $r > 5$ to obtain the correct period given by k_a . It means that an error would be introduced by applying RBC too close to the surface. We quantify this error in the next section.

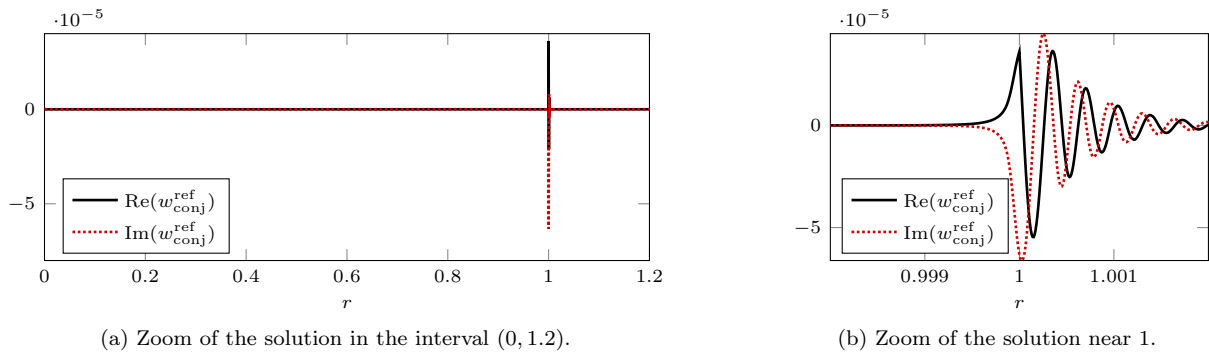


Figure 17: Reference solution at 0.2MHz for mode $\ell = 750$ with attenuation $\Gamma/(2\pi) = 20\mu\text{Hz}$. The solution is computed considering a domain $(0, 10)$ with a Dirichlet condition set in $r_{\max}^D = 10$. Here, the potential has the profile of a well in the atmosphere (see Figure 9), with a change of sign, from negative (propagating waves) to positive (evanescent waves).

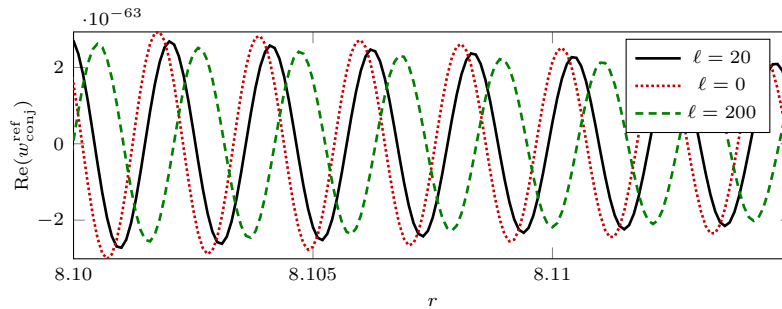


Figure 18: Oscillations of the reference solution at 7MHz for modes $\ell = 20, 0$ and 200 . The solution is computed considering a domain $(0, 10)$ with a Dirichlet condition set in $r_{\max}^D = 10$ with attenuation $\Gamma/(2\pi) = 20\mu\text{Hz}$. The mean period of the signal for interval $r \in (1.0008, 10)$ is of 0.002105 for modes $\ell = 0, \ell = 20$ and $\ell = 200$. For the signal restricted in interval $r \in (5, 10)$, the mean period is of 0.002106 for modes $\ell = 0, \ell = 20$ and $\ell = 200$. For frequency 7MHz, we have $(k_a/(2\pi))^{-1} = 0.002105$.

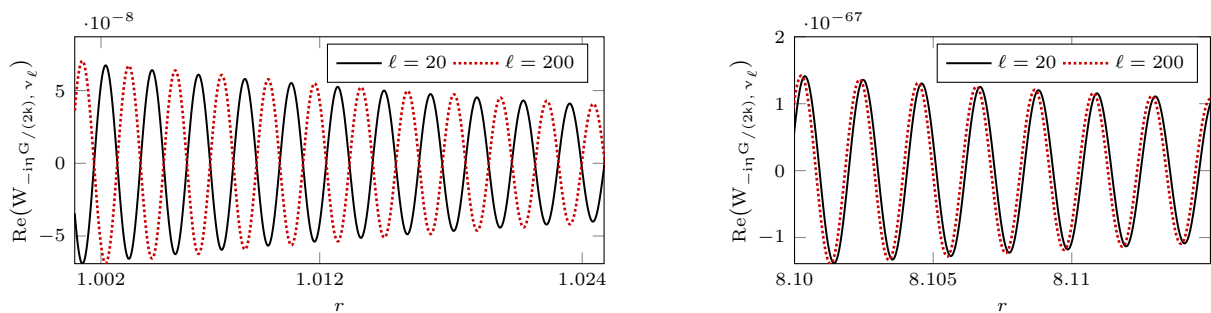


Figure 19: Evaluation of the Whittaker function $W_{-i\eta G/(2k), \nu_\ell}(-2i r k(r))$ at frequency 7MHz with attenuation $\Gamma/(2\pi) = 20\mu\text{Hz}$ for different modes. The mean period of these signals for interval $r \in (1.0008, 10)$ is of 0.00211895 for mode $\ell = 20$ and 0.00212095 for mode $\ell = 200$. For the signal restricted in interval $r \in (5, 10)$, the mean period is of 0.002106 for mode $\ell = 20$ and 0.002107 for mode $\ell = 200$. For frequency 7MHz, we have $(k_a/(2\pi))^{-1} = 0.002105$.

7.3.3 Position of the radiation boundary conditions

We evaluate the accuracy of the radiation condition with respect to the distance at which it is implemented, that is, the accuracy depending on r_{\max} . We define the relative error ϵ_{rel} such that

$$\epsilon_{\text{rel}}(x) = \frac{|w^{\text{ref}}(x) - w^{\mathcal{Z}^\bullet}(x)|}{|w^{\text{ref}}(x)|}. \quad (7.14)$$

We use the conjugated problem and RBC $\mathcal{Z}_{\text{NL}}^\ell$, with two levels of attenuation: $\Gamma/(2\pi) = 20\mu\text{Hz}$ and $\Gamma/(2\pi) = 1\mu\text{Hz}$. Figures 20 to 22 show the solutions for different modes, at frequency 0.2, 2 and 7mHz respectively. In Figure 23, we picture the evolution of the mean of the relative error, $\text{mean}(\epsilon_{\text{rel}})$, depending on the frequencies and modes.

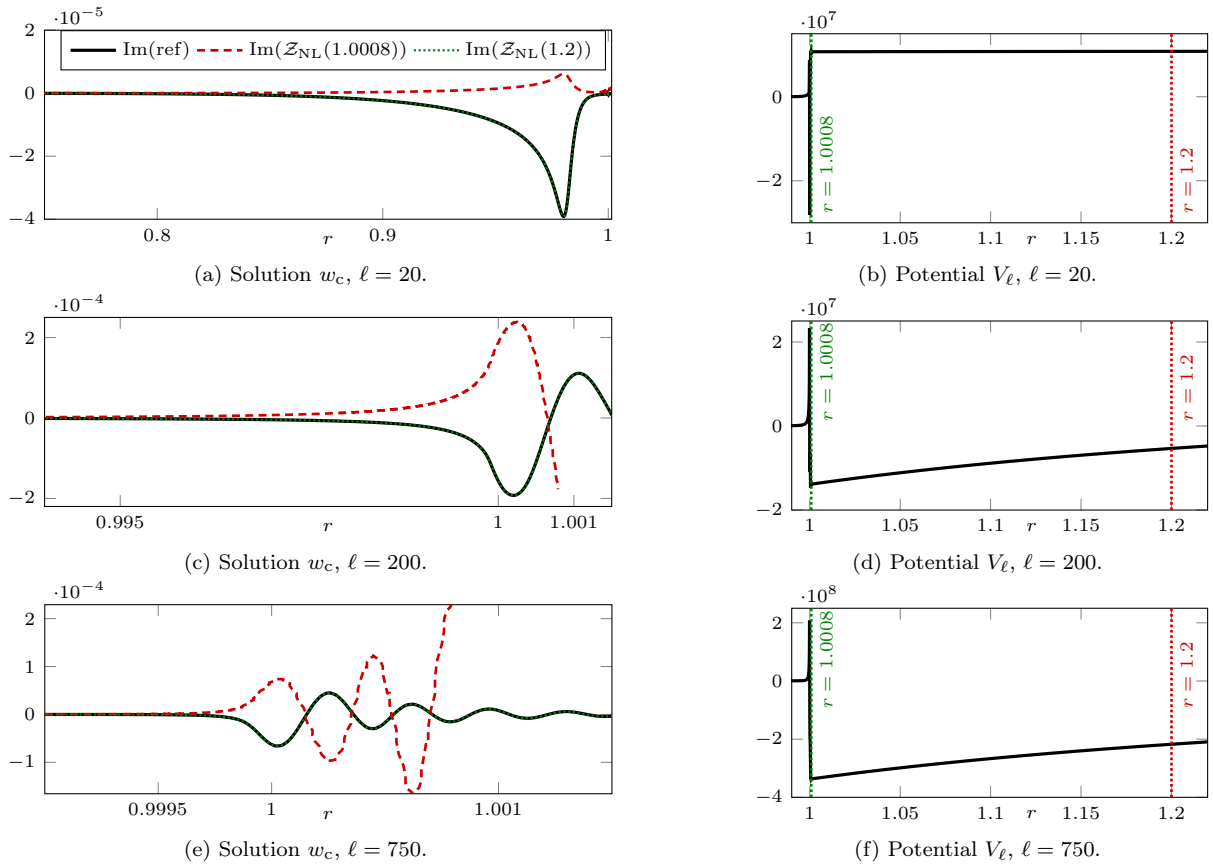


Figure 20: Potentials V_ℓ and comparison of the imaginary parts of the solution w_c at frequency 0.2mHz depending on the position of the RBC $\mathcal{Z}_{\text{NL}}^\ell$, with $\Gamma/(2\pi) = 20\mu\text{Hz}$.

Following the description of the behaviour of the potential given in Subsection 7.1, we highlight three configurations depending on the frequency:

- **Above the cut-off frequency** (Figure 22 and Figures 23g and 23h). The relative error is already very small when the RBC is positioned very close to the surface, in $r = 1.0008$. The solution in this case cannot be distinguished visually from the reference. The error remains stable as we move the position of the RBC further away, even with a low level of attenuation. Therefore, the RBC is very effective in this context, and one can truncate the domain close to the surface without losing accuracy, with relative error of magnitude 10^{-9} . This behavior is similar to what was observed studying the scalar problem [8].

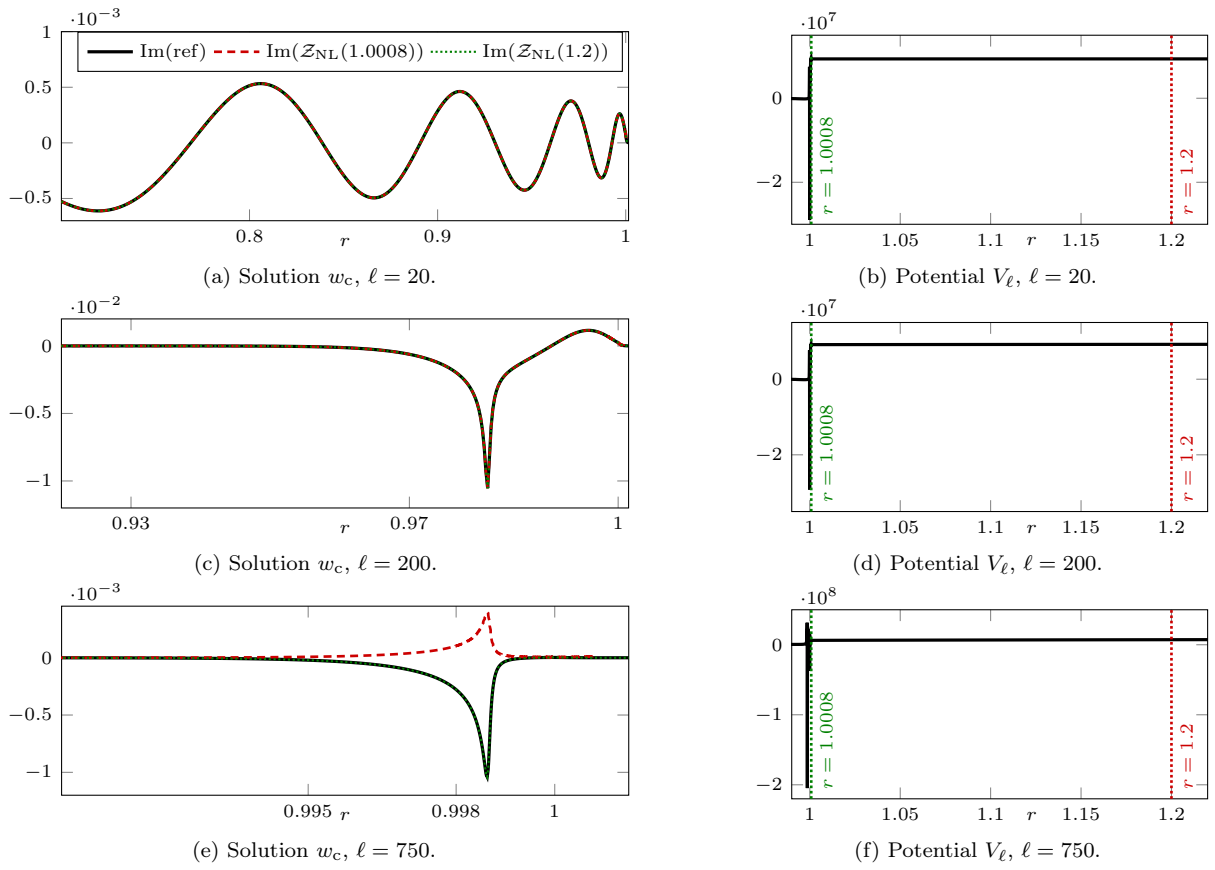


Figure 21: Potentials V_ℓ and comparison of the imaginary parts of the solution w_c at frequency 2mHz depending on the position of the RBC Z_{NL}^ℓ , with $\Gamma/(2\pi) = 20\mu\text{Hz}$.

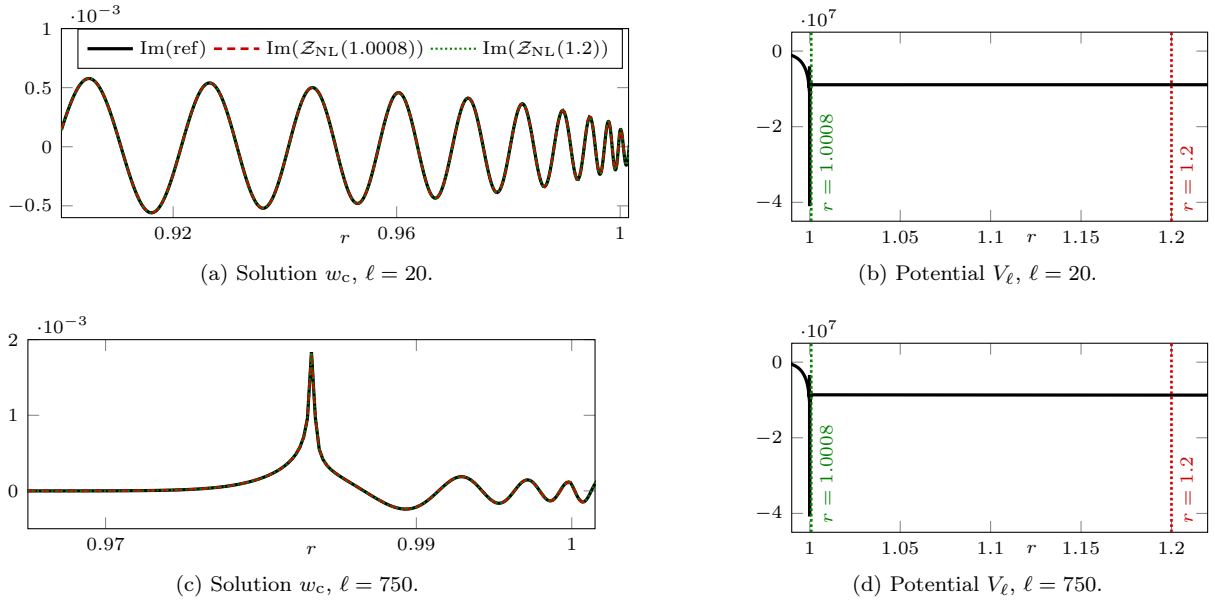


Figure 22: Potentials V_ℓ and comparison of the imaginary parts of the solution w_c at frequency 7mHz depending on the position of the RBC Z_{NL}^ℓ , with $\Gamma/(2\pi) = 20\mu\text{Hz}$.

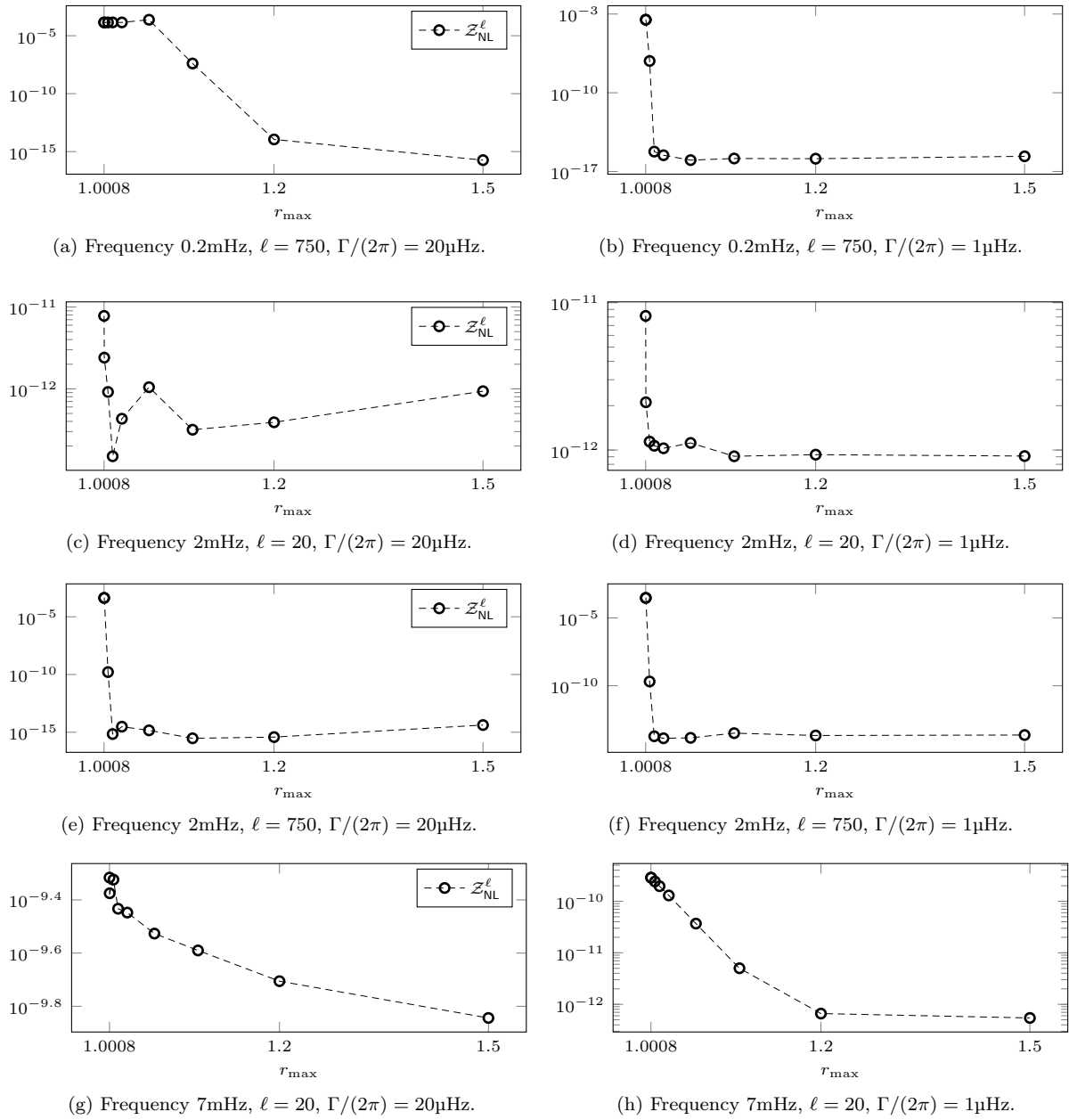


Figure 23: Mean of the relative error depending on the RBC and its position r_{\max} . We compare the following values of r_{\max} : 1.0008, 1.0010, 1.005, 1.01, 1.02, 1.05, 1.1, 1.2 and 1.50.

– **Between the Lamb and the cut-off frequencies** (Figure 21 and Figures 23c to 23f).

- For low modes and (relatively to the mode) high-frequency range, see Figure 21, the RBC positioned in $r = 1.0008$ gives an accurate solution, and the relative error is stable, Figures 23c and 23d.
- For higher modes and (relatively to the mode) low-frequency range in Figure 21, we see that the solution with the RBC in $r = 1.0008$ is inaccurate, and one needs to move it further away to obtain satisfactory results. Nonetheless, as shown by the relative errors in Figures 23e and 23f, the RBC solutions improves (about 10^{-10} relative error) when slightly moving away the RBC. Namely, it appears that it is sufficient to impose the condition in $r_{\max} = 1.0010$.

- **Below both the cut-off and the Lamb frequencies** (Figure 20 and Figures 23a and 23b). The solution with the RBC positioned in $r = 1.0008$ is inaccurate. Contrary to the previous case, one has to position it much further out to obtain satisfactory results, see Figures 23a and 23b. Here, it seems necessary to go up to $r_{\max} = 1.2$ to ensure the accuracy of the results. While we expect RBC to be less efficient at low frequencies, here, the case of a potential having the profile of a well in the atmosphere (see Subsection 7.1) further complicates the computations. Putting the boundary condition so far away is computationally expensive but also physically irrelevant. Our atmospheric model is reasonable up to $r_{\max} = 1.003$. At this point corresponding to the end of the photosphere, the temperature increases by four orders of magnitude and so the sound speed by two orders. Thus, the isothermal model considered here is not valid anymore after this point. Studying these waves will require to model the atmosphere using for example the VAL-C atmospheric model, [39], or to add more physics into the problem, for example by removing the adiabatic approximation. We further note that this situation, where one has to move the artificial boundary further out, does not appear in the scalar wave approximation, see [8, 3].

7.3.4 Analysis of performance

In Figure 24, we compare the relative error between the reference solution given in Figure 15 and simulations using condition $\mathcal{Z}_{\text{NL}}^\ell$ either in $r_{\max} = 1.5$ or $r_{\max} = 1.0008$. This corresponds to frequency 7mHz and mode $\ell = 20$, with attenuation $\Gamma/(2\pi) = 20\mu\text{Hz}$. That is, we consider a frequency above the cut-off, see Subsection 7.1. We observe that the difference is relatively stable in the whole interval, with mild variations for $r_{\max} = 1.5$. In particular, we note that the difference does not increase near the boundary condition. When the RBC is positioned at $r_{\max} = 1.0008$, the relative difference is already low with magnitude 10^{-7} , and two orders of magnitude are further gained using $r_{\max} = 1.5$ (i.e., increasing the domain by 50%).

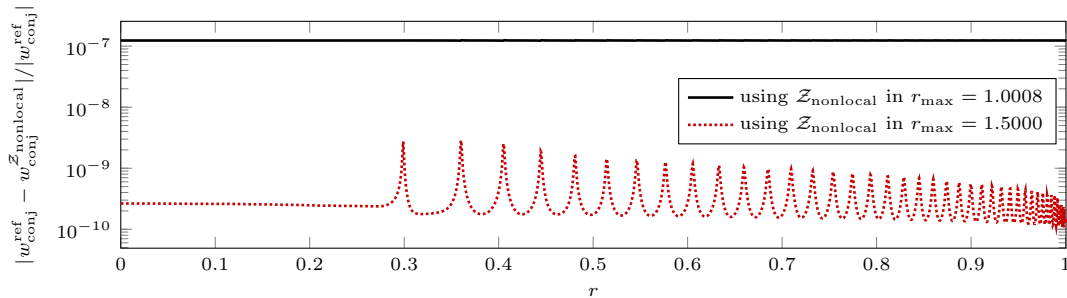


Figure 24: Relative difference between the reference solution computed using a Dirichlet boundary condition in $r_{\max}^D = 10$ (see Figure 15) and solutions using the boundary condition $\mathcal{Z}_{\text{NL}}^\ell$ in $r_{\max} = 1.0008$ and $r_{\max} = 1.5$. The computations correspond to frequency 7mHz and mode $\ell = 20$, with attenuation $\Gamma/(2\pi) = 20\mu\text{Hz}$.

In Figure 25, we keep frequency 7mHz and now use mode $\ell = 200$, comparing the results using RBC $\mathcal{Z}_{\text{S-HF-3}}^\ell$ and $\mathcal{Z}_{\text{S-HFG-3}}^\ell$ positioned at $r_{\max} = 1.0008$. It is visually not possible to distinguish the differences between the solutions, and the relative errors pictured in Figure 25c confirm the consistency on the entire interval. We clearly observe the improvement of the condition $\mathcal{Z}_{\text{S-HFG-3}}^\ell$ over $\mathcal{Z}_{\text{S-HF-3}}^\ell$, with a gain of about 3 order of magnitude in the relative difference. We remind that the difference in the conditions only comes from the consideration of the gravity term, cf. (6.19) and (6.20), and yet it makes a drastic improvement in the approximations.

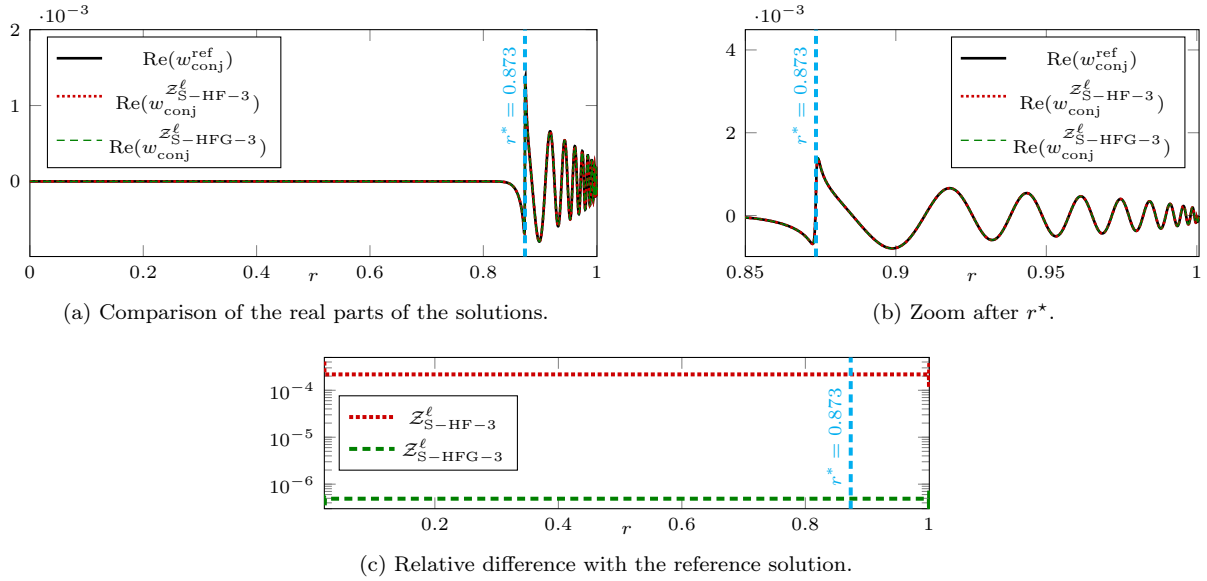


Figure 25: Comparisons of the solutions at frequency 7mHz for mode $\ell = 200$ with attenuation $\Gamma/(2\pi) = 20\mu\text{Hz}$. The reference solution is computed with a Dirichlet condition in $r_{\text{max}}^D = 10$ while the RBC $\mathcal{Z}_{\text{S-HF-3}}^{\ell}$ and $\mathcal{Z}_{\text{S-HFG-3}}^{\ell}$ are set up in $r_{\text{max}} = 1.0008$. The relative difference corresponds to $|w^{\text{ref}} - w^{\mathcal{Z}}|/|w^{\text{ref}}|$, with mean values given in Table 4.

We compare the RBC introduced in Section 6, and indicate the mean of the relative error on the interval in Table 4. For simplicity, we only show the cases (7mHz, $\ell = 20$) and (2mHz, $\ell = 20$). The reference solution is computed on the interval $(0, 10)$ with Dirichlet condition in $r_{\text{max}}^D = 10$, while the radiation conditions are set up in $r_{\text{max}} = 1.0008$. In Table 5, we include results using the original equations, and use the reference solution computed on $(0, 5)$.

We observe that

- The efficiency of the conditions is consistent between the conjugated and original equations, see Table 5. Namely, we have same magnitudes in the relative difference, and same performance.
- As expected, condition $\mathcal{Z}_{\text{NL}}^{\ell}$ is the most efficient, while conditions $\mathcal{Z}_{\text{S-HFG-2}}^{\ell}$, $\mathcal{Z}_{\text{S-HFG-3}}^{\ell}$ and $\mathcal{Z}_{\text{aNL-G}}^0$ show comparable accuracy.
- We see that encoding the gravity term in the condition, cf. $\mathcal{Z}_{\text{S-HFG-2}}^{\ell}$ and $\mathcal{Z}_{\text{S-HFG-3}}^{\ell}$ compared to $\mathcal{Z}_{\text{S-HF-2}}^{\ell}$ and $\mathcal{Z}_{\text{S-HF-3}}^{\ell}$ greatly improve the efficiency of the conditions, reducing the relative error by up to 3 orders of magnitude.
- Regarding the conditions that are independent of the mode ℓ , which are particularly convenient for computations in dimension 2 or 3, we see that $\mathcal{Z}_{\text{S-HFG-1}}$ and $\mathcal{Z}_{\text{G-LR}}$ are the most accurate at mode $\ell = 0$, and for higher modes, $\mathcal{Z}_{\text{aNL-G}}^0$ also gives similar error as these two conditions.

Table 4: Mean of the relative difference between radiation conditions in $r_{\max} = 1.0008$ and a reference solution computed on $(0, 10)$ with Dirichlet condition. The computations correspond to the conjugated equation with attenuation $\Gamma/(2\pi) = 20\mu\text{Hz}$.

RBC	2mHz, $\ell=0$	2mHz, $\ell=20$	2mHz, $\ell=200$	7mHz, $\ell=0$	7mHz, $\ell=20$	7mHz, $\ell=200$
$\mathcal{Z}_{\text{NL}}^{\ell}$	3.33×10^{-9}	4.54×10^{-9}	2.10×10^{-7}	1.38×10^{-7}	1.24×10^{-7}	5.99×10^{-8}
$\mathcal{Z}_{\text{aNL-G}}^{\ell}$	3.48×10^{-9}	6.76×10^{-9}	3.05×10^{-7}	1.50×10^{-7}	1.37×10^{-7}	4.14×10^{-7}
$\mathcal{Z}_{\text{aNL}}^{\ell}$	8.04×10^{-6}	9.66×10^{-6}	4.77×10^{-6}	2.51×10^{-4}	2.30×10^{-4}	2.13×10^{-4}
$\mathcal{Z}_{\text{S-HFG-0}}$	1.44×10^{-6}	4.47×10^{-6}	1.27×10^{-4}	4.51×10^{-5}	3.55×10^{-5}	4.64×10^{-4}
$\mathcal{Z}_{\text{S-HFG-1}}$	3.06×10^{-9}	2.73×10^{-6}	1.26×10^{-4}	2.48×10^{-7}	5.85×10^{-6}	5.03×10^{-4}
$\mathcal{Z}_{\text{S-HFG-2}}^{\ell}$	1.13×10^{-9}	2.34×10^{-9}	8.37×10^{-7}	1.98×10^{-7}	1.80×10^{-7}	4.80×10^{-7}
$\mathcal{Z}_{\text{S-HFG-3}}^{\ell}$	1.15×10^{-9}	2.38×10^{-9}	8.37×10^{-7}	1.97×10^{-7}	1.80×10^{-7}	4.79×10^{-7}
$\mathcal{Z}_{\text{S-HF-0}}$	9.48×10^{-6}	1.41×10^{-5}	1.32×10^{-4}	2.97×10^{-4}	2.65×10^{-4}	2.51×10^{-4}
$\mathcal{Z}_{\text{S-HF-1}}$	8.03×10^{-6}	1.24×10^{-5}	1.31×10^{-4}	2.51×10^{-4}	2.24×10^{-4}	2.90×10^{-4}
$\mathcal{Z}_{\text{S-HF-2}}^{\ell}$	8.04×10^{-6}	9.66×10^{-6}	5.53×10^{-6}	2.51×10^{-4}	2.30×10^{-4}	2.13×10^{-4}
$\mathcal{Z}_{\text{S-HF-3}}^{\ell}$	8.04×10^{-6}	9.66×10^{-6}	5.53×10^{-6}	2.51×10^{-4}	2.30×10^{-4}	2.13×10^{-4}
$\mathcal{Z}_{\text{G-LR}}$	5.46×10^{-9}	2.72×10^{-6}	1.26×10^{-4}	1.86×10^{-7}	5.77×10^{-6}	5.03×10^{-4}
$\mathcal{Z}_{\text{aNL-G}}^0$	8.03×10^{-6}	2.72×10^{-6}	1.26×10^{-4}	1.86×10^{-7}	5.77×10^{-7}	5.03×10^{-4}
$\mathcal{Z}_{\text{aNL}}^0$	8.03×10^{-6}	1.24×10^{-5}	1.31×10^{-4}	2.51×10^{-4}	2.24×10^{-4}	2.90×10^{-4}
$\mathcal{Z}_{\text{S-G}}$	1.44×10^{-6}	4.46×10^{-6}	1.27×10^{-4}	4.51×10^{-5}	3.56×10^{-5}	4.64×10^{-4}
$\mathcal{Z}_{\text{SAI-0}}$	8.03×10^{-6}	1.24×10^{-5}	1.31×10^{-4}	2.51×10^{-4}	2.24×10^{-4}	2.90×10^{-4}
$\mathcal{Z}_{\text{SAI-1}}^{\ell}$	8.04×10^{-6}	9.66×10^{-6}	5.52×10^{-6}	2.51×10^{-4}	2.30×10^{-4}	2.13×10^{-4}
$\mathcal{Z}_{\text{SAI-2}}^{\ell}$	8.04×10^{-6}	9.66×10^{-6}	4.78×10^{-6}	2.51×10^{-4}	2.30×10^{-4}	2.13×10^{-4}
$\mathcal{Z}_{\text{aW-4}}^{\ell}$	8.04×10^{-6}	9.66×10^{-6}	4.82×10^{-6}	2.51×10^{-4}	2.30×10^{-4}	2.13×10^{-4}
$\mathcal{Z}_{\text{aW-1}}^{\ell}$	1.95×10^{-9}	2.96×10^{-6}	1.37×10^{-4}	1.08×10^{-7}	9.88×10^{-8}	1.19×10^{-7}

7.4 Modal Green's kernels

We now compute the Green's kernels, by deploying the reconstruction formula of Approach 2 with [Algorithm 1](#). Following our previous computations, we have highlighted that the original equation is more stable in the case of low (or without) attenuation, and that the RBC including the gravity term improves drastically the accuracy. Therefore, the simulations are performed using the original equation, with boundary condition $\mathcal{Z}_{\text{S-HFG-3}}^{\ell}$. We have also seen that, in the case of a low frequency coupled with a high mode, the RBC must be positioned relatively far away to ensure the numerical accuracy. We primarily avoid this case for the computation of the Green's kernels below, and refer to [Subsection 7.5](#) where we further investigate the low frequency/high modes configuration.

7.4.1 Comparison of the approaches

The computation of the Green's kernels using Approach 2 with [Algorithm 1](#) relies on the solutions of two regular problems, from which the entire kernels are assembled. On the other hand, Approach 1 requires one simulation for each of the source in the discretization, hence is much more intensive numerically speaking. In addition, Approach 1 relies on the discretization of the Dirac source, hence encodes a singularity at this position, while Approach 2 only requires solving the two boundary value problems. We compare the two approaches in [Figure 26](#), where we picture the kernel for the positions where source and receiver coincide, that is, we plot $G_{\ell}^{+}(r, r)$. The plots correspond with 4001 different source positions, for frequency 7mHz and mode $\ell = 20$ (i.e., frequency above cut-off). With Approach 2, we solve two problems following [Algorithm 1](#), and use $r_{\min} = 0.60$ and $r_b = r_{\max} = 1.0008$. For Approach 1, one needs to solve one problem per source, on the whole interval, i.e., 4001 simulations.

Table 5: Mean of the relative difference between radiation conditions in $r_{\max} = 1.0008$ and a reference solution computed on $(0, 5)$ with Dirichlet condition. The computations use either the conjugated or original equation, with attenuation $\Gamma/(2\pi) = 20\mu\text{Hz}$.

RBC	original equation			conjugated equation		
	2mHz, $\ell=0$	2mHz, $\ell=20$	2mHz, $\ell=200$	2mHz, $\ell=0$	2mHz, $\ell=20$	2mHz, $\ell=200$
Z_{NL}^ℓ	n/a	n/a	n/a	3.21×10^{-9}	4.50×10^{-9}	2.10×10^{-7}
$Z_{\text{aNL-G}}^\ell$	4.40×10^{-9}	9.10×10^{-9}	3.82×10^{-5}	3.36×10^{-9}	6.73×10^{-9}	3.05×10^{-7}
Z_{aNL}^ℓ	8.04×10^{-6}	9.66×10^{-6}	4.25×10^{-5}	8.04×10^{-6}	9.66×10^{-6}	4.77×10^{-6}
$Z_{\text{S-HFG-0}}$	1.44×10^{-6}	4.46×10^{-6}	1.64×10^{-4}	1.44×10^{-6}	4.47×10^{-6}	1.27×10^{-4}
$Z_{\text{S-HFG-1}}$	3.98×10^{-9}	2.72×10^{-6}	1.63×10^{-4}	2.93×10^{-9}	2.73×10^{-6}	1.26×10^{-4}
$Z_{\text{S-HFG-2}}^\ell$	2.01×10^{-9}	4.65×10^{-9}	3.86×10^{-5}	9.55×10^{-10}	2.32×10^{-9}	8.37×10^{-7}
$Z_{\text{S-HFG-3}}^\ell$	2.04×10^{-9}	4.68×10^{-9}	3.86×10^{-5}	9.82×10^{-10}	2.35×10^{-9}	8.37×10^{-7}
$Z_{\text{S-HF-0}}$	9.49×10^{-6}	1.41×10^{-5}	1.69×10^{-4}	9.48×10^{-6}	1.41×10^{-5}	1.32×10^{-4}
$Z_{\text{S-HF-1}}$	8.04×10^{-6}	1.24×10^{-5}	1.68×10^{-4}	8.03×10^{-6}	1.24×10^{-5}	1.31×10^{-4}
$Z_{\text{S-HF-2}}^\ell$	8.04×10^{-6}	9.66×10^{-6}	4.32×10^{-5}	8.04×10^{-6}	9.66×10^{-6}	5.53×10^{-6}
$Z_{\text{S-HF-3}}^\ell$	8.04×10^{-6}	9.66×10^{-6}	4.32×10^{-5}	8.04×10^{-6}	9.66×10^{-6}	5.53×10^{-6}
$Z_{\text{G-LR}}$	6.38×10^{-9}	2.72×10^{-6}	1.63×10^{-4}	5.35×10^{-9}	2.72×10^{-6}	1.26×10^{-4}
$Z_{\text{aNL-G}}^0$	6.38×10^{-9}	2.72×10^{-6}	1.63×10^{-4}	5.35×10^{-9}	2.72×10^{-6}	1.26×10^{-4}
Z_{aNL}^0	8.04×10^{-6}	1.24×10^{-5}	1.68×10^{-4}	8.03×10^{-6}	1.24×10^{-5}	1.31×10^{-4}
$Z_{\text{S-G}}$	1.44×10^{-6}	4.46×10^{-6}	1.64×10^{-4}	1.44×10^{-6}	4.46×10^{-6}	1.27×10^{-4}
$Z_{\text{SAI-0}}$	8.04×10^{-6}	1.24×10^{-5}	1.68×10^{-4}	8.03×10^{-6}	1.24×10^{-5}	1.31×10^{-4}
$Z_{\text{SAI-1}}^\ell$	8.04×10^{-6}	9.66×10^{-6}	4.32×10^{-5}	8.04×10^{-6}	9.66×10^{-6}	5.52×10^{-6}
$Z_{\text{SAI-2}}^\ell$	8.04×10^{-6}	9.66×10^{-6}	4.25×10^{-5}	8.04×10^{-6}	9.66×10^{-6}	4.78×10^{-6}
$Z_{\text{aW-4}}^\ell$	8.04×10^{-6}	9.66×10^{-6}	4.25×10^{-5}	8.04×10^{-6}	9.66×10^{-6}	4.82×10^{-6}
$Z_{\text{aW-1}}^\ell$	2.86×10^{-9}	2.96×10^{-6}	1.74×10^{-4}	1.81×10^{-9}	2.96×10^{-6}	1.37×10^{-4}

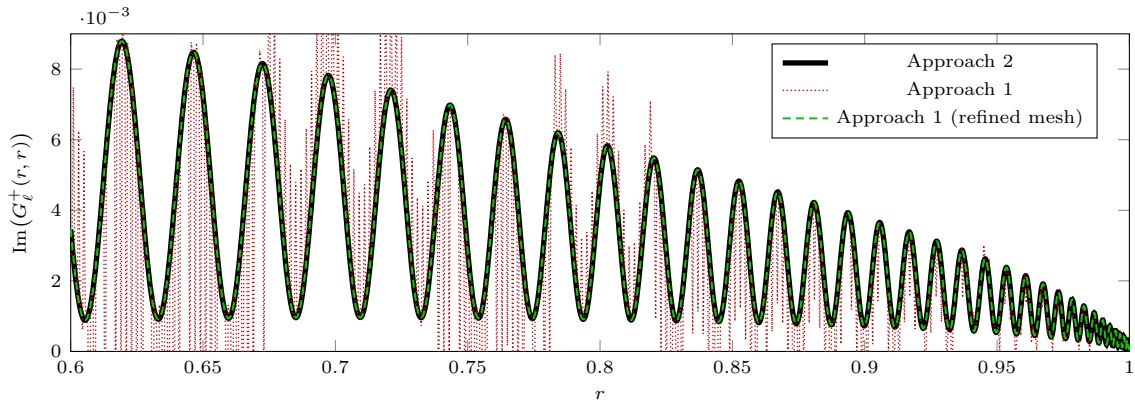


Figure 26: Imaginary part of the Green's kernel $G_\ell^+(r, r)$ at 7mHz for $\ell = 20$ depending on the approaches. Approach 2 uses two simulations to assemble the kernel while Approach 1 needs one computation for each of the 4001 sources. In the refined mesh, the size of each segment of the original mesh is divided by 8 (from 4×10^{-4} to 5×10^{-5}).

When we use the same discretization mesh for the two approaches, we see that the solution is noisy and unusable for Approach 1 at the position where $r = s$, due to the Dirac singularity at the source position, cf. Figure 26. We need to refine the mesh near the position of the sources (here dividing the

size by 8) to obtain the accurate solution. Therefore, not only Approach 2 is computationally cheaper by avoiding the resolution of a problem for each source, but it is also more accurate by avoiding the discretization of the Dirac singularity. This was also observed for the scalar case in [3]. We further illustrate the global kernel G_ℓ^+ obtained with Approach 2 in Figure 27.

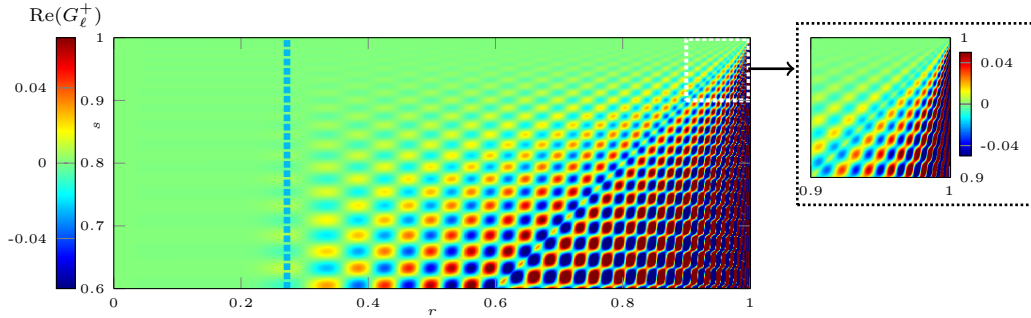
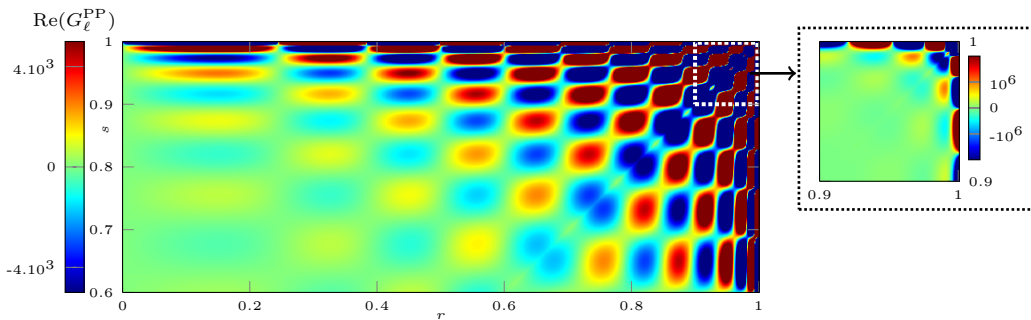


Figure 27: Real part of the Green's kernel G_ℓ^+ at 7mHz for $\ell = 20$. The position of r^* is indicated by the vertical dashed line in cyan. For visualization, zoomed pictures in the interval $[0.9, 1] \times [0.9, 1]$ are shown on the right.

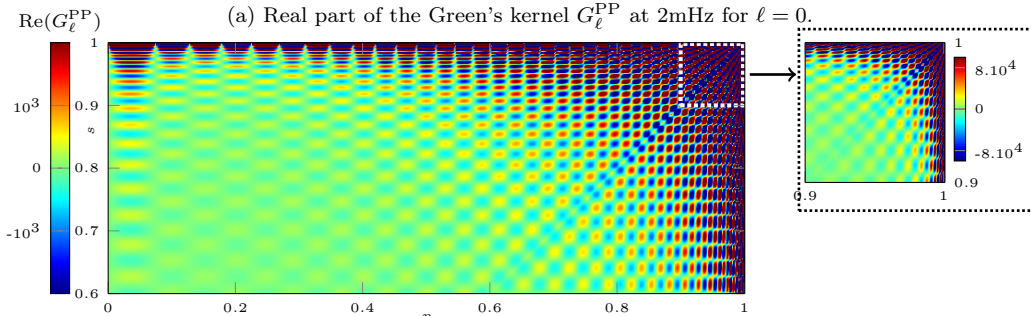
We see that the highest amplitudes correspond to the surface, as observed in Subsection 7.2. Here, the waves are evanescent in the interior, starting right after r^* , as illustrated in the corresponding potential of Figure 11. Here, the kernel is assembled from 2 simulations using Approach 2, whatever number of sources one wants to have.

7.4.2 Comparison of the vector modal Green's kernels

In Figures 28 to 30, we picture the Green's kernels G_ℓ^{PP} for modes $\ell = 0$, $\ell = 20$ and $\ell = 200$ respectively. The kernels are assembled from 2 simulations with Approach 2 (Algorithm 1) using $r_{\min} = 0.60$ and $r_b = r_{\max} = 1.0008$.



(a) Real part of the Green's kernel G_ℓ^{PP} at 2mHz for $\ell = 0$.



(b) Real part of the Green's kernel G_ℓ^{PP} at 7mHz for $\ell = 0$.

Figure 28: Comparison of the Green's kernel G_ℓ^{PP} at mode $\ell = 0$ for different frequencies. For visualization, zoomed pictures in the interval $[0.9, 1] \times [0.9, 1]$ are shown on the right using a different scaling.

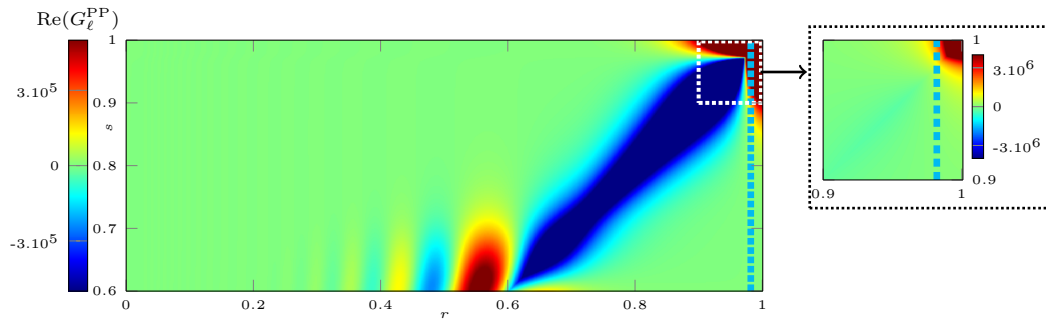
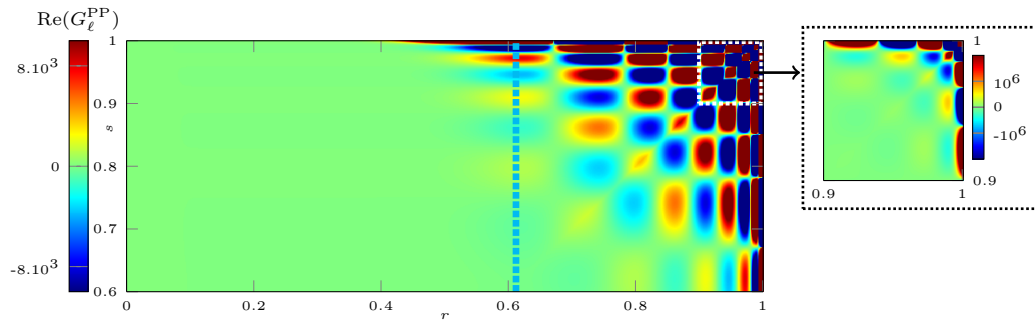
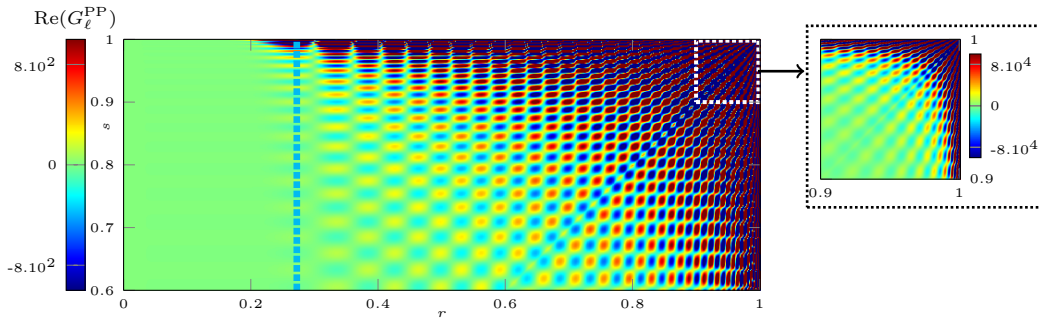
(a) Real part of the Green's kernel G_ℓ^{PP} at 0.2mHz for $\ell = 20$.(b) Real part of the Green's kernel G_ℓ^{PP} at 2mHz for $\ell = 20$.(c) Real part of the Green's kernel G_ℓ^{PP} at 7mHz for $\ell = 20$.

Figure 29: Comparison of the Green's kernel G_ℓ^{PP} at mode $\ell = 20$ for different frequencies. The position of r^* is indicated by the vertical dashed line in cyan. For visualization, zoomed pictures in the interval $[0.9, 1] \times [0.9, 1]$ are shown on the right using a different scaling.

One can observe the symmetry of the kernel $G_\ell^{\text{PP}}(r, s) = G_\ell^{\text{PP}}(s, r)$. Moreover, waves with low harmonic degrees are traveling further away from the source than high-degree modes. Namely, at mode $\ell = 0$, Figure 28, waves are able to reach the origin. At mode $\ell = 20$, Figure 29, waves do not reach the origin, and high-frequency waves are able to reach deeper region than low-frequency ones, in particular as r^* is deeper for high frequencies. We observe the same behaviour at mode $\ell = 200$, Figure 29, where the waves are now mostly concentrated near the surface, in particular at 2mHz frequency. For the mode $\ell = 20$ and frequency 0.2mHz, Figure 29a, we observe a patch of high amplitude in the interior (for $r \in (0.4, 0.6)$), that appears when the source is near the radiative zone. This corresponds to the part where the potential is negative in the interior in Figure 8, which is only for sufficiently low frequency (below the Brunt-Väisälä limit in the interior).

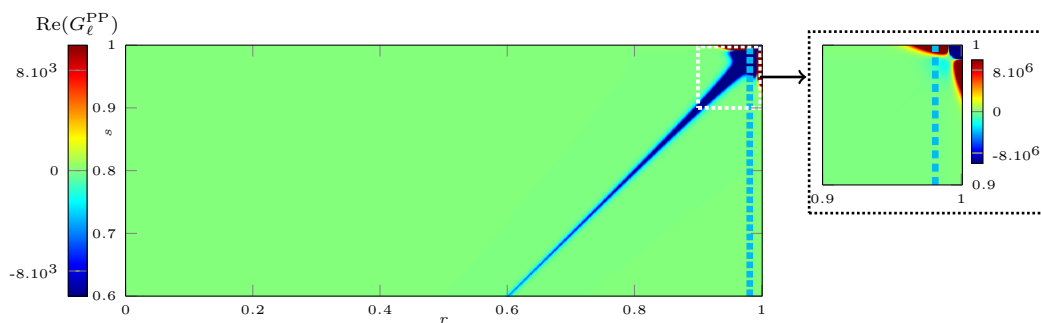
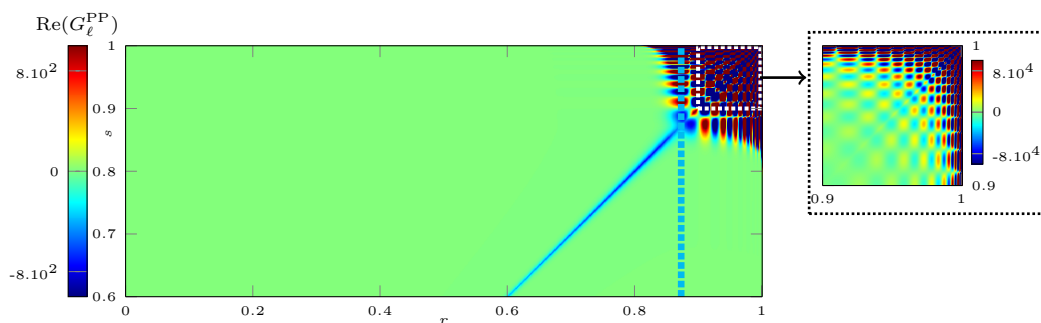

 (a) Real part of the Green's kernel G_ℓ^{PP} at 2mHz for $\ell = 200$.

 (b) Real part of the Green's kernel G_ℓ^{PP} at 7mHz for $\ell = 200$.

Figure 30: Comparison of the Green's kernel G_ℓ^{PP} at mode $\ell = 200$ for different frequencies. When it lies in the interval, the position of r^* is indicated by the vertical dashed line in cyan. For visualization, zoomed pictures in the interval $[0.9, 1] \times [0.9, 1]$ are shown on the right using a different scaling.

In addition to G_ℓ^{PP} , Approach 2 allows us to assemble the other kernels, e.g., G_ℓ^{BP} and G_ℓ^{BBreg} , from the same two simulations, see Algorithm 1. In Figure 31, we compare those kernels at frequency 7mHz for mode $\ell = 20$. In particular, all of these kernels are necessary to reconstruct the 3D wave displacement.

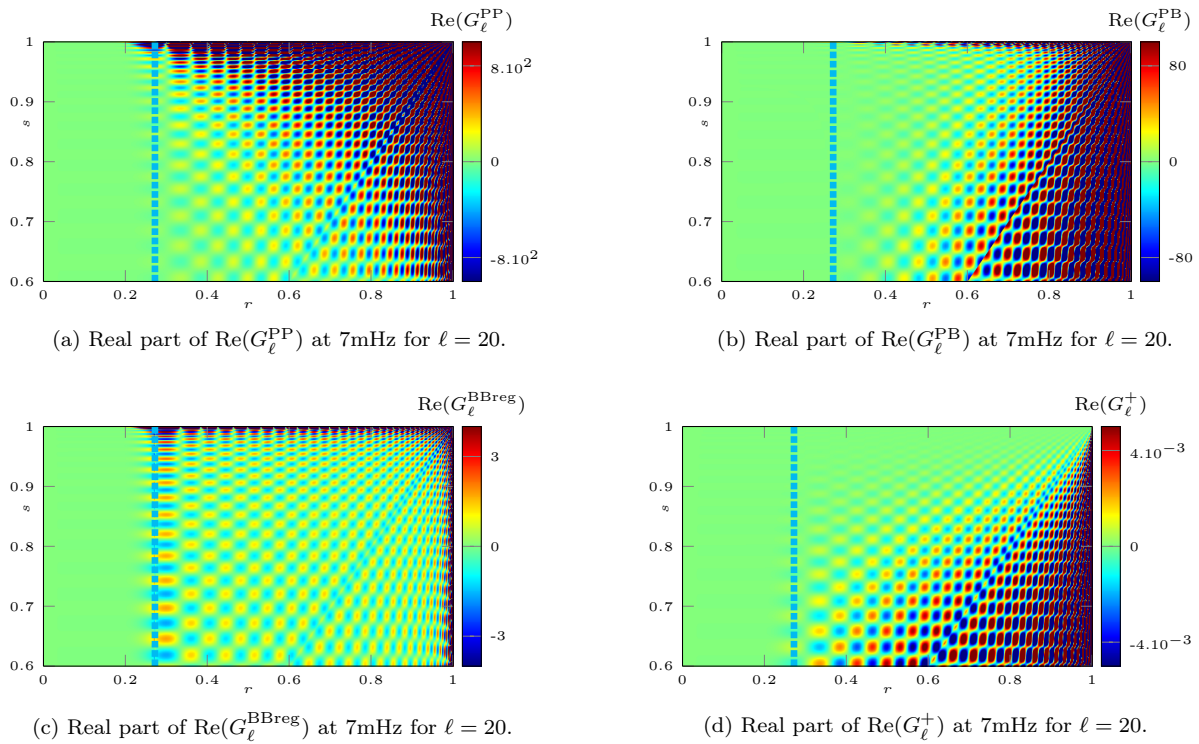


Figure 31: Comparison of the Green's kernels at frequency 7 mHz for mode $\ell = 20$. The position of r^* is indicated by the vertical dashed line in cyan.

7.5 Multi-frequency, multi-modal representations

7.5.1 Experiments at fixed mode and different levels of attenuation

In this section, we consider a fixed mode, and plot the solutions for all frequencies, comparing for different positions of sources and receivers. In Figures 32 and 33 we picture the Green's kernel G_ℓ^{PP} for mode $\ell = 10$ and $\ell = 750$ respectively. We consider frequencies between 1 μ Hz and 7mHz and a source positioned in $s = 0.65$ or $s = 1$. For the position of the RBC, we first select $r_{\text{max}} = 1.2$ to ensure the accuracy of the computations, in particular for the low frequencies at mode $\ell = 750$.

For the relatively low mode $\ell = 10$ (Figure 32), waves are able to propagate in the domain, whether the source is in 1 or 0.65. The wave amplitude decreases near the origin, except for low-frequencies below the Brunt-Väisälä frequency, this region corresponds to the part where the potential is negative in the interior, cf. Subsection 7.1. For the higher mode, $\ell = 750$ in Figure 33, we observe that now the high amplitude is localized near the position of the source, and decreases extremely rapidly as soon as it moves away (one hundred orders of magnitude). However, similarly to the lower modes, the waves of low frequencies below the Brunt-Väisälä one are able to propagate in the interior.

In Figures 34 and 35, we picture the amplitude of G_ℓ^{PP} for a given source and receiver positions, with all frequencies. We see peaks in the solution, with width depending on the level of attenuation, namely with sharper peaks when the attenuation is low. Comparing the modes, there are more peaks at low modes, while only a few are observed for $\ell = 750$ in Figure 35. In addition, we observe that several peaks appear in the low frequency regime, which are very close to each other. A low level of attenuation is necessary to distinguish the different peaks.

In Figure 36, we picture the solutions restricted to the low-frequencies, where we also compare the solutions given with the RBC either positioned in $r_{\text{max}} = 1.2$ or $r_{\text{max}} = 1.0008$. As highlighted in Subsection 7.3, above the cut-off frequency, the solution given with the RBC in $r_{\text{max}} = 1.0008$ accurately describes the behaviour, and we cannot distinguish the two solutions in Figure 36a. In particular, the peaks are located at the same frequencies.

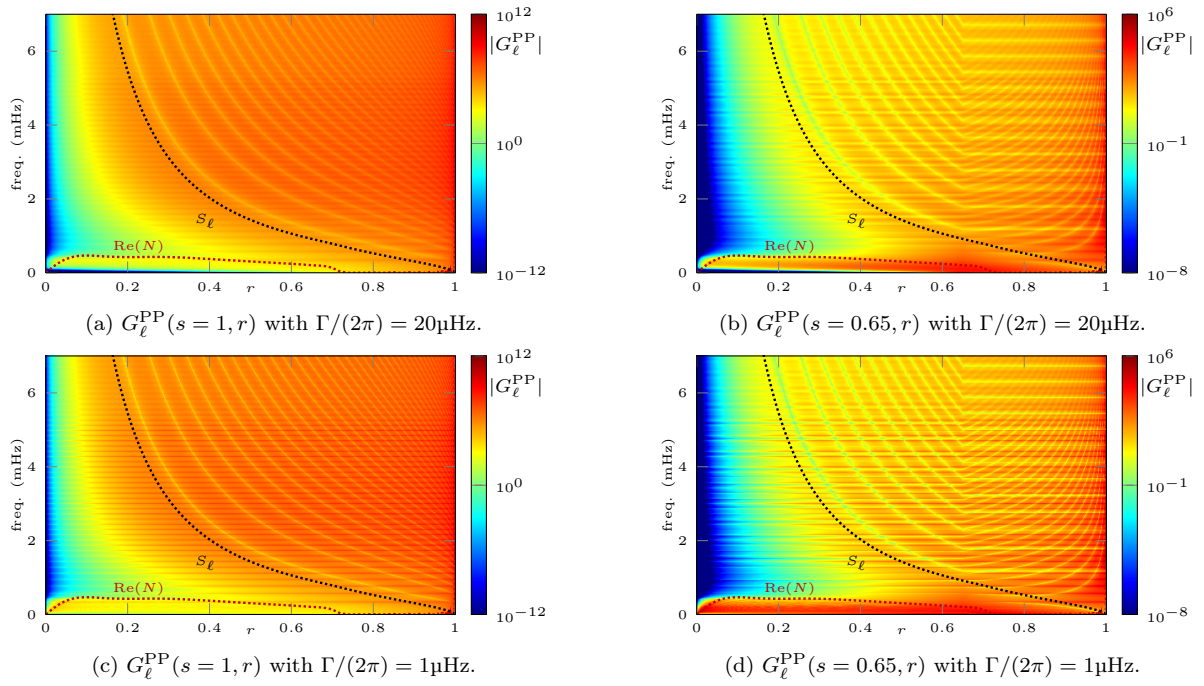


Figure 32: Norm of the Green's kernel G_ℓ^{PP} at mode $\ell = 10$ with frequency and position of the receivers, for a source positioned in $s = 0.65$ or $s = 1$. The Brunt-Väisälä N and Lamb frequencies S_ℓ are pictured with dashed lines. The computations use $r_{\text{max}} = 1.2$.

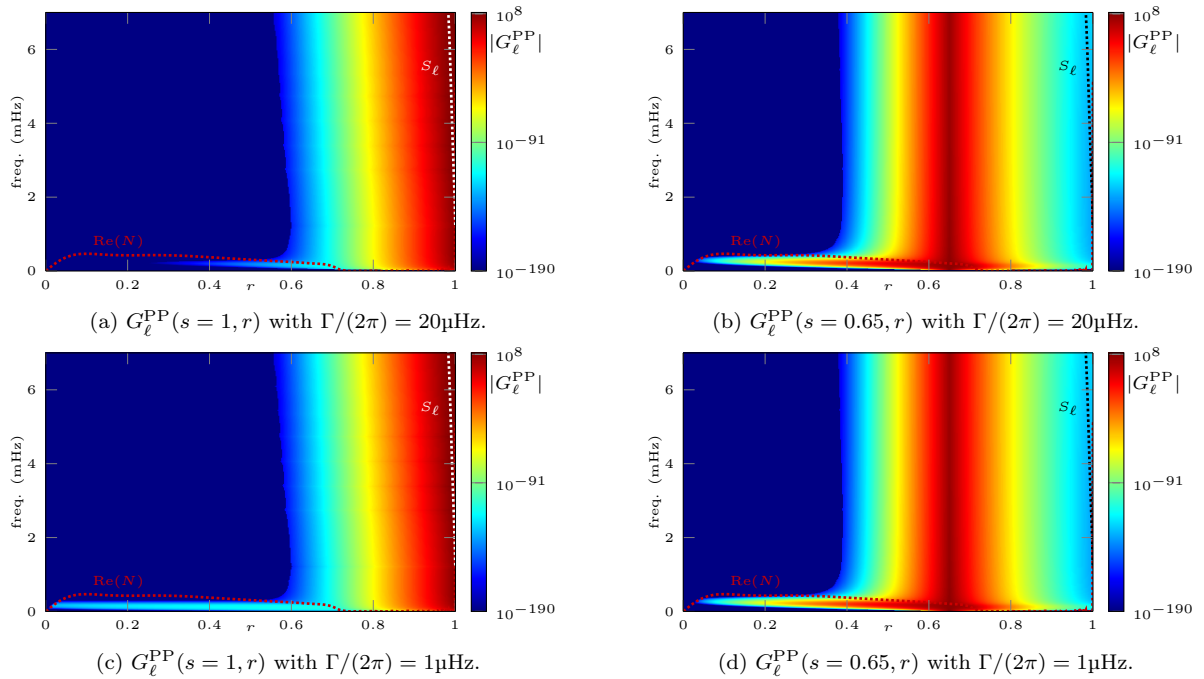


Figure 33: Norm of the Green's kernel G_ℓ^{PP} at mode $\ell = 750$ with frequency and position of the receivers, for a source positioned in $s = 0.65$ or $s = 1$. The Brunt-Väisälä N and Lamb frequencies S_ℓ are pictured with dashed lines. The computations use $r_{\text{max}} = 1.2$.

Nonetheless, for the higher mode, with frequency below the cut-off, we observe major differences

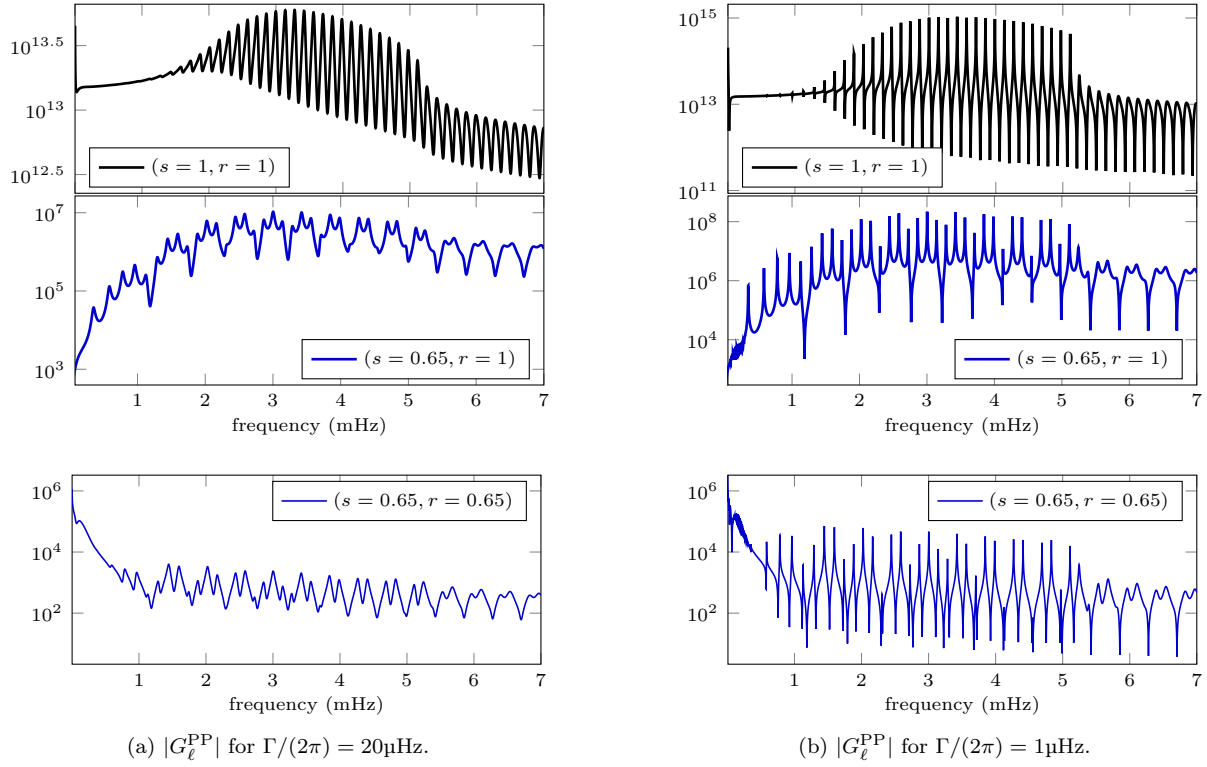


Figure 34: Norm of the Green's kernel $|G_\ell^{\text{PP}}|$ at mode $\ell = 10$ for different positions of source and receiver. The computations use $r_{\max} = 1.2$ and different level of attenuation.

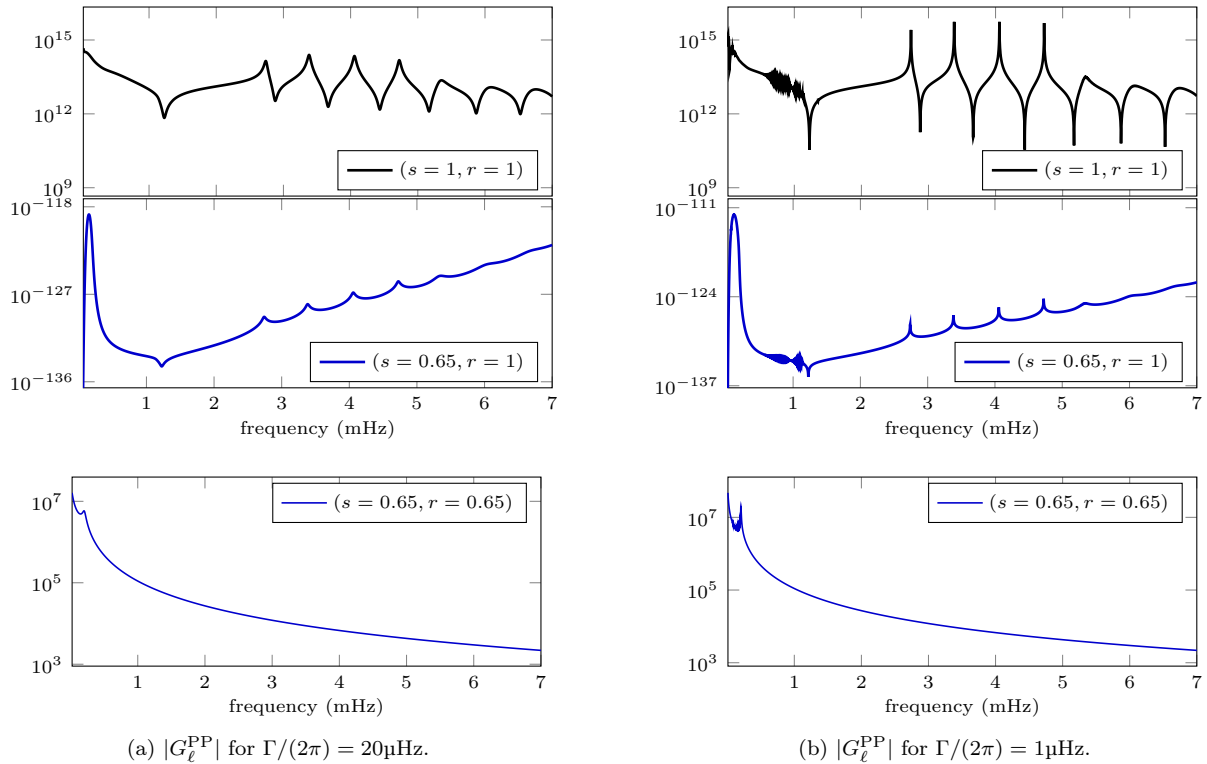


Figure 35: Norm of the Green's kernel $|G_\ell^{\text{PP}}|$ at mode $\ell = 750$ for different positions of source and receiver. The computations use $r_{\max} = 1.2$ and different level of attenuation.

between the solution, in particular at low level of attenuation, see Figures 36b and 36d. Many peaks appear when the RBC is positioned too close to the surface, which could be interpreted erroneously as atmospheric modes.

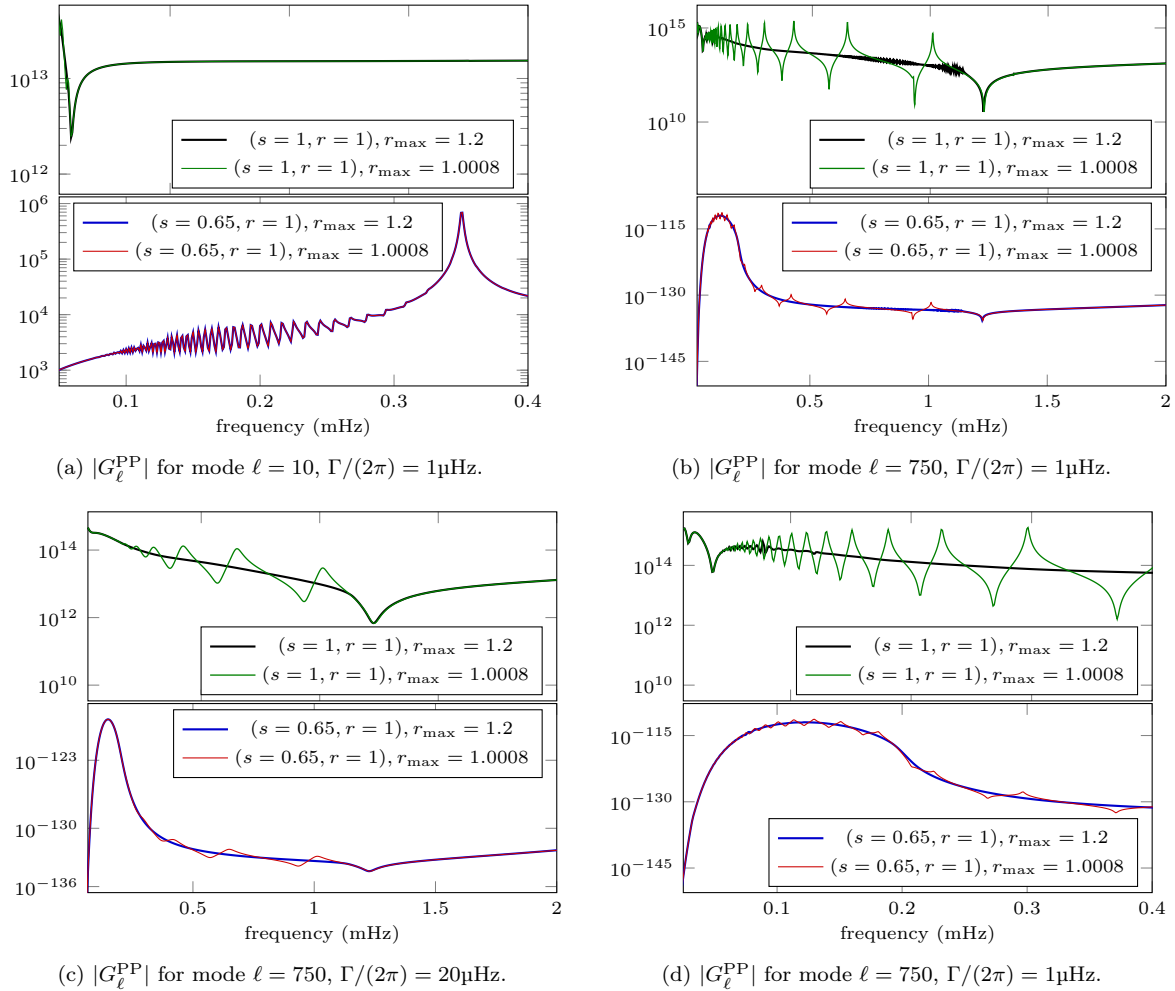


Figure 36: Norm of the Green's kernel $|G_\ell^{\text{PP}}|$ at low frequency, comparing the use of $r_{\text{max}} = 1.0008$ and $r_{\text{max}} = 1.2$ for the consideration of the RBC.

7.5.2 Experiments with all modes

We now picture the Green's kernels G_ℓ^{PP} , G_ℓ^{BP} and G_ℓ^{BBreg} for all modes and frequencies, at a fixed position (s, r) . In Figure 37, we fix the source in $s = 1$ and show the resulting kernels for two receiver heights: 1 and 0.9. The computations use attenuation $\Gamma/(2\pi) = 20\mu\text{Hz}$. Here we consider the RBC close to the surface, in $r_{\text{max}} = 1.0008$. Therefore, following our above results, only sufficiently high frequencies are accurately described, hence we only consider frequencies higher than 2 mHz.

In Figure 38, we picture the Green's kernel for low-frequencies, where we compare the solution obtained with the RBC either in $r_{\text{max}} = 1.20$ or $r_{\text{max}} = 1.0008$. We see that at the surface, $s = r = 1$, the ridges appear if the RBC is positioned too close to the atmosphere, while they disappear when it is positioned sufficiently far from the surface. In addition, we see that these ridges appear in all of the kernels. We note that while G_ℓ^{PP} and G_ℓ^{BBreg} maintain the same amplitude, G_ℓ^{BP} has less intensity when the RBC is positioned too close to the surface. As depicted in Subsection 7.1, the case where the RBC has to be moved away from the surface corresponds to low-frequency below the cut-off and Lamb frequency, which is confirmed by Figure 38, where the extra-ridges only appear for frequencies below S_ℓ . In the case where the positions investigated are deeper in the interior, e.g., $s = r = 0.65$ in Figures 38g and 38h, there is

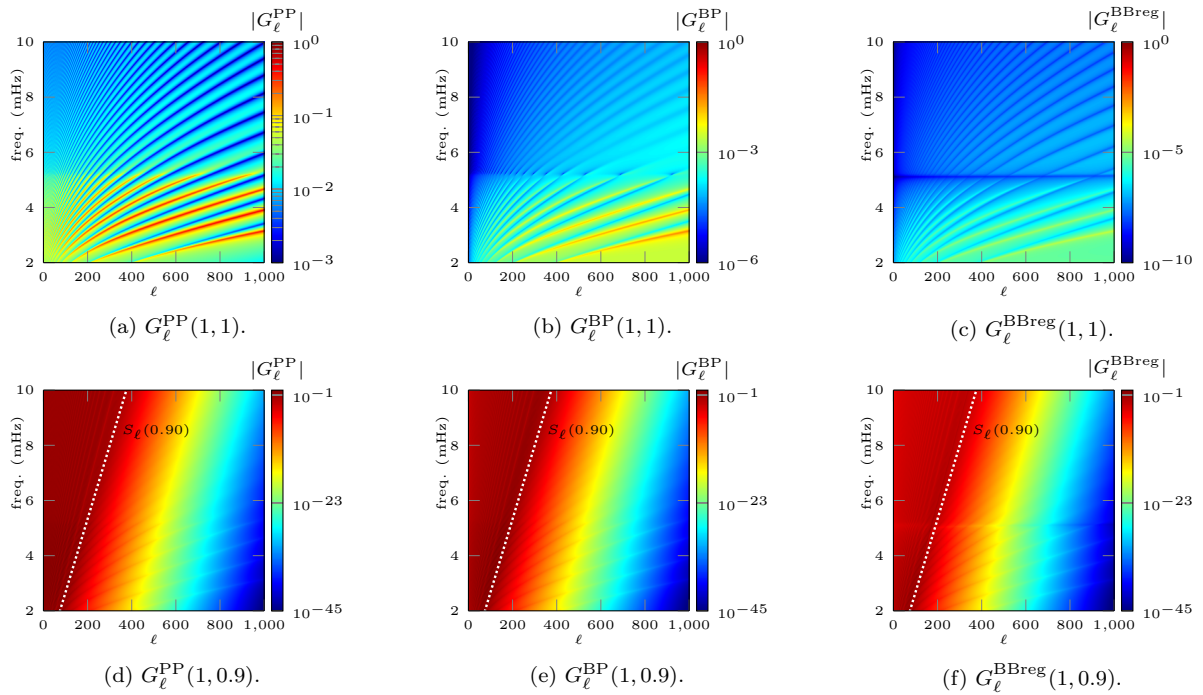


Figure 37: Green's kernels for fixed source in $s = 1$ and different receiver positions (1 and 0.9). The mode varies from 0 to 1000 and the frequency with step $25\mu\text{Hz}$ up to 10mHz . The position of the RBC is in $r_{\max} = 1.0008$, such that we only picture for frequencies higher than 2 mHz , where the accuracy is guaranteed. We use attenuation $\Gamma/(2\pi) = 20\mu\text{Hz}$. The absolute value is pictured, with each kernel individually normalized with its respective maximal value.

no more difference in the simulations, as the position is sufficiently far away from the difficulty of the atmosphere.

7.6 Concluding remarks

Here we give some remarks to summarize our numerical experiments.

1. The conjugated equation gives a symmetric formulation for the discretization, however, one needs to refine near the position of r^* to capture the behaviour of the solution with low level of attenuation, while it is inaccurate without attenuation. The original equation does not give a symmetric discretized problem, but is stable in all cases, as it avoids the singular behaviour in r^* .
2. Regarding the radiation boundary conditions:
 - The RBC can be efficient when positioned near the atmosphere (in $r_{\max} = 1.0008$), except for frequencies below both the cut-off and the atmospheric Lamb frequencies. It corresponds to low-frequencies and high-degree modes. In this case, the potential exhibits the profile of a well after the surface, and one should instead consider $r_{\max} \geq 1.2$ to ensure accuracy of the numerical truncation. This is problematic as our isothermal atmospheric model is only realistic until the end of the photosphere corresponding to $r = 1.003$. The study of these waves should thus be done by considering an atmospheric model or adding additional physical phenomena.
 - The consideration of the gravity term in the expression of the RBC allows to gain about 3 orders of magnitude in terms of accuracy.
3. The Green's kernels are efficiently assembled using our Approach 2 given by Algorithm 1, which allows to construct all of the kernels using two simulations only. In addition, the method avoids the difficulty of having to discretize a Dirac source. Furthermore, using the HDG method for the discretization is particularly appropriate as it solves the first-order formulation and readily

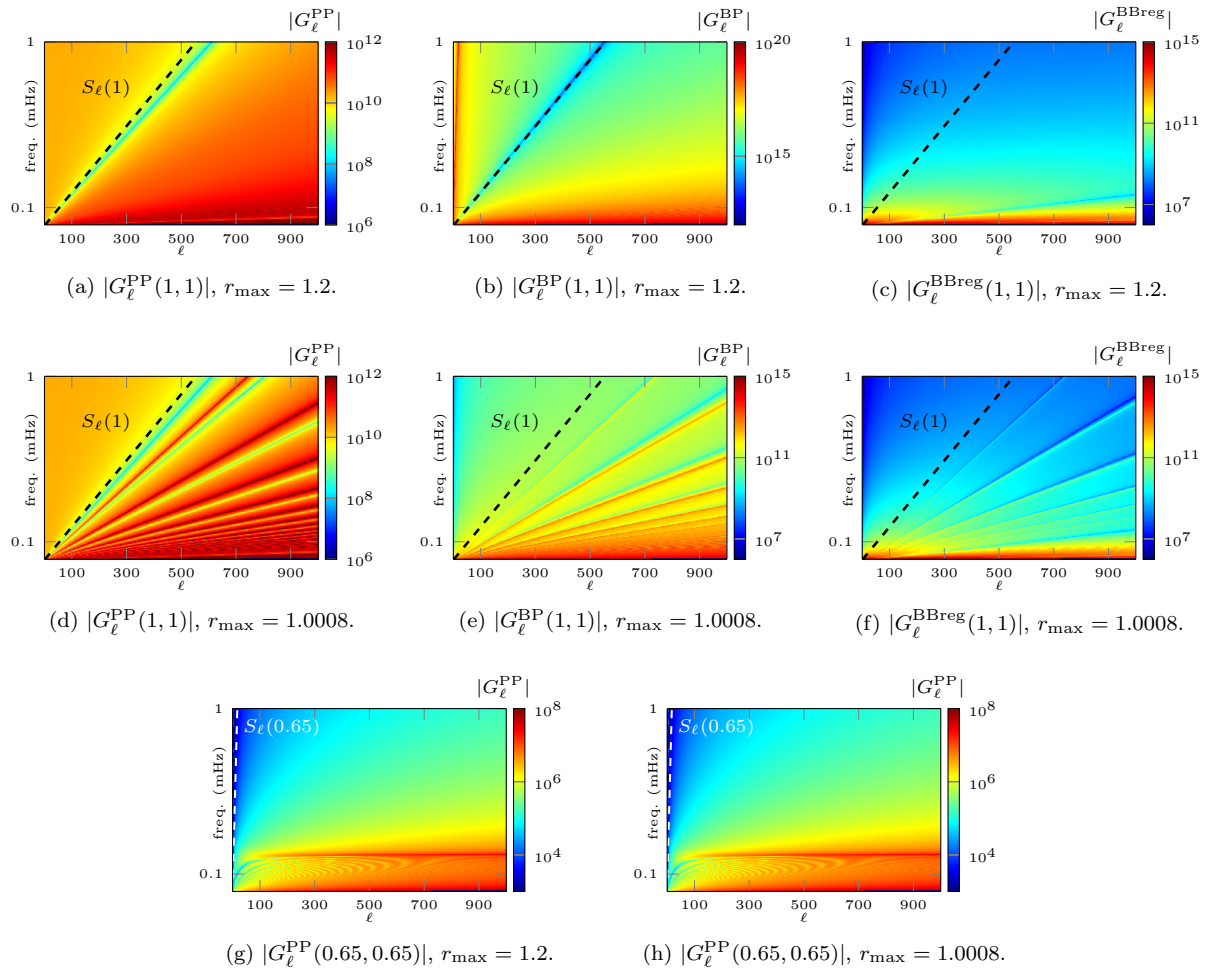


Figure 38: Green's kernels for fixed source and receiver position, with either $s = r = 1$ or $s = r = 0.65$ and using different position of r_{max} for simulations, corresponding to where the RBC is imposed. The mode varies from 0 to 1000 and the frequency with step from $5\mu\text{Hz}$ up to 1mHz . We use attenuation $\Gamma/(2\pi) = 1\mu\text{Hz}$.

gives all of the components to assemble the kernels (i.e., the regular solutions and their first-order derivatives).

4. The Green's kernels associated with the vector-wave problem and solar background models show the low-frequencies gravity modes, which are not acknowledged in the scalar-wave problem. In addition, these kernels give access to the full vector displacement which will allow for a better modeling of the solar observations.

8 Conclusion

In this work, we developed an efficient numerical methodology associated with the theoretical results obtained in [6, 5]. We have derived two formulations for the equations, the 'original' and 'conjugated' ones. The conjugated one directly works with the potential V_ℓ , and gives a symmetric discretization matrix. On the other hand, it is not able of treating the case without attenuation and, for low level of attenuation, the discretization must be refined near r^* so that the solution is accurately captured.

Our work extends the algorithm for computing modal Green's kernel for the scalar wave operator of [3] to the vector operator (1.1). It allows us to assemble all of the vector Green's kernels (G_ℓ^{PP} , G_ℓ^{BP} ,

G_ℓ^{BBreg}) with two simulations, while avoiding the singularity of having a Dirac source as the right-hand side. Here, the HDG method used for the implementation is particularly appropriate as it readily gives the derivatives of the regular solutions which are needed to assemble the kernels. Therefore, we have deployed an efficient and accurate algorithm for the computation of the vector Green's kernel, which will serve to obtain the full vector displacement to compare with solar observations.

For the truncation of the computational domain, we have provided several formulations of RBC, and have shown that including the gravity term, while being of order r^{-3} , leads to a drastic improvement in terms of accuracy. Nonetheless, for the solar case, for low frequencies and high modes, the potential in the low atmosphere has the profile of a well. That requires the RBC to be pushed further out (namely, from $r = 1.0008$ for frequencies above the cut-off one, to $r = 1.2$). In this case, it is in fact necessary to adapt our atmospheric solar model which only accounts for phenomena up to the photosphere, that is, up to $r = 1.003$. This is the subject of ongoing work.

Acknowledgments

This work is supported by the INRIA associated-team Ants (Advanced Numerical meThods for helio-Seismology). FF is funded by the Austrian Science Fund (FWF) under the Lise Meitner fellowship M 2791-N. DF and LG acknowledge funding by the Deutsche Forschungsgemeinschaft (DFG, German Research Foundation) – Project-ID 432680300 – SFB 1456.

A Numerical computation working with conjugated equation \mathcal{L}_ℓ

In this appendix, we briefly discuss how to use \mathcal{L}_ℓ to compute the quantities (5.1) as an alternative to \mathfrak{L}_ℓ as discussed in Section 5.

A.1 Coefficients of the Green's kernels using the conjugated equation

We recall the definition of the coefficients of the 3D Green's kernels,

$$a_\ell^m = R_\odot^2 \int_0^\infty G_\ell^{\text{PP}}(r, s) f_\ell^m(s) s^2 ds + R_\odot^2 \int_0^\infty G_\ell^{\text{PB}}(r, s) g_\ell^m(s) s^2 ds; \quad (\text{A.1a})$$

$$b_\ell^m = R_\odot^2 \int_0^\infty G_\ell^{\text{BP}}(r, s) f_\ell^m(s) s^2 ds + R_\odot^2 \int_0^\infty G_\ell^{\text{BB}}(r, s) g_\ell^m(s) s^2 ds, \quad (\text{A.1b})$$

Recall that \mathcal{G}_ℓ^+ is the regular-at-zero and outgoing-at-infinity Green's kernel of \mathcal{L}_ℓ ,

$$\left(-\partial_r^2 + V_\ell\right) \mathcal{G}_\ell^+(r, s) = \delta(r - s). \quad (\text{A.2})$$

We recall K_ℓ defined in (3.85),

$$K_\ell(r, s) := \frac{1}{r c_0(r) \rho_0^{1/2}(r) s c_0(s) \rho_0^{1/2}(s)} \frac{\sqrt{F_\ell(s)} \sqrt{F_\ell(r)}}{\sqrt{F_0(s)} \sqrt{F_0(r)}}. \quad (\text{A.3})$$

We also define

$$\mathfrak{z}_\ell(r) := \frac{r \ell(\ell + 1) \mathfrak{t}_\ell(r) - r \eta(r) + 2}{2}, \quad (\text{A.4})$$

Similarly to Proposition 1, in the following proposition, we compute the $G_\ell^{\bullet\bullet}$ coefficients now in terms of K_ℓ and \mathcal{G}_ℓ^+ .

Proposition 3. With K_ℓ and \mathfrak{z}_ℓ defined in (A.3) and (A.4), we have

$$G_\ell^{\text{PP}}(r, s) = K_\ell(r, s) \mathcal{G}_\ell^+(r, s) = \frac{G_\ell^+(r, s)}{c_0^2(s) \rho_0(s) s^2}, \quad (\text{A.5a})$$

$$G_\ell^{\text{PB}}(r, s) = -K_\ell(r, s) \frac{\sqrt{\ell(\ell+1)}}{F_\ell(s)} (s \partial_s \mathcal{G}_\ell^+(r, s) + \mathcal{G}_\ell^+(r, s) \mathfrak{z}_\ell(s)), \quad (\text{A.5b})$$

and

$$\begin{aligned} G_\ell^{\text{BP}}(r, s) &= -K_\ell(r, s) \frac{\sqrt{\ell(\ell+1)}}{F_\ell(r)} (r \partial_r \mathcal{G}_\ell^+(r, s) + \mathcal{G}_\ell^+(r, s) \mathfrak{z}_\ell(r)); \\ G_\ell^{\text{BB}}(r, s) &= +K_\ell(r, s) \frac{\ell(\ell+1)}{F_\ell(r) F_\ell(s)} [(r \partial_r)(s \partial_s) \mathcal{G}_\ell^+(r, s) + \mathcal{G}_\ell^+(r, s) \mathfrak{z}_\ell(r) \mathfrak{z}_\ell(s) \\ &\quad + \mathfrak{z}_\ell(s) r \partial_r \mathcal{G}_\ell^+(r, s) + \mathfrak{z}_\ell(r) s \partial_s \mathcal{G}_\ell^+(r, s)] \\ &\quad - \frac{r^2}{F_\ell(r) \gamma(r) p_0(r)} \frac{\delta(r-s)}{s^2}. \end{aligned} \quad (\text{A.6})$$

A.2 Implementation of the HDG method for \mathcal{L}_ℓ

A.2.1 Boundary conditions

- **Condition at $r = 0$.** The function \mathcal{G}_ℓ^+ is regular at $r = 0$ with exponent κ_ℓ^+ where, cf. [6, Eqn (5.20) Proposition 8],

$$\kappa_0^+ = 2, \quad \kappa_0^- = -1; \quad \kappa_\ell^+ = \ell + 1, \quad \kappa_\ell^- = -\ell, \quad \text{for } \ell > 0. \quad (\text{A.7})$$

For $\ell > 0$, these are the same indicial indices as the ones of the modal Green's kernel considered in [3, Section 3.2.1]. For $\ell \geq 0$, the 'regular-at-zero' solution is chosen by

$$\boxed{\lim_{r \rightarrow 0} r \partial_r \frac{\mathcal{G}_\ell^+}{r} = 0.} \quad (\text{A.8})$$

- **Condition at r_{\max} .** Considering the RBC coefficient \mathcal{Z}_\bullet given in Section 6, the outgoing characterization at infinity is approximated by

$$\boxed{(\partial_r \mathcal{G}_\ell^+)(r_{\max}) = i \mathcal{Z}_\bullet(r_{\max}) \mathcal{G}_\ell^+(r_{\max}).} \quad (\text{A.9})$$

Remark 20. Note that at $\ell = 0$ the indicial root is different from those in [3], however we can verify quickly that the above condition also selects the regular solution at level $\ell = 0$. The division by r is needed to distinguish regular from irregular solutions at level $\ell = 1$, at which level both solutions have nonnegative indicial roots. This division will not be needed or in fact cannot be imposed for G_ℓ^+ , see Remark 14. \diamond

We will work under the assumption of attenuation

$$\Gamma > 0, \quad (\text{A.10})$$

which is necessary in terms of computations, as highlighted in Subsection 7.2.

A.2.2 Direct and assembling methods

Approach 1. On $[0, r_{\max}]$ one solves directly for \mathcal{G}_ℓ^+ as a solution to

$$(-\partial_r^2 + V_\ell) \mathcal{G}_\ell^+ = \delta(r-s); \quad (\text{A.11a})$$

$$\lim_{r \rightarrow 0} r \left(\frac{\mathcal{G}_\ell^+}{r} \right)' = 0, \quad (\partial_r \mathcal{G}_\ell^+)(r_{\max}) = i \mathcal{Z}_\bullet(r_{\max}) \mathcal{G}_\ell^+(r_{\max}). \quad (\text{A.11b})$$

Approach 2. Using the same technique as in [3] (in particular Algorithm 3.2), we first solve for a solution in the ‘regular-at-zero’ family: chosen as

$$(-\partial_r^2 + V_\ell) \varphi_\ell = 0; \quad (\text{A.12a})$$

$$\lim_{r \rightarrow 0} r \left(\frac{\varphi_\ell}{r} \right)' = 0, \quad \varphi_\ell(r_b) = 1, \quad (\text{A.12b})$$

with $r_b \leq r_{\max}$. We then find a solution in the ‘outgoing-at-infinity’ family, chosen as

$$(-\partial_r^2 + V_\ell) \varphi_\ell^+ = 0; \quad (\text{A.13a})$$

$$\varphi^+(r_{\min}) = 1, \quad (\partial_r \varphi^+)(r_{\max}) = i \mathcal{Z}_\bullet(r_{\max}) \varphi_\ell^+(r_{\max}), \quad (\text{A.13b})$$

with $r_{\min} > 0$. The outgoing Green’s function \mathcal{G}_ℓ^+ is given by,

$$\mathcal{G}_\ell^+(r, s) := -\frac{\mathbf{H}(s-r) \varphi_\ell(r) \varphi_\ell^+(s) + \mathbf{H}(r-s) \varphi_\ell(s) \varphi_\ell^+(r)}{\mathbf{W}_\ell^+}. \quad (\text{A.14})$$

A.2.3 First-order formulation

The quantities \mathcal{G}_ℓ^+ , φ_ℓ and φ_ℓ^+ satisfy the generic problem

$$(-\partial_r^2 + V_\ell) \mathbf{w} = f; \quad (\text{A.15a})$$

$$(\mathfrak{B}_L \mathbf{w})(r_{\min}) = g_L; \quad (\mathfrak{B}_R \mathbf{w})(r_{\max}) = g_R. \quad (\text{A.15b})$$

Due to the singularity of V_ℓ , we will also need to multiply by a regularizing factor f_{reg} , and we define

$$V_{\text{reg}} = f_{\text{reg}} r^2 V_\ell. \quad (\text{A.16})$$

In terms of variables

$$\boxed{\mathbf{w}, \quad \mathbf{v} := r \left(\frac{\mathbf{w}}{r} \right)'}, \quad (\text{A.17})$$

then multiplying (A.15a) by $f_{\text{reg}} r^2$ and with the boundary conditions at r_{\min} and r_{\max} , we have²⁰

$$-f_{\text{reg}} r(r\mathbf{v})' + V_{\text{reg}} \mathbf{w} = r^2 f_{\text{reg}} f; \quad r\mathbf{w}' - \mathbf{w} = r\mathbf{v}; \quad (\text{A.20a})$$

$$(\mathbf{B}\mathbf{w}, \mathbf{v})(r_{\min}) = 0; \quad (\tilde{\mathbf{B}}(\mathbf{w}, \mathbf{v})(r_{\max}) = 0, \quad (\text{A.20b})$$

where the boundary trace operator is listed in Appendix A.2.3.

Table 6: Boundary conditions for first-order formulation of the conjugated modal equation $-\partial_r^2 + V_\ell$ using variables (w, v) where $v = r(\frac{w}{r})'$.

$r \in \Sigma_\bullet$	$\mathbf{B}_\bullet \mathbf{w} = g_\bullet$	$\mathbf{B}_\bullet(w, v) = g_\bullet$
$\bullet = \text{d}$	$w(r) = g_{\text{d}}$	$w(r) = g_{\text{d}}$
$\bullet = \text{dv}$	$(r(\frac{w}{r})')(r) = g_{\text{dv}}$	$v(r) = g_{\text{dv}}$
$\bullet = \text{a}$	$w'(r) - i \mathcal{Z}(r) w(r) = g_{\text{a}}$	$v(r) + (\frac{1}{r} - i \mathcal{Z}(r)) w(r) = g_{\text{a}}$

Therefore, the two approaches to compute \mathcal{G}_ℓ^+ using first-order formulations are:

²⁰Using $r^2 \partial_r^2 = (r \partial_r)^2 - r \partial_r$ and $r\mathbf{w}' = \mathbf{w} + r\mathbf{v}$

$$r^2 \partial_r^2 \mathbf{w} = r \partial_r (r \partial_r \mathbf{w}) - r \partial_r \mathbf{w} = r \partial_r (\mathbf{w} + r\mathbf{v}) - r \partial_r \mathbf{w} = r(r\mathbf{v})'. \quad (\text{A.18})$$

Regarding the RBC: for $r \neq 0$,

$$w'(r) = i \mathcal{Z}(r) w(r) \Leftrightarrow \frac{1}{r} w(r) + v(r) = i \mathcal{Z}(r) v(r) \Leftrightarrow v(r) = \left(-\frac{1}{r} + i \mathcal{Z}(r) \right) w(r). \quad (\text{A.19})$$

– **Approach 1.** Find (v, w) that solves

$$\begin{cases} -f_{\text{reg}} r (r w)' + r^2 f_{\text{reg}} V_\ell w = r^2 f_{\text{reg}} \delta(r-s), & \text{on } (0, r_{\max}); \\ r w' - w = r v, & \text{on } (0, r_{\max}); \\ v(0) = 0, \quad v(r_{\max}) = \left(-\frac{1}{r_{\max}} + \mathcal{Z}_\bullet\right) w(r_{\max}). \end{cases} \quad (\text{A.21})$$

Then, we have $\mathcal{G}_\ell^+(r, s) = w(r)$.

– **Approach 2.** The computational steps are listed in [Algorithm 2](#).

Algorithm 2 Algorithm to compute G_ℓ^{PP} via \mathcal{G}_ℓ^+ using first-order formulation, working with the conjugate modal operator $(-\partial_r^2 + V_\ell)$, with $r_{\min} > 0$ and $r_b \leq r_{\max}$.

Step 1a. Find (v, w) that solves

$$\begin{cases} -r (r v)' + r^2 V_\ell w = 0, & \text{on } (0, r_b); \\ r w' - w = r v, & \text{on } (0, r_b); \\ v(0) = 0, \quad w(r_b) = 1. \end{cases} \quad (\text{A.22})$$

Set $\varphi := w$ and $\varphi' := v + w/r$.

Step 1b. Find (v, w) that solves

$$\begin{cases} -r (r v)' + r^2 V_\ell w = 0, & \text{on } (r_{\min}, r_{\max}); \\ r w' - w = r v, & \text{on } (r_{\min}, r_{\max}); \\ w(r_{\min}) = 1, \quad v(r_{\max}) = \left(-\frac{1}{r_{\max}} + \mathcal{Z}_\bullet\right) w(r_{\max}). \end{cases} \quad (\text{A.23})$$

Set $\varphi^+ := w$ and $\varphi^{+'} := v + w/r$.

Step 2. Using $W^+ := W^+(s) = \varphi(s) \partial_r \varphi^+(s) - \varphi^+(s) \partial_r \varphi(s)$ (that only needs a value at one point), we assemble the Green's function,

$$\mathcal{G}_\ell^+(r, s) = \frac{-\mathbb{H}(s-r) \varphi(r) \varphi^+(s) - \mathbb{H}(r-s) \varphi^+(r) \varphi(s)}{W^+}, \quad (\text{A.24})$$

with $K_\ell(r, s)$ defined in (3.85), we have

$$G_\ell^{\text{PP}}(r, s) = \mathcal{G}_\ell^+(r, s) K_\ell(r, s). \quad (\text{A.25})$$

A.2.4 Discretization with HDG

We follow the notation given in [Subsection 5.4](#). The HDG problem is defined as:

Find $(\mathbf{w}_h, \mathbf{v}_h, \lambda_h)$ that solves

– the local volume problems for $\phi \in W_h(\Omega)$, $\psi \in V_h(\Omega)$, for $1 \leq e \leq |\mathcal{T}_h|$,

$$\begin{cases} -\int_K (r \mathbf{v}_h)' f_{\text{reg}} r \phi \, dr + \int_K V_{\text{reg}} \mathbf{w}_h \phi \, dr \\ \quad - \sum_{r \in \partial K} \tau^K (\mathbf{w}_h - \lambda_h)|_r (r^2 f_{\text{reg}} \phi)|_r \nu_{\partial K}(r) = \int_K f_{\text{reg}} r^2 \phi \, dr; \end{cases} \quad (\text{A.26a})$$

$$\begin{cases} \int_K \mathbf{w}_h (r \psi)' \, dr + \int_K \mathbf{w}_h \psi \, dr + \int_K r \mathbf{v}_h \psi \, dr - \sum_{r \in \partial K} (r \psi)|_r \nu_{\partial K}(r) = 0, \end{cases} \quad (\text{A.26b})$$

– and the problems on the interior faces Σ_{I} and boundary ones $\partial\Omega_h$,

$$\begin{cases} \llbracket v_h + \tau(w_h - \lambda_h) \rrbracket_r = 0, & \text{for } r \in \Sigma_{\text{int}}; \\ \mathfrak{B}_{\text{L}}(\mathbf{w}_h, \mathbf{v}_h, \lambda_h)(r_{\min}) = g_{\text{L}}; & \mathfrak{B}_{\text{R}}(\mathbf{w}_h, \mathbf{v}_h, \lambda)(r_{\max}) = g_{\text{R}}. \end{cases} \quad (\text{A.27a})$$

$$\quad (\text{A.27b})$$

The discretized HDG problem is the following:
Find \mathbf{U}^e, Λ that solve

$$\begin{cases} \mathbb{A}^e \mathbf{U}^e + \mathbb{C}^e \mathcal{R}_e \Lambda = \begin{pmatrix} \mathbf{F}^e \\ \mathbf{0}_{1 \times m_e} \end{pmatrix}, & \text{for all } 1 \leq e \leq |\mathcal{T}_h|; \\ \sum_{e=1}^{|\mathcal{T}_h|} \mathcal{R}_e^t (\mathbb{B}^e \mathbf{U}^e + \mathbb{L}^e \mathcal{R}_e \Lambda) = \sum_{e=1}^{|\mathcal{T}|} \mathcal{R}_e^t \mathbf{s}^e, \end{cases} \quad (\text{A.28a})$$

$$\quad (\text{A.28b})$$

where the component matrices are defined below.

– The matrices of the local problem are

$$\mathbf{F}_k^e = \int_{K^e} r^2 f_{\text{reg}} f \phi_k; \quad \mathbb{A}^e := \begin{pmatrix} \mathbb{Q}^e + \tau^e \mathbb{R}^e & \mathbb{T}^e \\ \mathbb{S}^k & \mathbb{M}^e \end{pmatrix}, \quad (\text{A.29})$$

with component matrices

$$\begin{aligned} \mathbb{Q}_{kl}^e &= \int_{K^e} V_{\text{reg}} \phi_k \phi_l; & \mathbb{S}_{kl}^K &= \int_{K^e} \phi_k (2\psi_l + r \psi_l'); \\ \mathbb{T}_{kl}^e &= - \int_{K^e} f_{\text{reg}} (\psi_k + r \psi_k') r \phi_l; & \mathbb{M}_{kl}^K &= \int_{K^e} r \psi_k \psi_l; \\ \mathbb{R}^e &= +f_{\text{reg}}(r^{(e,1)}) (r^{(e,1)})^2 \mathbb{E}_{11} - f_{\text{reg}}(r^{(e,2)}) (r^{(e,2)})^2 \mathbb{E}_{n_e n_e}, \end{aligned} \quad (\text{A.30})$$

and

$$\mathbb{C}^K = \begin{pmatrix} -\tau^e f_{\text{reg}}(r^{(e,1)}) (r^{(e,1)})^2 \mathbf{e}_1 & \tau^e f_{\text{reg}}(r^{(e,2)}) (r^{(e,2)})^2 \mathbf{e}_{n_e} \\ r^{(e,1)} \mathbf{e}_1 & -r^{(e,2)} \mathbf{e}_{m_e} \end{pmatrix}. \quad (\text{A.31})$$

Here \mathbf{e}_i is the element column unit vector.

– The matrices of the global discrete problem are given by

$$\mathbb{B}^e = \begin{pmatrix} \mathbb{F}^{(e,1)} & \mathbb{Q}^{(e,2)} \\ \mathbb{F}^{(e,2)} & \mathbb{Q}^{(e,2)} \end{pmatrix}, \quad \mathbb{L}^e = \begin{pmatrix} L_1^e & 0 \\ 0 & L_2^e \end{pmatrix}, \quad \mathbf{s}^e = \begin{pmatrix} \mathbf{s}^{(e,1)} \\ \mathbf{s}^{(e,e)} \end{pmatrix}, \quad (\text{A.32})$$

with components given by

$\mathbf{r}^{(e,i)} \in$	$\mathbb{F}^{(e,i)} \in \mathbb{R}^{1 \times n_e}$	$\mathbb{Q}^{(e,i)} \in \mathbb{R}^{1 \times m_e}$	$L_i^e \in \mathbb{R}$	$\mathbf{s}^{(e,i)} \in \mathbb{R}$	i
Σ_{int}	$-\tau^e \mathbf{e}_1$	$-\mathbf{e}_1$	τ^e	0	$i = 1$
	$\tau^e \mathbf{e}_{n_e}$	\mathbf{e}_{m_e}	$-\tau^e$	0	$i = 2$
Σ_{a}	$\tau^e \mathbf{e}_{n_e}$	\mathbf{e}_{m_e}	$\frac{1}{r^{(e,2)}} - i\mathcal{Z}(r^{(e,2)}) - \tau^e$	g_{a}	$i = 2$
Σ_{d}	0	0	1	g_{Ld}	$i = 1$
	0	0	1	g_{Rd}	$i = 2$
Σ_{dv}	$-\tau^e \mathbf{e}_1$	$-\mathbf{e}_1$	τ^e	g_{dv}	$i = 1$

In the above equation, \mathbf{e}_i is the elementary row unit vector.

References

- [1] Shmuel Agmon and Markus Klein. Analyticity properties in scattering and spectral theory for Schrödinger operators with long-range radial potentials. *Duke Mathematical Journal*, 68(2):337–399, 1992.
- [2] H el ene Barucq, Juliette Chabassier, Marc Durufl e, Laurent Gizon, and Michael Legu ebe. Atmospheric radiation boundary conditions for the Helmholtz equation. *ESAIM: Mathematical Modelling and Numerical Analysis*, 52(3):945–964, 2018.
- [3] H el ene Barucq, Florian Faucher, Damien Fournier, Laurent Gizon, and Ha Pham. Efficient and accurate algorithm for the full modal green’s kernel of the scalar wave equation in helioseismology. *SIAM Journal on Applied Mathematics*, 80(6):2657–2683, 2020.
- [4] H el ene Barucq, Florian Faucher, Damien Fournier, Laurent Gizon, and Ha Pham. Efficient computation of the modal outgoing Green’s kernel for the scalar wave equation in helioseismology. Research Report RR-9338, Inria Bordeaux Sud-Ouest ; Magique 3D ; Max-Planck Institute for Solar System Research, April 2020.
- [5] H el ene Barucq, Florian Faucher, Damien Fournier, Laurent Gizon, and Ha Pham. On the outgoing solutions and radiation boundary conditions for the vectorial wave equation with ideal atmosphere in helioseismology. Research Report RR-9335, Inria;MPS, April 2020.
- [6] H el ene Barucq, Florian Faucher, Damien Fournier, Laurent Gizon, and Ha Pham. Outgoing modal solutions for Galbrun’s equation in helioseismology. *Journal of Differential Equations*, 286:494–530, 2021.
- [7] H el ene Barucq, Florian Faucher, and Ha Pham. Outgoing solutions to the scalar wave equation in helioseismology. Research Report RR-9280, Inria Bordeaux Sud-Ouest, August 2019.
- [8] H el ene Barucq, Florian Faucher, and Ha Pham. Outgoing solutions and radiation boundary conditions for the ideal atmospheric scalar wave equation in helioseismology. *ESAIM: Mathematical Modelling and Numerical Analysis*, 54(4):1111–1138, 2020.
- [9] Jishnu Bhattacharya. Helioseismic finite-frequency sensitivity kernels for flows in spherical geometry including systematic effects. *The Astrophysical Journal*, 905(1):59, 2020.
- [10] Jishnu Bhattacharya, Shravan M Hanasoge, and Katepalli R Sreenivasan. A general formulation for computing spherical helioseismic sensitivity kernels while incorporating systematical effects. *The Astrophysical Journal*, 895(2):117, 2020.
- [11] Aaron C Birch and Alexander G Kosovichev. Travel time sensitivity kernels. In *Helioseismic Diagnostics of Solar Convection and Activity*, pages 193–201. Springer, 2001.
- [12] Vincent GA B oning, Markus Roth, Wolfgang Zima, Aaron C Birch, and Laurent Gizon. Sensitivity kernels for flows in time–distance helioseismology: Extension to spherical geometry. *The Astrophysical Journal*, 824(1):49, 2016.
- [13] Juliette Chabassier and Marc Durufl e. Solving time-harmonic Galbrun’s equation with an arbitrary flow. Application to helioseismology. Technical report, Inria Bordeaux Sud-Ouest; Magique 3D, 2018.
- [14] Subramanyan Chandrasekhar and Paul C Kendall. On force-free magnetic fields. *The Astrophysical Journal*, 126:457, 1957.
- [15] J. Christensen-Dalsgaard, W. D appen, S. V. Ajukov, E. R. Anderson, H. M. Antia, S. Basu, V. A. Baturin, G. Berthomieu, B. Chaboyer, S. M. Chitre, A. N. Cox, P. Demarque, J. Donatowicz, W. A. Dziembowski, M. Gabriel, D. O. Gough, D. B. Guenther, J. A. Guzik, J. W. Harvey, F. Hill, G. Houdek, C. A. Iglesias, A. G. Kosovichev, J. W. Leibacher, P. Morel, C. R. Proffitt, J. Provost, J. Reiter, E. J. Rhodes, F. J. Rogers, I. W. Roxburgh, M. J. Thompson, and R. K. Ulrich. The current state of solar modeling. *Science*, 272(5266):1286–1292, 1996.
- [16] J orgen Christensen-Dalsgaard. Helioseismology. *Reviews of Modern Physics*, 74(4):1073, 2002.

- [17] Jørgen Christensen-Dalsgaard. ADIPLS – The Aarhus adiabatic oscillation package. *Astrophysics and Space Science*, 316(1-4):113–120, 2008.
- [18] Jørgen Christensen-Dalsgaard. Lecture notes on stellar oscillations, 2014.
- [19] David Colton and Rainer Kress. *Inverse acoustic and electromagnetic scattering theory*, volume 93. Springer Nature, 2013.
- [20] Francis Anthony Dahlen and Jeroen Tromp. *Theoretical global seismology*. Princeton university press, 2021.
- [21] Florian Faucher. **hawen**: time-harmonic wave modeling and inversion using hybridizable discontinuous Galerkin discretization. *Journal of Open Source Software*, 6, 2021.
- [22] Florian Faucher, Damien Fournier, and Ha Pham. C^2 representations of the solar background coefficients for the model S-AtmoI. *arXiv preprint arXiv:2009.01587*, 2020.
- [23] Pablo Fernandez, Alexandra Christophe, Sebastien Terrana, Ngoc Cuong Nguyen, and Jaime Peraire. Hybridized discontinuous galerkin methods for wave propagation. *Journal of Scientific Computing*, 77(3):1566–1604, 2018.
- [24] Damien Fournier, Michaël Leguèbe, Chris S Hanson, Laurent Gizon, Hélène Barucq, Juliette Chabassier, and Marc Duruflé. Atmospheric-radiation boundary conditions for high-frequency waves in time-distance helioseismology. *Astronomy & Astrophysics*, 608:A109, 2017.
- [25] Henri Galbrun. *Propagation d'une onde sonore dans l'atmosphère et théorie des zones de silence*. Gauthier-Villars et Cie, Éditeurs., 1931.
- [26] Laurent Gizon, Hélène Barucq, Marc Duruflé, Chris S Hanson, Michael Leguèbe, Aaron C Birch, Juliette Chabassier, Damien Fournier, Thorsten Hohage, and Emanuele Papini. Computational helioseismology in the frequency domain: acoustic waves in axisymmetric solar models with flows. *Astronomy & Astrophysics*, 600:A35, 2017.
- [27] D. O. Gough. Linear adiabatic stellar pulsation. In *Astrophysical Fluid Dynamics - Les Houches 1987*, pages 399–560, January 1993.
- [28] Martin Halla. On the treatment of exterior domains for the time-harmonic equations of stellar oscillations. *arXiv preprint arXiv:2105.04161*, 2021.
- [29] Martin Halla and Thorsten Hohage. On the well-posedness of the damped time-harmonic Galbrun equation and the equations of stellar oscillations. *SIAM J. Math. Anal.*, 2021.
- [30] D Lynden-Bell and JP Ostriker. On the stability of differentially rotating bodies. *Monthly Notices of the Royal Astronomical Society*, 136(3):293–310, 1967.
- [31] Marcus Maeder, Gwénaél Gabard, and Steffen Marburg. 90 years of Galbrun's equation: An unusual formulation for aeroacoustics and hydroacoustics in terms of the lagrangian displacement. *Journal of Theoretical and Computational Acoustics*, 28(04):2050017, 2020.
- [32] Krishnendu Mandal, Jishnu Bhattacharya, Samrat Halder, and Shravan M Hanasoge. Finite-frequency sensitivity kernels in spherical geometry for time-distance helioseismology. *The Astrophysical Journal*, 842(2):89, 2017.
- [33] Paul A Martin. *Multiple scattering: interaction of time-harmonic waves with N obstacles*. Cambridge University Press, 2006.
- [34] Peter Monk et al. *Finite element methods for Maxwell's equations*. Oxford University Press, 2003.
- [35] Ngoc Cuong Nguyen, Jaume Peraire, and Bernardo Cockburn. An implicit high-order hybridizable discontinuous galerkin method for linear convection–diffusion equations. *Journal of Computational Physics*, 228(9):3232–3254, 2009.

-
- [36] Ruben Sevilla. An implicit hdg method for linear convection-diffusion with dual time stepping. *Journal of Computational Physics*, 434:110201, 2021.
- [37] Wasaburo Unno, Yoji Osaki, Hiroyasu Ando, and H Shibahashi. Nonradial oscillations of stars. *nos*, 1979.
- [38] Dmitriĭ Aleksandrovich Varshalovich, Anatolij Nikolaevič Moskalev, and Valerii Kelmanovich Kher-sonskii. *Quantum theory of angular momentum*. World Scientific, 1988.
- [39] J. E. Vernazza, E. H. Avrett, and R. Loeser. Structure of the solar chromosphere. III. Models of the EUV brightness components of the quiet sun. *The Astrophysical Journal Supplement Series*, 45:635–725, April 1981.



**RESEARCH CENTRE
BORDEAUX – SUD-OUEST**

200 avenue de la Vieille Tour
33405 Talence Cedex

Publisher
Inria
Domaine de Voluceau - Rocquencourt
BP 105 - 78153 Le Chesnay Cedex
inria.fr

ISSN 0249-6399